DSMC Simulation of Flows in Multiple Microchannel Geometries

Minmin Le

A Thesis

in

The Department

of

Mechanical and Industrial Engineering

Presented in Partial Fulfillment of the Requirements
for the Degree of Master of Applied Science (Mechanical Engineering) at
Concordia University
Montreal, Quebec, Canada

March 2006

Your file Votre référence
ISBN: 978-0-494-16251-4
Our file Notre référence
ISBN: 978-0-494-16251-4

ABSTRACT

DSMC Simulation of Flows in Multiple Microchannel Geometries

Minmin Le

The direct simulation Monte Carlo method was applied to simulate the flows in uniform, parallel, series, and T-shape microchannels. For the uniform microchannel case, both the supersonic and subsonic flows have been considered. The effect of the Knudsen number (Kn) on the flow properties and the heat transfer characteristics were investigated. Some significant flow features, such as the flow acceleration along the channel, the nonlinear pressure distribution, and the velocity slip near the wall, due to the compressibility and the rarefaction of the microflow were specified. Most of the wall heat flux occurs within the channel entrance region when the wall temperature is higher than the bulk flow temperature. Furthermore, in supersonic flow case, the wall heat flux is mainly caused by the deceleration of the flow due to the wall friction.

For the series microchannel case, diffuse effect were observed near the interface of the two segments, where the flow upstream of the interface can be either heated or cooled by the flow downstream depending on their temperature difference. In addition, the effect of the gas species was investigated by conducting the simulation using helium and argon respectively. It was found that the speed of the gas with lighter molecular mass is much higher than that of the heavier gas. For the parallel microchannel cases, with a certain pressure ratio, more pressure drop occurs in the parallel parts as the gap height increases. The recirculation phenomenon was observed after the gap wall between the two parallel parts and was evaluated quantitatively by defining a parameter called the developing

coefficient in the present study. The gap height between the two parallel parts has only slight effect of the flow development.

In a T-shape microchannel, the gas mixing process was simulated by introducing nitrogen and carbon monoxide at the two inlets of the T junction respectively. The effect of the channel geometry, Kn, inlet pressure, free stream temperature, and wall temperature on the mixing length was examined. An enhancement in gas mixing can be observed in the T-shape micro mixer due to the gas diffusion within the T junction, which does not exist in its macro counterpart.

This work is dedicated

to

my dear parents.

献给我最亲爱的爸爸和妈妈

Table of Contents

List of Figures ..... **viii**

List of Tables ..... **xii**

Nomenclature ..... **xiii**

1 Introduction **1**

2 Literature Review **7**

2.1 Supersonic Microchannel Flows 7

2.2 Subsonic Microchannel Flows 8

2.3 Inlet/Outlet Boundary Conditions 21

2.4 Experimental Work 28

2.5 Summary and Objectives 31

2.5.1 Physical modeling and the application 31

2.5.2 Advances in DSMC 33

2.5.3 Objectives 33

3 Numerical Modeling and the Direct Simulation Monte Carlo Method **....35**

3.1 Microchannel Geometries and Flow Parameters 35

3.2 Numerical Solutions and Flow Samplings 41

3.2.1 Network setting and time step 42

3.2.2 Gas-wall surface interaction 43

3.2.3 Boundary conditions 44

3.2.4 NTC scheme and VHS model 47

3.2.5 Flow sampling 50

3.3 Accuracy of the Numerical Results 52

4 Supersonic Flow in Uniform Microchannels 58

4.1 Code Verification 58

4.2 Supersonic Microchannel Flows with Vacuum Boundary 58

4.2.1 Effect of the Kn number 58

4.2.2 Effect of wall temperature distribution, flow direction and free stream temperature 72

4.3 Supersonic Microchannel Flows With Pressure Boundary 73

4.3.1 Effect of the back pressure 73

4.3.2 Effect of the inlet Mach number 76

5 Subsonic Flow in Uniform, Series and Parallel Microchannels and Gas Mixing in T-shape Microchannel 85

5.1 Code Verification 85

5.2 Uniform Microchannel Flow 85

5.3 Series Microchannel Flows 95

5.4 Parallel Microchannel Flows 101

5.5 T- Shape Micromixer 109

5.5.1 Characterization of the mixing process 109

5.5.2 Effect of channel geometry and Kn 115

5.5.3 Effects of inlet pressure, free stream temperature, and wall temperature 119

6 Conclusion and Future Directions 126

6.1 Conclusion 126

6.2 Future Directions 128

References 130

List of Figures

Figure 3.1 (a): Schematic of the uniform microchannel geometry.....36

Figure 3.1 (b): Schematic of the series microchannel geometry. 36

Figure 3.1 (c): Schematic of the parallel microchannel geometry. 36

Figure 3.1 (d): Schematic of the T-shape microchannel geometry. 37

Figure 3.2 (a): Boundary conditions for the series microchannel flow. 38

Figure 3.2 (b): Boundary conditions for the parallel microchannel flow. 38

Figure 3.2 (c): Boundary conditions for the T-shape microchannel flow. 39

Figure 3.3: Mesh size effect on: (a) the pressure distribution along the uniform channel, (b) the streamwise velocity profiles at the channel mid-span. 54

Figure 3.4 (a): Effect of the average number of simulated particles per cell on the pressure and centerline temperature distributions 56

Figure 3.4 (b): Effect of the average number of simulated particles per cell on velocity profiles at channel inlet, mid-span, and outlet. 57

Figure 4.1: Comparison of the streamwise velocity at x/L = 0.5 for vacuum boundary cases. 59

Figure 4.2: Comparison of the centerline temperature distribution for vacuum boundary cases. 60

Figure 4.3: Velocity profiles at a) x/L = 0.1, b) x/L = 0.4, c) x/L = 0.7 and d) x/L = 0.9 for different Kn cases 61

Figure 4.4: Temperature profiles at a) x/L = 0.1, b) x/L = 0.4, c) x/L = 0.7 and d) x/L = 0.9 for different Kn cases. 63

Figure 4.5: Effect of the Kn on the centerline temperature distribution.....65

Figure 4.6: Temperature profiles at x/L = 0.40, 0.45, 0.50 and 0.55 for Kn = 0.186.....66

Figure 4.7: Effect of the Kn on the Mach number contours.....68

Figure 4.8: The wall heat flux distributions for different Kn. 69

Figure 4.9: Effect of wall temperature distribution on the wall heat flux for a) L/H = 5 and b) L/H = 10. 71

Figure 4.10: Effect of free stream temperature on the wall heat flux.....72

Figure 4.12: Velocity profiles at a) x/L = 0.3, b) x/L = 0.5, c) x/L = 0.7 and d) x/L = 0.9 for different outlet boundaries. 75

Figure 4.13: Temperature profiles at a) x/L = 0.3, b) x/L = 0.5, c) x/L = 0.7 and d) x/L = 0.9 for different outlet boundaries. 77

Figure 4.14: Wall heat flux with respect to different outlet boundaries.....78

Figure 4.15: Mach number contours for supersonic microchannel flow with M_{in} = 3.39 and M_{in} = 4.15.....80

Figure 4.16: Effect of the inlet Mach number on the pressure distribution along the channel centerline at P_b = 0.5 MPa. 81

Figure 4.17: Effect of the inlet Mach number on the wall heat flux at P_b = 0.5 MPa. 82

Figure 5.1: Pressure distribution along the uniform microchannel for Kn_{in} = 0.0547 and P_{in}/P_{out} = 4. 86

Figure 5.2: Velocity profiles corresponding to different local Knudsen numbers in uniform microchannel. 87

Figure 5.3: The wall heat flux distribution for flow in uniform microchannels with T_w = 500K.....88

Figure 5.4: The wall temperature jump for flow in uniform microchannels.....90

Figure 5.5: Kn number distribution along the uniform channel for P_{in} / P_{out} = 4, 2 and 1.33. 91

Figure 5.6: Mach number distribution along the centerline of the uniform microchannel. 92

Figure 5.7: Wall heat flux for cases with linear wall temperature distribution. 93

Figure5.8: Temperature distribution of the flow close to the wall. 94

Figure 5.9: Velocity vectors for series microchannel flow at P_{in}/P_{out} = 4 and Kn_{in} = 0.0912. 96

Figure 5.10: Pressure distribution of the series microchannel flow coming from difference edges at P_{in}/P_{out} = 4. 97

Figure 5.11: Wall heat flux for the series microchannel flows with different wall temperature distributions. 99

Figure 5.12: Temperature profiles at (a) x/L = 0.25, (b) x/L = 0.36, (c) x/L = 0.38 and (d) x/L = 0.60. 100

Figure 5.13: The velocity profiles at x/L = 0.431 for (a) P_{in}/P_{out} = 2, (b) P_{in}/P_{out} = 4, (c) P_{in}/P_{out} = 6 and (d) P_{in}/P_{out} = 8. 102

Figure 5.14: Velocity vectors of the parallel microchannel flow at P_{in}/P_{out} = 4 and Kn_{in} = 0.182 103

Figure 5.15: Evolution of the relative density difference. 105

Figure 5.16: The effect of the gap size on the developing coefficient. 106

Figure 5.17: Wall pressure distribution along the parallel microchannel with different gap sizes. 107

Figure 5.18: The effect of the gas size on the mass flow rate at P_{in}/P_{out} = 4. 108

Figure 5.19: Velocity vectors for the gas mixture of CO and N_2 in T-shape microchannel. 110

Figure 5.20: Mass fraction contours for the gas mixture of CO and N_2 in T-shape microchannel. 113

Figure 5.21: Evolution of the composition deviation coefficient along the main channel. 114

Figure 5.22: Effect of the channel dimension on the mixing process at a certain Kn. 116

Figure 5.23: Effect of the Kn on the mixing process by changing the inlet channel width. 117

Figure 5.24: Effect of the Kn on the mixing coefficient. 118

Figure 5.25: Effect of the inlet pressure on the mixing process. 120

Figure 5.26: Effect of the free stream temperature on the mixing process. 122

Figure 5.27: Effect of the wall temperature on the mixing process. 123

List of Tables

Table 4.1 Test cases for supersonic flows with vacuum boundary 83

Table 4.2 Test cases for supersonic flows with pressure boundary..... 84

Table 5.1 Test cases for subsonic flow in uniform microchannel 124

Table 5.2 Test cases for parallel and series microchnannel flows..... 125

Nomenclature

a	Local speed of sound (m/s)
A	Area of the cross section (m^2)
b	The distance of closet approach of the undisturbed trajectories in the center of mass frame of reference for a collision pair (m)
$\vec{C}$	Thermal velocity of molecules (m/s)
$C_m^{'}$	Most probable thermal velocity of the molecules (m/s)
C_r	The relative speed of two molecules (m/s)
d	Molecular diameter (m)
E_i	The energy of incident molecules on a wall surface (J)
E_r	The energy of reflected molecules from a wall surface (J)
E_w	The energy molecules would have if they acquired energy from the wall at the temperature of T_w (J)
F_N	The number of real molecules represented by a simulated particle
H_c	Characteristic length of the geometry (m)
k	Boltzmann constant
K_n	Knudsen number (λ/H)
L	Length of the geometry (m)
L_D	Developing length (m)
L_{mix}	Mixing length (m)
$\dot{m}$	Mass flow rate (kg/s)
m	Molecular mass (kg)
M	Flow Mach number
n	Gas number density

$\dot{n}$	The particle flux
$\dot{n}_+$	Flowing-in particle flux
$\dot{n}_-$	Flowing-out particle flux
nt	The total number of simulated molecules that strike the wall during the sampling time period
N	Average number of real molecules in one cell
$\dot{N}$	Net particle flux
NCY	The number of cells in the transverse direction
p	Pressure (Pa)
P	Probability of collision between two simulated particles
P_{max}	Maximum probability of collision between two simulated particles
q	Wall heat flux (W/m^2)
Q	Total heat exchange between the wall and the bulk flow (J)
Q_m	Mass flow rate ($g \cdot min^{-1} \cdot s^{-1}$)
R	Universal gas constant ($J \cdot K^{-1} \cdot mol^{-1}$)
R_f	Uniformly distributed random fraction between 0 and 1
s	Gap size between the two parallel parts of the parallel microchannel (m)
T	Gas temperature (K)
T_r	Reflection temperature (K)
T_{tr}	Transitional temperature (K)
T_{rot}	Rotational temperature (K)
T_w	Wall temperature (K)
T_{w1}	Wall temperature of the first channel section (K)
T_{w2}	Wall temperature of the second channel section (K)

Δt	Time step (s)
Δx_d	Cell dimension (m)
u	Velocity component of entering molecules in x direction (m/s)
U	Streamwise flow velocity (m/s)
U/U_c	Dimensionless velocity
v	Velocity component of entering molecules in y direction (m/s)
V	Magnitude of the flow velocity (m/s)
$\vec{V}$	Flow velocity (m/s)
V_c	Cell volume (m^3)
w	Velocity component in z direction of entering molecules (m/s)
x	Coordinate along the axis of the channel (m)
y	Coordinate along the vertical direction of the channel (m)

Subscripts

in	Properties at channel inlet
e	Properties at channel outlet
b	Properties at the back environment
c	Properties at the channel center
inc	Incident properties
j	Properties corresponding to the local cell
ref	Properties at a reference temperature T_{ref}
reflect	Reflected properties
w	Properties at the wall

Greek Letters

α	Thermal accommodation coefficient
β	Stocks number
χ	Deflection angle
ε_{rot}	Sample average of molecular rotational energy (J)
ε_{tr}	Sample average of molecular transitional energy (J)
ϕ	Angle with a uniform distribution from 0 to 2π
η_{mix}	Mixing coefficient
λ	Mean free path (m)
υ	Inverse power law
ρ	Flow density (kg/m^3)
ρ_0	The minimum density at a certain cross section along the main channel of the micromixer (kg/m^3)
ρ_1	The maximum density at a certain cross section along the main channel of the micromixer (kg/m^3)
σ	Cross-section (m^2)
σ_T	Total collision cross-section (m^2)
$\omega_\infty(i)$	The equilibrium mass fraction for species i
$\omega(i,y)$	The mass fraction for species i at location y in a cross section
ξr	Number of rotational degrees of freedom
ξ	Relative density difference
ζ	Composition deviation coefficient

Abbreviations

VHS Variable hard sphere model

NTC No-Time-Counter scheme

Chapter 1

Introduction

The technological advancement in fabrication has made it possible to produce microdevices, which opened a new field of research in the area of micro-electro-mechanical-systems (MEMS). Recently, attention has been directed to these microdevices because of their advantages over their macro counterparts, such as the relatively lower expense for manufacture in large quantities, the small size and mass rendering them possible to fit in specific situations, and the quick reaction from their minimal inertia, etc. However, the prediction of the flow properties and heat transfer characteristics in MEMS has not developed at the same rapid pace as micro fabrication techniques.

Currently, since the microdevices can be manufactured in micron size, it becomes possible for the gaseous flow to posses a mean free path comparable to the characteristic length of the device even at standard conditions (STP). According to the Knudsen number (Kn), which is used to evaluate the rarefaction of the fluid ($Kn = \lambda/h$), the flow is classified into different flow regimes in order to facilitate the dictation of the appropriate approach in analyzing the flow. Based on the general knowledge of rarefied gas dynamics, if $Kn < 0.01$ the flow is considered to be in the continuum regime and the continuum assumption of fluid is valid. When Kn falls into $0.01 < Kn < 0.1$ or $0.1 < Kn < 10$, the flow lies in the slip flow regime or transition flow regime correspondingly. As Kn exceeds 10 the flow is counted as free molecular flow. The size of the current microdeveices has made the Kn range between 0.001 and 1 approximately (Mavripls et

al., 1997). This fact indicates that the microdevices can fall into not only the continuum flow regime but also the slip or transition flow regime.

In the continuum flow model (Kn < 0.01), the Navier-Stokes equations govern the flow field as long as the flow is assumed to be infinitely divisible, it is required that sufficient molecules are contained within a finite space so that the macroscopic quantities can be justified without statistical fluctuations. When the flow becomes more rarefied, for example, when the Kn is of the order of 0.1, the wall heat flux, shear stress, pressure drop and mass flow rate cannot be predicted accurately based on the continuum hypothesis; that is, the Navier-Stokes equations are no longer valid. Instead, the Boltzmann equation, which involves the molecular motions rather than the macroscopic quantities, must be employed in the flow prediction. However, it is very expensive to solve the Boltzmann equation either analytically or numerically; therefore, a well-established alternative, the direct simulation Monte Carlo (DSMC) method is adopted in order to solve this problem.

The DSMC method introduced by Bird in the early 1970s is a particle-based model, which studies the rarefied flow in a direct physical way instead of solving any equation. In other words, the evolution of a large number of simulated particles, which represent the real molecules in the flow field, is simulated. Modeling is implemented by uncoupling the molecular motion and calculating the intermolecular collision between the simulated particles over a small time interval. In general, the DSMC method consists of four steps: moving of particles, indexing particles into cells, simulating the intermolecular collision of particles, and sampling of particles. In order to locate the particles and track their movements, the whole computational domain is divided into a number of cells, which contains sub-cells in a predefined structure. Initially, a set of

simulated particles are randomly distributed in each cell. Each of the particles is assigned a position, velocity components and energy, etc. Then, the mentioned four procedures are repeated within each time interval to encourage the evolution of the simulated particles. The macroscopic quantities of the simulated flow, such as the velocity, pressure, density, temperature and so on, are counted on a cell base and can be obtained from simple weighting averages of microscopic properties.

In the past 20 years, DSMC has been mainly used to study the rarefied atmospheric flows in the aerospace field (Oran et al., 1998). However, in recent years, the DSMC method is also applied in dealing with the micro flows in MEMS. Applications in MEMS include instrumentation, microelectronics, bioengineering, and advanced systems, where complex networks of microchannels may be used (Gabriel et al., 1988). Microchannels, being an elemental configuration in microfluidic system, have generated an increasing interest in predicting the internal flow behavior and corresponding heat transfer characteristics. The correct prediction will lead to improving current microchannel designs prior to manufacturing.

Many works have been attempted to conduct the prediction of microchannel flows. The supersonic flow in straight microchannel has been investigated by Mavriplis et al. (1997), Oh et al. (1997) and Liou et al. (2001). However, due to its limited application while it is not realistic to have such a high speed flow inside micro devices, not a lot of studies have been done in literature. Thus, much more effort has been contributed to the study of the subsonic microchannel flows. In order to simulate the subsonic microchannel flows, several ideas were developed to implement the pressure boundary conditions. The theory of conservation of particles was employed at the inlet and outlet boundaries by

Ikegawa et al. (1990). Nance et al. (1998) applied the particle conservation theory at the channel inlet on a cell base, while the theory of characteristics was employed to enforce the outlet boundary condition. Liou et al. (2000, 2001) followed Nance's method and presented it in more detail. In 2004, Wang et al. introduced a new boundary treatment for pressure boundary conditions, which applied the theory of characteristics at both the inlet and the outlet of the microchannel. This new treatment is proved to have a better efficiency as well as a better astringency than the others (Wang et al., 2004).

With the pressure boundaries, a lot of fundamental works have been conducted for subsonic flows in two dimensional uniform microchannels (Piekos et al. 1995, Fan et al. 1999, Liou et al. 2000, Xue et al. 2000, Fang et al. 2002, Yan et al. 2002, H. Qunwu et al. 2004, and Wang et al. 2004), as well as for micro-Couette flow (Liou et al. 2000, Xue et al. 2003 and Liu et al. 2004). Here, flows in both the slip regime and the transition regime were taken into account. More specifically, Hadjiconstantinou (2000, 2002, and 2003) conducted a very comprehensive study in order to understand the heat transfer characteristics of flow in uniform microchannels. Some significant flow features due to the compressibility and the rarefaction of the flow, such as the flow acceleration along the channel, the nonlinear pressure distribution, and the velocity slip near the wall, were specified. As for the heat transfer characteristics between the wall and the bulk flow where a higher wall temperature is imposed, the wall heat flux only occurs in the channel entrance region. Furthermore, the Nusselt number decreases with the increasing flow rarefaction.

Microflows in other simple geometries have also been examined. . For example, a 2-D duct with a cavity (Ikegawa et al., 1990), straight microchannel with a solid core inside

(Mavriplis et al. 1997), a straight microchannel with a rectangular orifice inside (Wang et al. 2004), a T-shape micro-manifold (Wu et al. 2001), a bended microchannel (Wang et al. 2004), as well as a three-dimensional rectangular channel with a moving surface (Yan et al. 2002) have all been studied in DSMC simulations. Furthermore, mixing of two different gas species in a uniform microchannel, in which a splitter plate was placed at the channel entrance to separate the two incoming gases, was first carried out using DSMC by Wang et al. (2005). However, this configuration can just provide some academic value, which is not applicable as a real micro device. It was found that the dynamic flow properties of the microflows differ from those observed in the continuum flow.

In the present study, the research work starts with the verification of the DSMC code by investigating subsonic flows in uniform microchannels. The flow properties and heat transfer characteristics will be investigated by changing the pressure ratio, the wall temperature distribution and the channel dimension. Then, our work will be extended to study the gaseous flows in parallel and series multiple microchannels. The flow behaviors with respect to the geometry, the pressure ratio, the gas species and the wall temperature distribution will all be explored. Typically, the diffusion effect in the series microchannel will be revealed. Moreover, the effects of the channel geometry and the pressure ratio on the flow development in parallel microchannel will be evaluated quantitatively.

The micromixer with a T shape mixing configuration, where the two gas flows coming from the different inlets start to diffuse at the inlet of a T junction before subsequent processing, can perform a better mixing effect than its macro counterpart. This phenomenon leads to an increasing interest for the research work. In the current

work, the mixing performance of two gaseous flows within a T shape micromixer will be simulated using the DSMC method, which has not been found in literature. The effects of the pressure ratio, the inlet Kn number, the channel geometry, the free stream temperature and the temperature of the wall on the mixing effect will be thoroughly explored.

Chapter 2

Literature Review

2.1 Supersonic Microchannel Flows

Mavriplis et al. (1997) investigated the supersonic flows through two-dimensional microchannels with varying aspect ratios using DSMC, where nitrogen was considered as the testing species. The simulated supersonic flow had an inlet Mach number of 4.03 and the Kn number ranged from 0.0046 to 0.18 corresponding to the continuum flow regime and the transitional flow regime respectively. The wall temperature was maintained at 300 K, which was equal to the temperature of the incoming free stream flow. A step was introduced by excluding a rectangular section from the domain. A symmetric boundary was imposed along the channel centerline so that the computation time can be shortened by considering only the lower half of the channel. As the Kn increases, the bow shock attached to the boundary wall before the step broadens. Also, for the case in transitional flow regime where the Kn is equal to 0.18, the wall heat flux decreases monotonically with an increasing inlet pressure as the flow becomes exclusively subsonic inside the channel. It was shown that increasing the channel length would lead to a similar effect to that of a more rarefied flow since both of the factors would increase the retarding force from the wall.

Oh et al. (1997) combined the Direct Simulation Monte Carlo Method with the Monotonic Lagrangian Grid (MLG), which allows the grids to be refined automatically by considering the changing of the local number density throughout the flow. The DSMC-MLG method developed in their work sped up the simulation through a massively

parallel computation process used to predict the high-speed, high Kn microchannel flow. A new boundary condition was used in their study to specify the pressure information at the outlet boundary by defining a virtual region outside of the computational domain. The inlet Mach number for all flow cases in this study was set at 5.0. At the channel entrance, as the Kn increases, the shock thickness and oblique shock angles, as well as the velocity slip and the temperature jump increase. However, as the flow develops further downstream, the velocity slip remains constant while the wall temperature jump decreases gradually.

Liou et al. (2001) studied the heat transfer characteristics of supersonic flow in two-dimensional microchannels by means of DSMC. Different Kn, Kn = 0.031, Kn = 0.062, and Kn = 0.186, were obtained by changing the channel height to examine the shock structure, temperature distribution, velocity distribution, and wall heat flux. A Variable Hard Sphere (VHS) model was employed to simulate the collision by a probabilistic procedure for each pair of collision particles. At the upper and lower wall boundaries, the temperatures were set equal, and the diffuse reflection model was chosen to determine the gas-surface interactions. As the Kn increases, especially in the higher Kn case (Kn = 0.186), it was shown that the number rate of the molecules impacting the wall increases, which was considered as a dominating factor in enhancing the wall heat flux.

2.2 Subsonic Microchannel Flows

Ikegawa et al. (1990) modeled the subsonic microchannel gaseous flows with the pressure conditions given at the inlet and outlet boundaries. The original DSMC code was modified by applying the theory of conservation of particles at both channel edges to implement the pressure boundary conditions. The modified code was verified by

simulating the plane Poiseuille flow and comparing the results with the analytical solutions as well as the experiment results. Then, the modified code was applied to investigate the flow in the duct with a cavity. The whole computational domain was divided into partial regions in order to conduct the prediction in the complex-shaped duct. Due to the large Kn, no flow separation was found at the corners. Also, since the Reynolds number was really small the gas stream flowed smoothly parallel to the duct walls.

Piekos et al. (1995) investigated the pressure-driven microchannel flows in both the slip and transition regime. Pressure was specified at both the inlet and outlet face; the incoming flow temperature was given at the inlet face. For flows in the slip regime, the outlet Kn was maintained at 0.05. Some flow behaviors, such as the flow acceleration due to the density drop, the velocity slip increasing down the channel walls, were observed, which differs from the familiar Poiseuille result. The accuracy of the results was supported by the excellent agreement between their simulations and the analytical solutions. The unique feature of the DSMC was demonstrated in predicting the transition regime flows, where the Kn was set between 0.1 and 3. The analytical prediction with slip boundary condition started to fail at near Kn = 0.15 evidently. The nonlinear pressure distribution, the nonzero velocity slip at the walls and the flow acceleration down the channel became more significant as the Kn increased. A new expression, 'similarity speed', was developed to further compare the DSMC results with the analytical solutions of N-S equations. The N-S equations were found to be only strictly valid to first order in Kn. The DSMC is therefore a versatile tool because of its instructed grid capability and particle-tracing scheme. In addition, the supersonic micro-nozzle flow was investigated.

The nozzle exit was treated as a 'vacuum' while the inlet pressure was set as 10 times of the reference value.

Mavriplis et al. (1997) examined the subsonic, pressure-driven low speed flows in microchannels. Simulations for the subsonic flow with M_{in} = 0.4 and T_{in} = 300 K were conducted at Kn = 0.04622 and 0.1849 in the uniform microchannel, whose aspect ratio varied between 2.5, and 20. For a given exit pressure, the pressure ratio increased by increasing the channel length. Except for the case with the aspect ratio of 2.5, the heat exchange between the wall and the bulk flow only occurred at the channel entrance region and maintained almost zero after a rapid decrease when the wall temperature was 600 K. In the pressure-driven flow case, the aspect ratio of the microchannel was fixed at 10 with an unchanged pressure ratio of 8. For cold case as the wall temperature was 300 K, there was almost no wall heat flux throughout the whole channel. For hot case as the wall temperature was 600 K, the inlet pressure obtained was higher than that in the cold case and the maximum heat flux occurred at the channel entrance. For case of variable wall temperatures, the wall heat flux distribution was plotted out and provided some idea about the cooling of a plate with various surface heat sources.

Fan et al. (1999) described the DSMC method in more detail and applied it in simulating the 2-D Plane Poiseuille microchannel flow. In their work, the NTC scheme was used to determine the collision pairs within a cell statistically. The VHS model was chosen to model the intermolecular potential between collision pairs and to calculate the post-collision velocities from the pre-collision state. Regarding the gas-surface interactions, the CLL (Cercignani-Lampis Lord) gas surface model was applied to simulate the reflection of the molecules impacting the solid surfaces. The operating flow

was driven by a pressure difference between the two edges with the given incoming flow stream temperature. Other flow properties at the channel inlet and outlet were specified from the states of particles inside the flow field. Satisfactory agreements were obtained between the DSMC results and the analytical results in slip flow regime. When the flow fell into the transition regime, the analytical solutions were distinguished with the DSMC results and failed to predict the flow because of the breakdown of the continuum assumption. The non-linear pressure distribution was resulted from the compressibility of the rarefied flow. As the Kn increased, the profiles of the streamwise velocity became flatter.

Liou et al. (2000) presented a new implicit treatment of the pressure boundary conditions for low-speed microchannel flows. The pressure conditions were imposed by enforcing the mass conservation at the upstream boundary and applying the theory of characteristics at the downstream boundary. The new boundary conditions were verified by comparing the DSMC results with the analytical solutions for the micro-Coutte flow and the micro-Poiseuille flow. It was proved that the defect of analytical flow prediction based on the continuum assumption was not necessarily due entirely to the low-order accuracy in the slip boundary condition. For the micro-Couette flow, the inlet and outlet pressures were both equal to 0.83 atm, while the upper wall moved with a speed of 100 m/s. The inflow temperature and the wall temperatures were both set at 300 K. Two cases with the Kn of 0.08 and 0.16 based on different channel heights were investigated respectively. In comparison with the linear continuum-based result, the DSMC results showed a lower value of slope in the velocity profile near the channel center portion and slight curvatures approaching the wall. This kind of nonlinear wavy behavior became

more significant as the Kn increased and was claimed not to be reported before. For the micro-Poiseuille flow, two cases were investigated at the pressure ratio of 2.5 and 4.54 respectively. The local Kn value varied between 0.055 and 0.12 for the first case and between 0.19 and 0.72 for the second one while the channel height was fixed at 0.4 μm. The results showed the continuum-based model with lower-order slip wall condition can no longer predict the flow properly. Moreover, the mass flow influx from downstream the exit was too significant to be neglected due to the thermal fluctuation. It may take a large portion of the whole mass flux and hence gave the evidence to the unreasonable 'vacuum' boundary condition.

Pan et al. (2000) simulated the stationary gas and the 2-D micro Couette flow using the DSMC method combined with the information preservation (IP) method. The advantage of this modified method is to reduce the statistical error in low speed flow through preserving macroscopic information in the simulated particles and computational cells. It was evident that as the sample size exceeded a certain value, the increasing of the statistical error is negligible. Compared with the results simulated by the original code, using the same sample size, better agreement can be obtained between the simulation results predicted with the IP method and the exact solutions. Although the code implemented with the IP method needs to be run twice as the original code, the sample size is reduced to achieve the steady state; hence, less computation effort is required.

Wu et al. (2001) simulated the T-shaped micro-manifold flow with a new boundary treatment implemented with the particle flux conservation principle. One of the two horizontal edges was considered as the entrance while the other two were treated as the exits. The T shape micro-manifold was uniform with the characteristic length of 1 μm for

each segment. Argon was employed as the testing species. Based on the inlet conditions, the Kn was 0.2, corresponding to the flow in the transition regime. Excellent mass conservation was obtained between the entrance and the exits for the low-speed subsonic flows. Given the same pressure at the two exits, less mass flow would be charged from the one located at the end of the vertical part. When the pressure of the horizontal exit was specified two times as that of the vertical one, the vertical exit can almost be blocked with no more than 3% mass flow passing through it. Some flow properties, such as the velocity, Mach number, temperature and pressure contours were also illustrated.

Fang et al. (2002) extended Liou et al.'s (2000) work by considering the heat transfer in the micro Poiseuille flow case. In their work, the wall temperatures were 323 K while the inflow temperature was 300 K. For both cases, the flow temperature increased gradually in the first half of the channel until it reached the wall temperature. However, for the higher Kn case, a significant temperature decrease occurred in the second half of the channel as the flow developed downstream to the exit. With no regards to the difference in the temperature distribution, the hear transfer between the wall and the bulk flow can only be observed in the first half of the channel for both case. Also, the magnitude of the wall heat flux for the higher Kn case was higher than that for the lower Kn case. Flows in a microchannel containing two rectangular blocks, which were attached to the lower surface, were simulated in the parallel mode by domain decomposition. The temperature at the block top was maintained at 523 K and therefore the temperature jumps along the walls were higher near the two blocks.

Yan et al. (2002) examined the effect of Kn, Re, and Pr on heat transfer characteristic for microchannel flows. The subsonic flow developed between two parallel

plates, which had a constant temperature higher than the inlet flow except at the entrance region. Independence of the results was implemented by repeating the calculations using different mesh sizes and initial 'particle number per cell' respectively. Simulations were conducted for different single gas species as well as the gas mixtures, such as N_2, Ar, H_2, O_2, He-Xe (68%-32%), He-Kr (60%-40%) and He-Ar (58%-42%). The Kn increased and the Re decreased along the channel due to the compressibility. Furthermore, at larger Kn the molecular diffusion dominated. Significant differences were found in wall heat fluxes predicted by DSMC and from the classic Graetz solution, although qualitative agreement was achieved. The heat transfer was highest at the entrance of the heated region because of the largest temperature difference there. A simple expression, which predicted Nu as a function of Pr, Re, and Kn, was given by modifying the correlations presented by Graetz.

Yan et al. (2002) implemented the three-dimensional DSMC code in a parallel way. Flows in a 3-D rectangular microchannel which has a moving upper surface were simulated. Investigations were carried out for flows with equal inlet-outlet pressure and with unequal inlet-outlet pressure as well. Pressure gradient can be observed in all three directions even when the pressure ratio was equal to 1. Also, at a certain cross section, the pressure near the moving surface was higher than that in the other locations. For cases with unequal inlet-outlet pressures, better pumping effect can be achieved by increasing the speed of the moving surface. As the Kn increased, the velocity fields became more uniform. The variation of compression ratio was found to be a function of the Kn and reached its maximum value in the transition flow regime.

Park et al. (2002) simulated the one-dimensional unsteady microflow created by a sinusoidal oscillation input from the left edge. In their work, main attention has been

focused on the nonequilibrium effect near the stagnation wall. Six cases based on different acoustic Reynolds numbers and Knudsen numbers were examined with a fixed frequency and amplitude for the external excitation. It was shown that the effect of the characteristic length on the transient behavior of the working fluid is more significant than the acoustic Reynolds number. Furthermore, more significant nonequilibrium effects at the stagnation wall can be observed due to the small number of reflected molecules from the diffuse wall, which may bring some errors in analyzing the microflow and can not be neglected.

Xue et al. (2003) investigated the micro-Couette flow in the slip and transition flow regimes. The flow properties, such as the velocity, temperature, and pressure distribution, were considered in analyzing the effect of rarefaction. The results calculated from the Burnett equations with the non-corrected and corrected pressure boundary conditions were compared with those achieved from the DSMC simulation. It was indicated that with a modified pressure boundary condition the Burnett equations can predict the flow in the continuum and slip flow regimes properly; the results agree well with the DSMC solutions. However, further into the transition flow regime the Burnett equations failed to predict the wall shear stress and the heat flux. As Kn number increases the temperature jump at the upper and the lower plates increases with a more flattened profile and the velocity slip near the plate also increases. It can also be found that the effect of rarefaction on the heating process is not very significant unless a large difference in the temperature exists between the upper and the lower plate.

Xue et al. (2003) studied the backward facing step microflow using the DSMC method. The effects of rarefaction and compressibility were analyzed by investigating

some typical phenomena of the backward facing step flow, such as the flow separation, recirculation, and reattachment, which can be observed in the normal scale, at micro or sub micro scale. A growth of the Knudsen layer thickness was caused by increasing the Kn, thus leading to a reduction in all the mentioned phenomena. Because of the rarefaction effect, a dramatic flow behavior was observed; that is, there is a sudden jump in the magnitude of the pressure and the velocity right behind the step corner. This jump was considered to be caused by the high number density in the corner surrounded by the two solid walls which act just like a molecular 'collector'. The flow compressibility effect was analyzed by changing the pressure ratios. In the slip flow regime, where the continuum assumption is still valid, the reattachment length and the pressure drop increase as the pressure ratio increases; however, the acceleration near the step doesn't change with respect to the pressure ratio. As the flow falls into the transition regime, imposing different pressure ratios, the pressure recovery becomes less significant at the portion after the step. Because of the rarefaction, the flow accelerates streamwisely at the back of the step in a steady way as if there was no step.

Wang et al. (2003) illustrated the nonideal gas effect of the micro- and nanochannel flows. Instead of using the equation of state, the van der Waals equation was employed in their work in order to investigate the nonideal gas behavior. The velocity and temperature distributions, the skin friction, and heat transfer of surfaces have been predicted using the DSMC code modified with the consistent Boltzmann algorithm (CBA). The results show that the ideal gas assumption may break down when the gas becomes very dense or the channel height is very small even though the Kn is high. As a result, the nonideal gas effect becomes very significant and must be considered in simulation. It was also found

that the nonideal-gas effect can lead to lower skin friction coefficients and different wall heat flux distributions along the wall surface.

Hadjiconstantinou (2000, 2002, and 2003) studied the heat transfer characteristics for the fully developed two-dimensional microchannel flows. The Nusselt number for the flow with the Kn varying from 0.05 to 2 was investigated using the DSMC method while the continuum assumption broke down. With the constant-wall-heat-flux boundary condition, the Nusselt number decreases monotonically with increasing Kn in both flow regimes for the fully accommodating case. Similarly, the constant-wall-temperature boundary condition was considered afterwards to investigate the convective heat transfer characteristics in the transition regime. Qualitative agreement has been achieved compared with the previous study. It was shown that dissipation effect at the wall can not be neglected for its considerable effect on the heat transfer characteristics, which becomes significant as the Kn increases.

Qunwu et al. (2004) examined the low-speed gaseous flows in 2-D microchannels with pressure boundary conditions. The operating microchannel has the dimension of 0.0642 μm in height and 0.0963 μm in length, which gives the aspect ratio of 15. The Kn according to the base case is 0.8 while slight deviation may occur with changing the inflow temperature. In their work, the particles flux conservation was adopted at both the inlet and outlet edges to implement the pressure boundary conditions. For the case with the wall temperature higher than the bulk flow temperature, it was found that the local gas temperature changes only at the entrance and the exit channel region. Moreover, within the whole flow region, a higher temperature difference between the wall and gas

flow causes the gas flow to become more rarefied. Thus, a farther deviation from the linear pressure distribution can be obtained, indicating an enhanced compressibility.

Park et al. (2004) conducted a parametric study of time-periodic oscillatory Couette flows using the unsteady direct simulation Monte Carlo (DSMC) method. The dynamic response of the unsteady Couette flows, such as the velocity profiles, phase angle, wave speed, shear stress, and the penetration depth have been investigated in the entire Knudsen regime ($Kn \leq 100$) with a wide range of Stocks numbers ($\beta \leq 7.5$). Comparing the DSMC results with the predictions of the extended slip model for $\beta \leq 0.25$ in the entire Knudsen regime, and slip flows for $\beta \leq 7.5$, good agreement in the normalized velocity amplitude profile can be obtained and it is believed that DSMC can easily substitute the continuum based slip model. It was found that the velocity amplitude decays exponentially as a function of the distance from the oscillating surface in most of the bulk flow region. However, within the Knudsen layer small deviations from this behavior was observed, which can only be captured by DSMC. In the transition flow regime $0.1 \leq Kn \leq 10$, being predicted by DSMC, the slip velocity increases with increasing Kn for a certain β and the thickness of the Stokes layer decreases with increasing β ($\beta \leq 7.5$). In the free-molecular flow regime ($Kn = 10$), a good agreement was also achieved between the DSMC results and the linearized collisionless Boltzmann solutions for $\beta \leq 7.5$. It was found that the shear stress and the slip velocity amplitude for oscillatory Couette flows are identical to that of the steady plane Couette flows. In their work, the penetration depth, being defined as the distance from the moving wall to the position where the velocity amplitude decays to 1% of its excitation value, for the bounded rarefaction layer is a function of both Kn and β. It becomes a new length scale

in the problem and makes it necessary to redefine the Kn based on the penetration depth instead of the separation distance L. However, without a priori knowledge this is not completed yet in their work.

Wang et al. (2004) proposed a new implicit boundary treatment to overcome the instability of particle-based approaches and speed up the astringency of Liou's method (2000). The modified code was first verified by applying to a pressure-driven micro-Poiseuille flow and the results were compared with those obtained from the N-S equations with slip boundary condition as well as the other boundary treatments. In addition, flows in two types of microgeometries, a straight microchannel with a rectangular orifice and a bended microchannel with a right angle at the corner, were simulated using the new boundary treatments. For the first geometry, it was found that most of the pressure drop occurs across the orifice and the pressure behind the orifice can be even lower than the exit pressure. A larger pressure drop causes higher velocities and a lower temperature behind the orifice. The effect of geometry on the flow behavior is revealed by the reduction in mass flow rates compared with the corresponding straight microchannel flow case. As for the second geometry, the distribution of the average bulk flow temperature is similar to that of the straight microchannel case except for a peak occurring at the corner. The flow decelerates suddenly at the corner with the Mach number lower than the entry flow Mach number and accelerates afterwards. In contrary to the continuum model, no flow separation can be observed at the corner even with a high pressure ratio and the mass flow rates are much higher than those obtained from the N-S equations.

Liu (2004) applied an Artificial-Moving-Wall boundary (AMW) condition in simulating the micro Couette flow in order to obtain a faster convergence rate and reduce the computational time. The partial domain was located either between the wall boundary and the interface or within two interfaces built within the full domain. The simulation was carried out using the modified Bird's code based on the formulation developed by the researcher. Three cases according to different position of the virtual interfaces were established and investigated in the research. Good agreement has been achieved between the results obtained by the previous work and those done by the new boundary settings.

Wang et al. (2005) simulated the gas mixing in microchannel using the DSMC and exposed the inherent effect factors on the micro gas mixing behavior. Two gas species with equal molecular masses were employed in order to avoid the density effect on investigating the flow mixing behavior. The two parallel gas streams entering the 2-D uniform microchannel are separated by a splitter plate with the dimension of one third of the channel length. A quantified parameter, mixing length, was defined to quantitatively characterize the mixing process. The results show that the wall effect on the mixing length is limited even though it plays a key role in the velocity and temperature profiles. On the other hand, it was concluded that the main flow velocity and temperature are the dominate factors for the mixing process in microchannels. The mixing length was found to be almost proportional to the gas main flow velocity and decrease with the increasing temperature. Also, a dimensionless mixing coefficient defined as the mixing length divided by the channel height, was found to be proportional to the Mach number, while inversely proportional to the Kn number.

2.3 Inlet/Outlet Boundary Conditions

The original code developed by Bird implemented the upstream inlet and downstream outlet boundary conditions in DSMC simulation using an explicit way. At the inlet the Dirichlet type of boundary condition is imposed with the known free stream Mach number and the inflow temperature; while at the outlet boundary the flow is assumed to be discharged into a vacuum with no molecules being allowed to return back to the computational domain. This type of boundary treatment is appropriate for the high speed microchannel flow since the thermal velocity of a molecule can be very small in magnitude compared with the mean velocity.

Once the speed of the flow is not high, as is in the subsonic flow and pressure driven flow, however, the magnitude of the mean flow velocity may be of the same order as the most probable thermal speed. Hence, more effort should be attributed to dealing with the thermal motion of the molecules near the boundaries. The molecules leaving out of the outlet boundary can reenter the computational domain while the molecules inside the inlet boundary can also return back upstream the inlet region. According to this analysis new boundary condition is required to be imposed at the inlet and the outlet boundaries. Currently, there are two types of boundary conditions used in simulating the subsonic low speed gaseous flows. One is the pressure boundary conditions with specified inlet and exit pressures, and the other one is specified with a certain mass flow rate and a fixed exit pressure, both of which are more realistic than the inflow velocity boundary condition.

Ikegawa et al. (1990) implemented the pressure boundary conditions at the I/O boundaries by employing the theory of conservation of particles at both of the boundaries. The mean flow velocity U at the boundaries was determined by the number

of molecules flowing in, $N_{in}^{t-\Delta t}$, and out, $N_{out}^{t-\Delta t}$, across the boundary cell interfaces, as indicated below,

$$U(t) = \frac{N_{in}^{t-\Delta t} - N_{out}^{t-\Delta t}}{n \cdot \Delta t \cdot A}, \tag{2.1}$$

$$n = \frac{p}{kT}, \tag{2.2}$$

where n is the number density in the upstream or downstream, Δt is the time step, A is the cross-sectional area, p is the pressure, and T is the gas temperature at the upstream or downstream boundary. The number of flowing-in molecules N_{in} is calculated by

$$N_{in} = \frac{n \cdot C'_m \cdot K}{2\sqrt{\pi}} \cdot \Delta t \cdot A, \tag{2.3}$$

$$K = \exp\left(-\frac{U^2}{C'^2_m}\right) \pm \sqrt{\pi}\frac{U}{C'_m}\left\{1 + erf\left(\frac{U}{C'_m}\right)\right\}, \tag{2.4}$$

$$C'_m = \sqrt{2RT}, \tag{2.5}$$

where C_m is the most probable molecular speed, R is the gas constant, and *erf* is the error function. The number of flowing-out N_{out} is computed by actually accounting the number of particles crossing the boundary. The method was verified by comparing their results with the experimental data in Dong's (1956) work in simulating the 2-D micro Poiseuille flow.

Piekos et al. (1995) enforced the pressure boundary condition by introducing appropriate particles at the I/O boundaries. The macroscopic quantities, such as the pressure at both the inflow and outflow edges and the free stream temperature at the inlet

boundary, were maintained at a given value by means of the boundary treatment. The rarefaction effects in micromechanical devices were investigated in their work.

Nance et al. (1998) introduced a new method to implement the pressure boundary conditions. In their work, the inflow mean velocity is determined cell by cell by means of the per-cell based particle-conservation theory other than just giving a constant inflow mean velocity at the inlet edge in Ikegawa et al.'s (1990) work. Additionally, the particle fluxes crossing the computational domain are determined by the Maxwellian distribution but not through an actual accounting way.

$$\dot{n} = \frac{nC'_m[\exp(-q^2) + \sqrt{\pi}q(1 + erf(q))]}{2\sqrt{\pi}}, \tag{2.6}$$

$$q = s\cos\theta, \tag{2.7}$$

$$(u_{in})_j = \frac{(\dot{n}_+ - \dot{n}_-)_j}{n_{in}A}, \tag{2.8}$$

where s is the speed ratio V/C'_m; V is the mean speed; C'_m is the most probable speed, and θ is the angle between the velocity vector and normal to the boundary element; u is the streamwise velocity; j is the cell number; in indicates the inlet quantities; $\dot{n}_+$ and $\dot{n}_-$ denote the flowing-in and flowing-out particle flux at the inlet boundary respectively. For the outflow, the theory of characteristics was used to implicitly enforce the boundary condition. The resultant equations (for a Cartesian grid) are

$$(\rho_e)_j = \rho_j + \frac{p_e - p_j}{a_j^2}, \tag{2.9}$$

$$a_j = \sqrt{\gamma RT_j}, \tag{2.10}$$

$$(u_e)_j = u_j + \frac{p_j - p_e}{\rho_j a_j}, \tag{2.11}$$

$$(\upsilon_e)_j = \upsilon_j, \tag{2.12}$$

$$(T_e)_j = \frac{p_e}{(\rho_e)_j R}, \tag{2.13}$$

where the subscript e signifies the exit quantities; ρ is the density; P is the pressure; v is the transverse velocity, and a is the local speed of sound. The exit temperature T_e can then be calculated using the ideal gas law with the known exit pressure p_e.

Liou et al. (2000, 2001) followed Nance's method and described it in more detail. At the inlet boundary, the streamwise thermal velocity of the molecules entering the computational domain is randomly sampled with the implement of the acceptance-rejection method. The resulting velocity components, u, v, w, of the flowing-in molecules becomes

$$u = (U_j + 3C'_m)R_f, \tag{2.14}$$

$$v = A\cos\phi, \tag{2.15}$$

$$w = A\sin\phi, \tag{2.16}$$

where R_f represents a random fraction number; the magnitude, A, lies between 0 and ∞, with the distribution function of

$$f_A = \exp(-\frac{A^2}{2RT}), \tag{2.17}$$

and can be determined by

$$A = \sqrt{-\ln(R_f)}C'_m . \tag{2.18}$$

The angle, ϕ, has a uniform distribution from 0 and 2π. That is

$$\phi = 2\pi R_f .$$

The mean velocity at the upstream inlet boundary is determined by a very simple way which is

$$(u_{in})_j = u_j . \tag{2.19}$$

The inflow temperature, T_{in}, the number density, n_{in}, can then be calculated according to the equation of state, the conservation of mass from the give pressure P_{in}, and density ρ_{in}

$$(T_{in})_j = \frac{p_{in}}{\rho_{in} R}, \tag{2.20}$$

$$(n_{in})_j = \frac{\rho_{in}}{m_r}, \tag{2.21}$$

where m_r denotes the molecular mass. At the outlet boundary, the theory of characteristics is taken to deal with the pressure boundary condition. The mean quantities are first determined by the sample average equations

$$u_j = \frac{1}{N_j}\sum u , v_j = \frac{1}{N_j}\sum v , \tag{2.22}$$

$$\rho_j = n_j \cdot m_r , \tag{2.23}$$

$$T_j = \frac{3T_{tr} + \xi_r T_{rot}}{3 + \xi_r}, \tag{2.24}$$

$$p_j = n_j k T_j , \tag{2.25}$$

where T_{tr} denotes the translational temperature; T_{rot} denotes the rotational temperature, and ξ_r denotes the number of rotational degree of freedom.

Step 1: determine the number density of molecules at the exit by

$$(\rho_e)_j = \rho_j + \frac{p_e - p_j}{(a_j)^2}, \tag{2.26}$$

$$(n_e)_j = \frac{(\rho_e)_j}{m_r}, \tag{2.27}$$

Step 2: determine the exit temperature T_e, $(u_e)_j$ and $(v_e)_j$

$$(T_e)_j = \frac{p_e}{(\rho_e)_j R}, \tag{2.28}$$

$$(u_e)_j = u_j + \frac{p_j - p_e}{\rho_j a_j}, \tag{2.29}$$

$$(v_e)_j = v_j. \tag{2.30}$$

Step 3: determine the exit mean flow velocity by sampling

$$(u_e)_j = \frac{1}{N_j}\sum u_e, (v_e)_j = \frac{1}{N_j}\sum v_e. \tag{2.31}$$

Step 4: The implicit determined downstream properties can then be used to calculate the number of the molecules entering the outlet boundary from the number flux function and their velocity components.

The specified mass flow rate and exit pressure boundary condition was employed in the simulation work by Wu et al. (2000, 2001). Their approach ensures the continuity of

flows (mass conservation) automatically when the flow reaches the steady state. Consider a microchannel flow with constant mass flow rate $\dot{m}$, a given free stream temperature, T_i, and the outlet pressure, P_e. The mass flow rate can be calculated as a finite summation of the average value in each boundary cell,

$$\dot{m} = m_r h \sum_{j=1}^{NCY} (n_{in})_j (u_{in})_j \frac{\Delta y}{h}. \tag{2.32}$$

In the above, 'NCY' denotes the number of the cells in the transverse direction; m_r denotes the molecular mass; h is the channel height and Δy is the cell height. Note that $\frac{\dot{m}}{m_r h}$ is the net particle flux crossing some particular cross section so that it can be rewritten as the following

$$\left(\frac{\dot{N}}{A}\right)_{net} \equiv \frac{\dot{m}}{m_r h} = \sum_{j=1}^{NCY} (n_{in})_j (u_{in})_j \frac{\Delta y}{h}. \tag{2.33}$$

A hypothesis of uniform velocity is applied to the inlet conditions:

$$u_{in} = (u_{in})_1 = (u_{in})_2 = \cdots\cdots = (u_{in})_{NCY}. \tag{2.34}$$

By defining the average inlet number density as

$$\overline{n_{in}} = \sum_{j=1}^{NCY} (n_{in})_j \frac{\Delta y}{h}. \tag{2.35}$$

The expression for the inlet streamwise velocity associated with constant flow rate is proposed as

$$u_{in} = \frac{1}{\overline{n_{in}}} \left(\frac{\dot{N}}{A}\right)_{net} = \frac{\dot{m}}{\overline{n_{in}} m_r h}. \tag{2.36}$$

The number density, n_{in}, at the inlet upstream boundary is approximated as the number density interior to the corresponding inlet boundary cell j, i.e.

$$n_{in} = (n_{in})_j, \tag{2.37}$$

which will be updated in each time-step during the computation.

Wang et al. (2004) applied the theory of characteristics at both of the boundaries with known pressure at the inlet and outlet boundaries and the given inlet flow temperature. At the inlet upstream boundary, the velocity components and the inlet flow number density are determined as

$$(u_{in})_j = u_j + \frac{p_{in} - p_j}{\rho_j a_j}, \tag{2.38}$$

$$v_{in} = 0, \tag{2.39}$$

$$n_{in} = \frac{p_{in}}{kT_{in}}. \tag{2.40}$$

2.4 Experimental Work

An integrated microchannel/pressure sensor system has been used by Pong et al. (1994) to examine the pressure distribution in microchannels with uniform cross sections. The pressure distribution measurement along the channel has been carried out by micron-sized pressure sensors integrated with the flow system. The channel has the dimension of 3000 μm in length, 1.2 μm in height, 5 μm in width for one and 40 μm in width for the other. The Kn is varied by employing different gas species, nitrogen and helium, while

the other flow conditions are maintained. For the first generation microsystem integrated with four pressure sensors, it shows that the nonlinearity of the pressure distribution along the channel increases with respect to the inlet pressure as well as the Kn. As for the second generation microsystem, eleven pressure sensors were integrated along the channel in order to get a better spatial resolution, while two more pressure sensors were equipped to measure the inlet and outlet pressure. Moreover, the temperature sensor was also integrated although the measurement was not available at that moment. The measured results reveal that pressure gradients are low at the inlet and at the outlet and an asymptotic pressure distribution does not occur even though the aspect ratio of the channel is more than three hundred.

The design and fabrication of the integrated microsystem have been successfully done by Liu et al. (1995). The uniform and non-uniform microchannels were both involved in their experimental investigation. For the straight channel with a uniform cross section, the nonlinearity of the pressure distribution is observed along the microchannel and is significantly affected by the inlet pressure. Specifically, the pressure gradients near the inlet and outlet edge were found to be smaller than that in the middle of the channel, which can not be predicted by the slip flow model. For flows in non-uniform microchannels, sudden pressure changes across the transitions occurred. This flow phenomenon becomes less distinctive as the inlet pressure decreases. The corresponding numerical modeling has also been accomplished using the N-S equations with the slip boundary conditions. Good agreement was obtained between the numerical results agree and the experimental data.

Shih et al. (1996) conducted the experimental test using the microchannel with the dimension of 4000 μm × 40 μm ×1.2 μm. It was observed that the Kn increases along the microchannel while the outlet Kn is fixed at 0.16 for helium by imposing the atmospheric condition at the channel exit. Moreover, at a certain position the Kn decreases by increasing the inlet pressure. Good agreement can be achieved between the experimental results and the analytical solutions, which is based on the continuum model with slip boundary condition, by applying an appropriate ETCA (effective tangential accommodation coefficient). As for the nitrogen flow, the pressure drop along the channel from the analytical solution is more rapid than that from the experiment observation. When the inlet pressure exceeds 0.27 MPa absolute, an apparent deviation can be found from the mass flow rate prediction, which indicates that more gas flows through the channel than expected.

Li et al. (2000) fabricated two micro constriction devices, the micro orifice plate and the micro Venturi tube, to investigate the microflows experimentally. The Orifice- or the Venturi-element is placed at the center of the microchannel with the dimensions of 4000 μm ×40 μm ×1.0 μm. The mass flow rate measured experimentally in either device is much smaller than that from the analytical prediction of the straight channel case due to their obstructions. Moreover, the orifice flow rate is only equal to half of the 'Venturi' flow rate due to the significant resistance caused by the orifice. On the other hand, more pressure drop can be caused by the Venturi constriction rather than the orifice construction. Therefore, the micro Venturi is ideal to be utilized to construct a micro flow meter for its higher sensitivity. It is also demonstrated by the pressure distribution that

flow separation may occur with a very small Reynolds number and possibly a micro vortex can develop upstream and downstream the obstruction.

Cheng (2003) investigated the series and parallel microchannel flows experimentally. The series microchannel contains three uniform segments, the width of which is 10 μm, 20 μm and 30 μm respectively. The effect of Kn has been explored by switching the channel height from 0.6 μm to 1.6 μm. It was observed that the mass flow rate is independent of the sequence of the segments. The analytical solution based on the slip flow model indicates a 10% mass flow reduction compared with the experimental measurements. It was also found that the pressure distribution relies a lot on the sequence of the segments. In the parallel microchannel system, three kinds of geometries corresponding to different transition sections were performed. The mass flow rate is sensitive to the shape of the branching sections. The minor loss depending on the detailed geometry of the branching sections, however, has no evident effect on the pressure distribution.

2.5 Summary and Objectives

The DSMC method developed by Bird has been widely used in investigating the flows in different microgeometries. Good agreement has been achieved between the DSMC results and the analytical solutions in the continuum regime and also in the slip regime with high order boundary conditions. Qualitative agreement has also observed between the DSMC results and the experimental data. A summary of the method itself and its application will be presented in the following.

2.5.1 Physical modeling and the application

- Knudsen number (Kn), which is defined to judge how rarefied the flow is, can be varied by either changing the characteristic length of the geometry or by changing the number density of the flow.

- The VHS (Variable Hard Sphere) model is the most popular model in simulating the collisions among molecules not only because of its simplicity in implementation but also for its good approximation to the real intermolecular potentials. The NTC scheme is adopted to determine the collision pairs and makes the computational time proportional to the number of the simulated particles, which considerably reduces the computational effort.

- To account for the gas-surface interactions in microchannel, the diffuse reflection model proved to be adequate and has been widely used in most of the research. The molecules, reflected from the channel surfaces with full thermal accommodation coefficient, are assumed to have the same temperature as the wall and the reflection direction is determined by random.

- Three types of I/O boundary conditions are currently considered in DSMC simulations: the Dirichlet type of boundary conditions, the pressure boundary condition, and the mass flow rate condition. Currently, the pressure boundary condition is the commonly used one, which is implemented by means of introducing particles, applying the theory of characteristics, or enforcing the conservation of the particle flux at the channel edges.

- A lot of flow investigations have been already conducted in some simple geometries, such as the uniform microchannel, the two dimensional duct with a

cavity, the straight microchannel with a solid core or a rectangular orifice inside, the T-shape micro-manifold, the bended microchannel, and the three-dimensional rectangular channel with a moving surface.

- The heat transfer characteristics of gas mixtures have been explored and also the gas mixing process has been investigated in a straight microchannel.

2.5.2 Advances in DSMC

- The information preservation (IP) method was combined to the original DSMC method in order to reduce the statistical error in low speed flow. The overall computational effort will be much less than that spent for the original code to get the steady state although the code should be run twice.

- The MLG (monotonic Lagrangian grid) method combined with the original DSMC has been developed to construct and maintain data structures for many-particle simulations. The key advancement of this method is to make the grids automatically adapt the change of the flow properties and achieve the best resolution possible for a given grid size.

- Unsteady microflow has also been taken into consideration imposing a time dependent boundary condition, which makes the DSMC simulation more applicable in the real microsystems.

2.5.3 Objectives

In the present thesis, a systematic research work using the DSMC in flow simulation will be presented, which investigates some of the simplest flow configurations in MEMS,

such as the straight uniform microchannel flows, the parallel and series microchannel flows. For the uniform microchannel flow, both the supersonic and the subsonic flow will be modeled to conduct a parametric analysis. The effect of the Kn on the wall slip phenomena, the flow velocity, the development of the thermal layers, the pressure distribution, and the wall heat flux will be explored. The parallel and series microchannels, being the most typical configurations in microfluidic systems, have not been thoroughly studied using the DSMC. In the present study, the diffuse effect will be investigated by applying different wall temperatures to the two uniform segments of the series microchannel. Also, helium and argon will be employed in simulation respectively to investigate the effect of the gas species. In the parallel channel cases, the flow recirculation phenomenon will be evaluated quantitatively by defining a parameter named the developing coefficient. Furthermore, gas mixing in a T-shape micromixer will be simulated using the DSMC, which has never been implemented in the previous work. The effects of the Kn, the inlet pressure, the free stream temperature, and the wall temperature on the mixing behavior will be investigated.

Chapter 3

Numerical Modeling and the Direct Simulation Monte Carlo Method

3.1 Microchannel Geometries and Flow Parameters

Four types of channel configurations: the uniform microchannel, the parallel microchannel, the series microchannel, and the T-shape microchannel, have been employed in the current work as shown in Figure 3.1 schematically. Figure 3.1 (a) shows the 2-D uniform microchannel with the height H and the length L. Figure 3.1 (b) shows the 2-D series microchannel, which consists of two uniform segments. The lengths of the two uniform segments are l_1 and l_2 respectively, with corresponding heights, h_1 and h_2. The computational domain of the series channel was established as shown in Figure 3.2 (a). The surfaces are added and treated as diffuse reflect walls, and a rectangular section at the lower left corner was excluded. Also, a symmetric boundary was imposed at the upper edge. Figure 3.1 (c) shows the 2-D parallel microchannel, which contains a main channel connected to two parallel uniform sections. The two parallel sections have the same length l and the same height h, and are separated by a gap with a height s. The main channel height is represented by H while the whole length is represented by L, and the simulation was carried out in the computational domain as shown in Figure 3.2 (b). Figure 3.1 (d) shows the T-shape microchannel with two inlets along the vertical axis and one outlet along the horizontal axis. The widths of the two inlets are l and the height of the outlet is h. The computational domain was established similarly as the previous configurations as shown in Figure 3.2 (c).

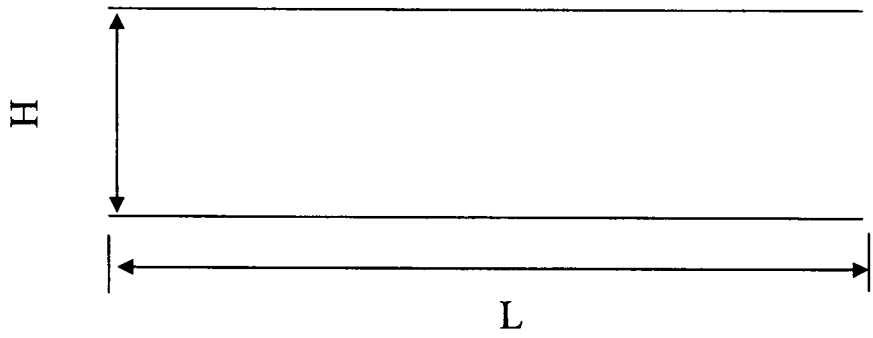

Figure 3.1 (a): Schematic of the uniform microchannel geometry.

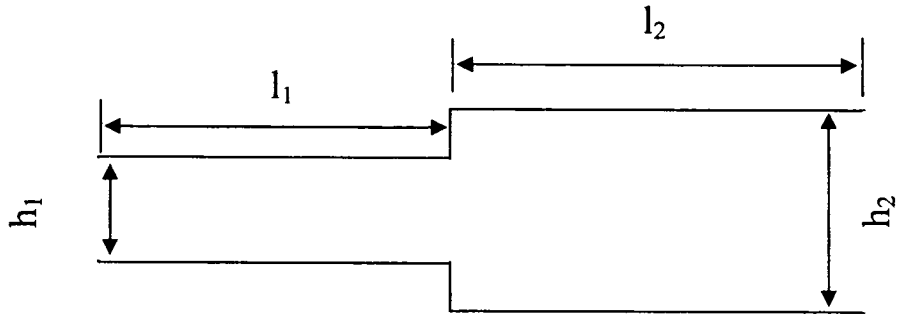

Figure 3.1 (b): Schematic of the series microchannel geometry.

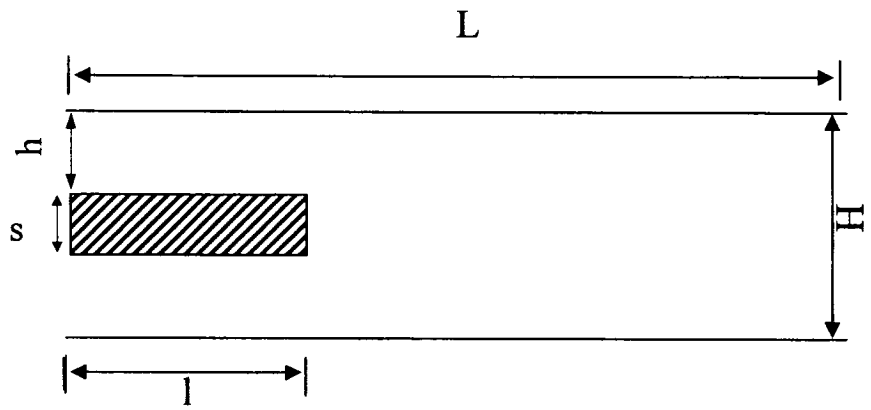

Figure 3.1 (c): Schematic of the parallel microchannel geometry.

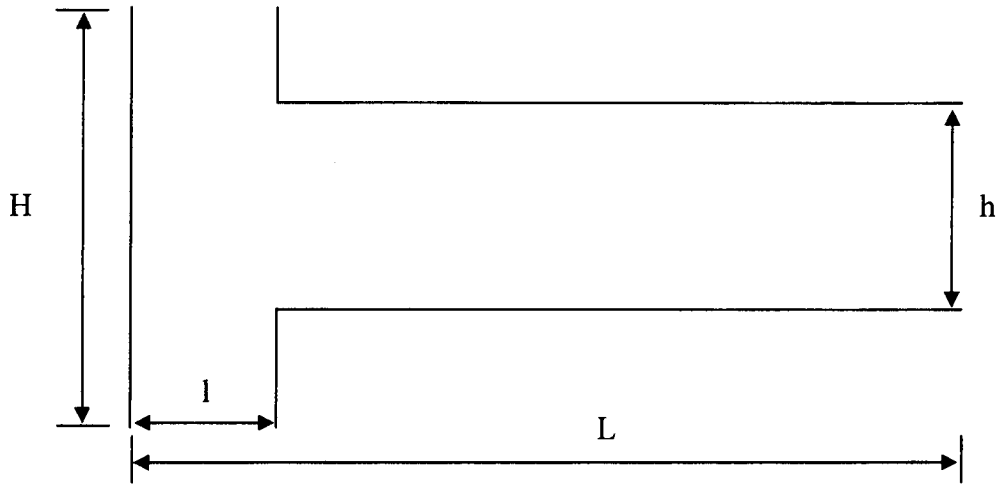

Figure 3.1 (d): Schematic of the T-shape microchannel geometry.

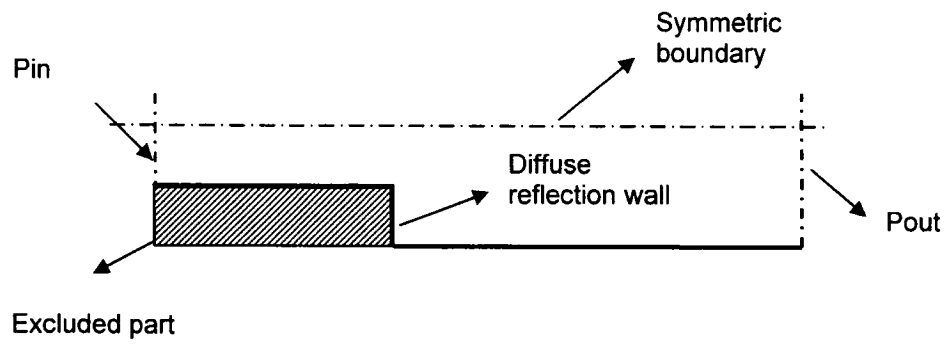

Figure 3.2 (a): Boundary conditions for the series microchannel flow.

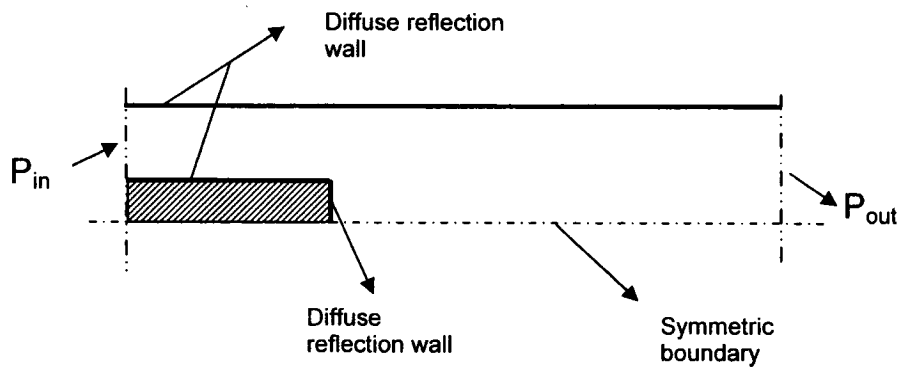

Figure 3.2 (b): Boundary conditions for the parallel microchannel flow.

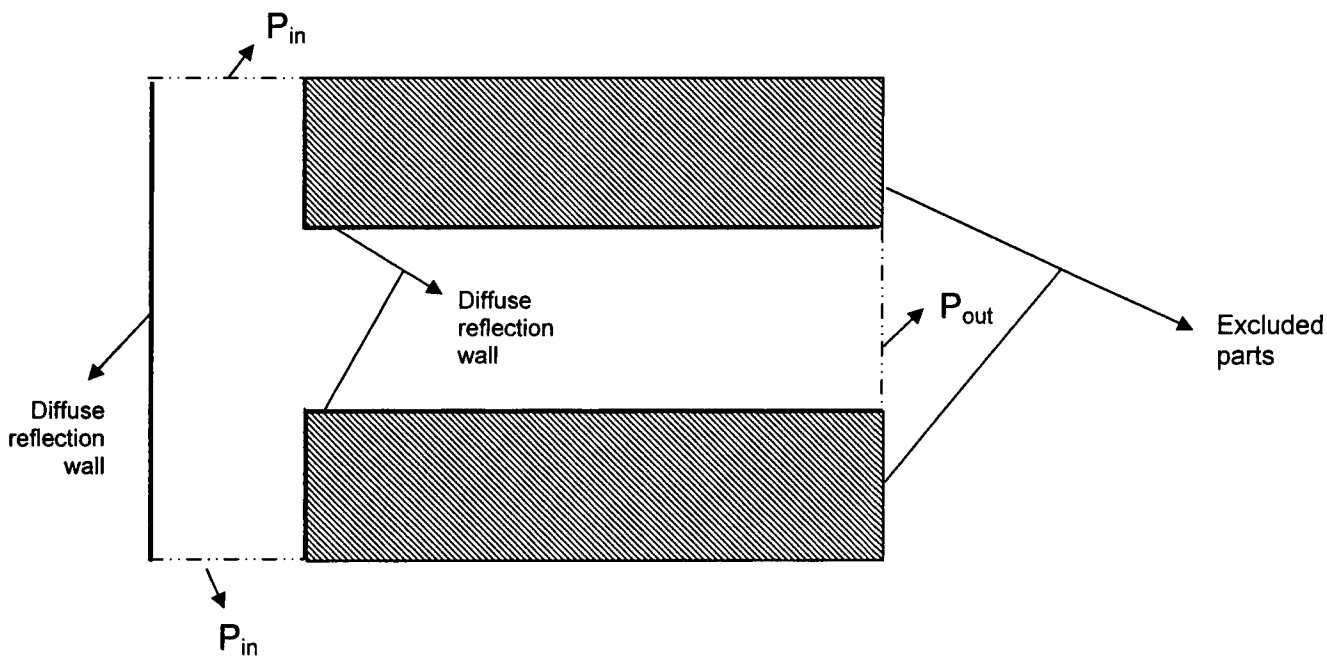

Figure 3.2 (c): Boundary conditions for the T-shape microchannel flow.

For the supersonic case in the uniform microchannel, the free stream Mach number, M_∞ and the incoming flow temperature T_∞ are set at the inlet. In order to generate the free stream supersonic flow, a portion of the wall at the entrance region, 10% of the whole channel, is kept as a specular reflector (discussed in detail later in this chapter). As for the subsonic cases operated in all the four configurations, gas flows are driven by the pressure ratio, the inlet pressure, P_{in}, over the outlet pressure, P_{out}, which are specified at the inlet and outlet boundaries, respectively. Also, the free stream temperature, T_{in}, is specified at the inlet boundary.

The Kn for the microchannel flow, which indicates the flow rarefaction as mentioned in chapter I, is defined as

$$Kn = \frac{\lambda}{H_c}, \tag{3.1}$$

where λ represents the mean free path can be calculated by

$$\lambda = \frac{1}{\sqrt{2}n\sigma}, \tag{3.2}$$

where n is the number density of the gas flow and σ is the cross section. Using the hard sphere model, the cross section of a gas species with fixed molecular diameter d is defined as

$$\sigma = \pi d^2. \tag{3.3}$$

The Kn of microchannel flow varies either by changing the channel height or by changing the number density of the flow. In our work, both options will be taken to obtain gas flows with different Kn.

3.2 Numerical Solutions and Flow Samplings

The DSMC method introduced by Bird (1976) is used to simulate the microchannel flow in a physical way using a particle-based model. That is, the macroscopic properties in the flow field, such as the pressure, velocity, temperature, and density, are determined by sampling the microscopic quantities of the simulated particles based on each cell within the computational domain.

First, a number of simulated particles, each of which represents a certain number of real molecules, are placed into each cell and are set into motion within a very short interval. This time interval Δt should be smaller than the mean collision time in order to discretize the molecular movement, and so the interactions among the molecules can be neglected. Once a particle reaches either the channel wall or the I/O boundary, its position and velocity are adjusted according to the imposed boundary conditions. Second, the location of each particle is indexed by recording the subcell number and the cell number where the particles are located. Third, the collision partners are randomly selected from particles with the restriction that during a time step, the binary collisions are permitted only between the particles within the same cell. The probability of treating a given pair as a collision one is the function of the relative speed between the two participative particles. Also, the post-collision state of the involved pair is determined stochastically, conserving momentum and energy with the post-collision angles selected from kinetic theory distribution. Afterwards, the macroscopic properties are sampled by the weighting average of the microscopic properties based on each cell. The whole procedure needs to be repeated for an appropriate number of iterations until steady state is achieved.

3.2.1 Network setting and time step

In the present work, the computational domain for each configuration was divided into a number of rectangular cells, each of which contains four subcells with the 2×2-subcell structure. The 2-D cell dimension has the same order as the mean free path λ in order to ascertain absence of large gradients of macroscopic properties within a cell. The subcell is used to facilitate the choice of collision pairs by assuming that collisions only happen between two molecules in neighboring subcells within a cell. At the initial time, several simulated particles are assigned in each cell with a thermal velocity, and a certain location determined probabilistically. Each simulated particle represents a large amount of real molecules in simulation. The number of the simulated particles should be sufficient enough to minimize the statistical error, but not be too large to exceed the computational capacity. Meanwhile, the number of real molecules per particle can not be too large to be impractical since all these molecules are assumed to have the same properties. A reasonable network, which is composed of appropriate number of cells as well as the simulated particles, will provide good accuracy for the numerical results. The independence test for these factors will be performed individually later in this chapter.

After a proper network setting, the time step Δt was chosen to encourage the evolution of the molecular motions. The time step used in the cases is determined as

$$\Delta t = \frac{1}{3}\frac{\Delta x_d}{c'_m}, \tag{3.4}$$

where Δx_d is the cell dimension and c'_m represents the most probable molecular speed for the flow of temperature T and is defined by

$$C_m' = \sqrt{2RT}\,, \tag{3.5}$$

where R is the gas constant . The time step was chosen to be less than the mean collision time in order to make sure that each molecule can reside within the same cell for at least several time steps.

3.2.2 Gas-wall surface interaction

The most common models to treat the gas-surface interactions are specular and diffuse reflection models and some combination of these. In our work, with the given temperature of boundary walls, the diffuse reflection model is mainly used except that in the supersonic cases 10% the length of the wall from the entrance is considered as a specular reflector. As is expected from the specular reflection model, during the molecule-wall interaction process, the magnitude of the molecular velocity does not change while the reflected angle is equal to the incident angle. For the diffuse reflection model (Bird, 1994), the wall surfaces are considered as diffuse reflector with full thermal accommodation coefficient, $\alpha = 1$. The outgoing velocity is randomly assigned according to a half-range Maxwellian distribution determined by the wall temperature. The accommodation coefficient α is defined as

$$\alpha = \frac{E_i - E_r}{E_i - E_w}, \tag{3.6}$$

where E_i represents the energy of incident molecules on a surface, E_r is the energy of reflected molecules from the surface, and E_w is the energy molecules would have if they acquired energy from the wall at T_w.

The velocity components u, v, w of the reflected molecules are determined as:

$$u = \sqrt{-\log R_f} \cdot C_m' \cdot \sin[2\pi \cdot R_f], \tag{3.7}$$

$$v = \pm\sqrt{-\log R_f} \cdot C_m', \tag{3.8}$$

$$w = \sqrt{-\log R_f} \cdot C_m' \cdot \cos[2\pi \cdot R_f], \tag{3.9}$$

$$C_m' = \sqrt{2\frac{k}{m}T_r}, \tag{3.10}$$

where R_f is a uniformly distributed random fraction between 0 and 1; C_m' is the most probable thermal velocity for a molecule at the reflection temperature T_r which is equal to the wall temperature, T_w, according to the diffuse reflection model. The positive and negative symbol corresponds to the lower and upper wall respectively; k is the Boltzmann constant and m is the molecule mass.

3.2.3 Boundary conditions

In the supersonic cases, the free stream boundary condition is applied at the inlet boundary, whereas the leaving fluxes are neglected. At the outlet boundary, for high-speed microchannel flows, a vacuum is imposed so that no molecules are allowed to reenter the computational domain. In this condition, the particles are simply removed from the calculation domain once they encounter the outlet edge.

Much more effort should be contributed to the boundary treatment for subsonic cases. If the flow is subsonic at the exit, the most probable thermal speed of the molecules can be the same order of magnitude as the mean flow velocity. Thus, it is possible for the molecules to reenter the computational domain. Therefore, it is not reasonable to assume a perfect vacuum environment at the exit due to the existence of the

non-neglected backflow. Otherwise, if the reenter mass flow rate is neglected, the flow speed near the outlet region may exceed the accurate value in a real case, which somehow accelerates the internal flow especially for the flow near the exit region. In our work, the pressure boundary condition applied at the I/O boundary for subsonic cases was developed by Wang et al. in 2004. This treatment is proved to have a better efficiency as well as a better astringency than the other methods (Wang et al., 2004).

With the given pressure P_{in} at the inlet and P_{out} at the outlet, the theory of characteristics was used at both of the I/O boundaries. Knowing the inflow temperature, T_{in}, the inlet number density can be calculated from the equation of state,

$$n_{in} = \frac{p_{in}}{kT_{in}}. \tag{3.11}$$

The theory of characteristics was applied based on each boundary cell and the cell-based inflow velocity can be calculated and updated per iteration as,

$$(u_{in})_j = u_j + \frac{p_{in} - p_j}{\rho_j a_j}, \tag{3.12}$$

$$(v_{in})_j = v_j, \tag{3.13}$$

where the subscript j indicates the boundary cell j, and in signifies the inlet quantities; ρ is the density; p is the pressure; v is the transverse velocity; a is the local speed of sound.

For the downstream boundary, the same method is applied whereas the temperature of the exit flow needs to be determined from inside the computational domain. The equations are similar to those applied at the upstream boundary and was defined as,

$$(\rho_e)_j = \rho_j + \frac{p_e - p_j}{a_j^2}, \tag{3.14}$$

$$(u_e)_j = u_j + \frac{p_j - p_e}{\rho_j a_j}, \tag{3.15}$$

$$(\upsilon_e)_j = \upsilon_j, \tag{3.16}$$

$$(T_e)_j = \frac{p_e}{(\rho_e)_j R}, \tag{3.17}$$

where the subscript e signifies the exit quantities; the exit temperature T_e can then be obtained using the ideal gas law with the known exit pressure P_e.

As the cell-based inflow velocity and the temperature at either the upstream inlet boundary or the downstream outlet boundary are calculated, the molecules entering the computational domain can be determined according to the Maxwellian equilibrium distribution function. This procedure introduces the inflow from the upstream and the backflow from the downstream exit. The resulting velocity components, u, v, w, of the flowing-in molecules from the upstream becomes

$$u = ((u_{in})_j + 3C_m^{'})R_f, \tag{3.18}$$

$$v = A\cos\phi + (v_{in})_j, \tag{3.19}$$

$$w = A\sin\phi, \tag{3.20}$$

$$C_m^{'} = \sqrt{2RT_{in}}, \tag{3.21}$$

where R_f represents the random fraction number; the magnitude, A, lies between 0 and ∞, with a distribution function

$$f_A = \exp(-\frac{A^2}{2RT}), \tag{3.22}$$

and can be determined by

$$A = \sqrt{-\ln(R_f)}C_m^{'}, \tag{3.23}$$

The angle, ϕ, has a uniform distribution from 0 and 2π. That is

$$\phi = 2\pi R_f . \tag{3.24}$$

Similarly, at the downstream exit boundary, the thermal velocity for a molecule entering the computational domain is

$$u = ((u_e)_j - 3C_m^{'})R_f , \tag{3.25}$$

$$v = A\cos\phi + (v_e)_j , \tag{3.26}$$

$$w = A\sin\phi , \tag{3.27}$$

$$C_m^{'} = \sqrt{2R(T_e)_j} . \tag{3.28}$$

3.2.4 NTC scheme and VHS model

The no-time-counter (NTC) scheme, introduced by Bird (1994), was used to determine the collision pairs within a cell. This scheme makes the computational time to be proportional to the number of the simulated particles, N, and significantly saves the computational effort. Within a cell of volume V_c, the collision probability P between two simulated particles, each of which representing F_N real molecules, over a time step, Δt, is given by Bird (1994) as:

$$P = \frac{F_N \sigma_T C_r \Delta t}{V_c} \tag{3.29}$$

and the corresponding maximum value is

$$P_{\max} = \frac{F_N (\sigma_T C_r)_{\max} \Delta t}{V_c} \tag{3.30}$$

where σ_T is the total cross section; C_r is the relative speed, and $P_{\max}$ is the maximum collision probability.

The average number of real molecules in the cell is nV_c and the average number of simulated molecules is

$$N = \frac{nV_c}{F_N} \tag{3.31}$$

Using the NTC scheme, $(1/2)N\overline{N}F_N(\sigma_T C_r)_{\max}\Delta t / V_C$ pairs are chosen from the cell at each time step, where N denotes the fluctuating quantity and $\overline{N}$ is the average value. The collision procedure is counted cell by cell. As mentioned before, the collision pair of molecules was chosen randomly within the same cell. Afterwards, for a certain pair, the collision is determined by the probability

$$\frac{\sigma_T C_r}{(\sigma_T C_r)_{\max}} . \tag{3.32}$$

The simulated particles will move in the next step according to the post-collision molecular velocity. The distance covered by the particles in each direction is equal to the time step multiplied by the corresponding velocity components.

Regarding the intermolecular collision, energy and momentum should be conserved based on the kinetic theory. The aim in solving the collision is to determine the post-collision velocities of the collision pair via its pre-collision state. Many collision models, such as the inverse power low model, the hard sphere model, the variable hard sphere

model, the variable soft sphere model, the general hard sphere model, the Maxwell model and the other models concerning the attractive potential have been introduced to accurately predict the binary intermolecular collision.

In the present work, the Variable Hard Sphere (VHS) model introduced by Bird (1994) is used to model the intermolecular potential between collision pairs and to calculate the post-collision velocities from the pre-collision state. The VHS model has been widely used because of its simplicity and its good approximation to real intermolecular potential, where the real gas temperature exponent of the coefficient of the viscosity has been counted. The diameter d of molecules is considered as a function of C_r, which can be described as the function of a simple inverse power law υ, so that

$$d = d_{ref}(\frac{C_{r,ref}}{C_r})^{\upsilon}, \tag{3.33}$$

where the subscript '*ref*' denotes the reference values at a reference temperature T_{ref}. And the deflection angle is given by

$$\chi = 2\cos^{-1}(\frac{b}{d}), \tag{3.34}$$

where b is the distance of closest approach of the undisturbed trajectories in the center of mass frame of reference for a collision pair. Hence, according to the VHS model the total cross-section is,

$$\sigma_T = \sigma_{ref}(\frac{c_r^{\,2}}{c_{r,ref}^{\,2}})^{-\upsilon}. \tag{3.35}$$

In the application of this model, σ_{ref}, T_{ref} and υ are known parameters. For the molecular collisions, C_r is determined and the value of σ_T can be calculated.

3.2.5 Flow sampling

The macroscopic properties are sampled by the weighting average of the microscopic properties based on each cell. Also, for the steady flow studied in the present work the resulting macroscopic flow properties are also sampled by time averaging.

The flow velocity $\vec{V}$ and the transitional temperatures T_{tr} can be calculated as

$$\vec{V} = E(\vec{C}) = \int \vec{C} \cdot f(\vec{C}) d\vec{C}, \tag{3.36}$$

$$3RT_{tr} = E(\vec{C}^2) = \int \vec{C}^2 \cdot f(\vec{C}) d\vec{C} - \vec{V}^2, \tag{3.37}$$

where $f(\vec{C})$ is the velocity distribution function in each cell; $\vec{C}$ is the thermal random velocity. Since the number of the simulated particles is sufficient enough, the integral can be replaced by

$$f(\vec{C}) = \frac{1}{N} \sum_{i=1}^{N} \delta(\vec{C} - \vec{C}_i), \tag{3.38}$$

where N denotes the number of the particles within the cell, while $E(\vec{C})$ and $E(\vec{C}^2)$ can be substituted by

$$E(\vec{C}) = \frac{1}{N} \sum_{i=1}^{N} \vec{C}_i, \tag{3.39}$$

$$E(\vec{C}^2) = \frac{1}{N} \sum_{i=1}^{N} \vec{C}_i^2 - E(\vec{C})^2. \tag{3.40}$$

Hence, the flow velocity and the transitional temperature can be obtained by

$$\vec{V} = \frac{1}{N} \sum_{i=1}^{N} \vec{C}_i, \tag{3.41}$$

$$3RT_{tr} = \frac{1}{N}\sum_{i=1}^{N}\vec{C}_i^2 - (\frac{1}{N}\sum_{i=1}^{N}\vec{C}_i)^2 . \tag{3.42}$$

Only equilibrium gas is considered in the present work and the vibration energy is neglected so that the overall temperature T is the weighted average of the translational temperature T_{tr}, and the rotational temperature T_{rot}:

$$T = \frac{3T_{tr} + \xi_r T_{rot}}{3 + \xi_r}, \tag{3.43}$$

$$T_{rot} = \left(\frac{2}{k}\right)\frac{\overline{\varepsilon_{rot}}}{\xi_r}, \tag{3.44}$$

where ξ_r denotes the number of rotational degrees of freedom, and ε_{rot} is the sample average of molecular rotational energy. In the case with $\xi_r > 1$, rotational energy of molecules is included and the Larsen-Borgnakke model was applied in simulation. Based on this model, the collision is treated to be inelastic and the total energy is reassigned between the transitional and internal modes, which improves the physical realism. The process to deal with the Larsen-Borgnakke model has been described in detail in Bird's (1994) book. The wall heat flux can be evaluated from:

$$q = \frac{\left[\left(\sum_{i=1}^{nt}\varepsilon_{tr} + \sum_{i=1}^{nt}\varepsilon_{rot}\right)_{inc} - \left(\sum_{i=1}^{nt}\varepsilon_{tr} + \sum_{i=1}^{nt}\varepsilon_{rot}\right)_{reflect}\right]\cdot F_N}{\Delta t \cdot (1 \cdot \Delta x_d)}, \tag{3.45}$$

where nt is the total number of simulated molecules that strike the wall during the sampling time period Δt, and ε_{tr} is the sample average of molecular transitional energy; while the subscript *inc* indicates the incident property and *reflect* refers to the reflected value.

3.3 Accuracy of the Numerical Results

Unlike conventional CFD solvers, there are three factors that can affect the accuracy of the simulation results: the number of cells in the computational domain or mesh size, the number of particles per cell, and the number of real molecules represented by each simulated particle (also called 'scaling factor'). The mesh size should be big enough to satisfy the accuracy requirement without exceeding the computer capacity. In addition, for a given problem the total number of molecules is fixed, which means that increasing the number of particles per cell will cause the scaling factor to decrease, both of which lead to a more accurate solution. Therefore, the dependence of these two factors will be tested at the same time.

The mesh size independence was implemented by repeating the simulation with different cell dimensions in a short uniform microchannel with a sufficient number of simulated particles maintained. In the present study, the cell dimension was set to be less than the inlet gas mean free path, since the mean free path increases along the whole channel due to the pressure drop. Therefore, if the cell dimension is appropriate compared with the inlet mean free path, the requirement of accuracy will be automatically satisfied along the rest of the entire channel.

For the channel with a height of 1 μm and a length of 5 μm, computations were first carried out with mesh size of 25×40, 50×50, and 60×80 respectively, corresponding to cell dimensions of 0.305, 0.366 and 0.731 times the inlet mean free path in the direction normal to the flow. Ilgaz and Çelenligil (2003) found that the cell dimension can be much greater than the local mean free paths in directions where the gradients of the flow properties are small, and that the time step could also been enlarged accordingly. This

statement was proved in the present work by conducting a case with a mesh size of 50×250, which gives equal cell dimensions in both directions. Figures 3.3 (a) and (b) show the comparison of the pressure distribution along the channel and the streamwise velocity profiles at the channel's mid-span based for different mesh sizes. It can be found that the mesh size (50×50) with the corresponding cell dimension in both directions meets accuracy requirements and that the large cells in the flow direction do not affect the solution.

For the cases with channel heights of 0.5 μm and 0.1 μm, mesh sizes of 50×50 and 25×50 were selected, which correspond to the cell dimensions much smaller than the required ones. As expected, these mesh sizes make the computation process more expensive. In fact, it was found that although the coarser mesh (10×20) can also provide a good prediction of the velocity of the bulk flow with less computation effort, it is unable to capture the velocity information near the wall. Therefore, the number of grids needs to be sufficient not only to obtain high accuracy but also to prevent any information from being missed during the prediction of the flow. For the parallel and the series microchannel cases, the cell dimension was selected based on the grid independence tests for the uniform microchannel case.

Independence of the number of simulated particles was checked also in the uniform microchannel. Four cases were carried out with an average number of 2, 5, 13, 20, and 30 simulated particles in each cell. These values correspond to the fixed scaling factor of 3.2×10^{10}, 1.2×10^{10}, 5.0×10^{9}, 3.0×10^{9}, and 2.0×10^{9}. Figures 3.4 (a) and (b) show the effect of the number of simulated particles on the pressure distribution and centerline temperature distribution along the channel,

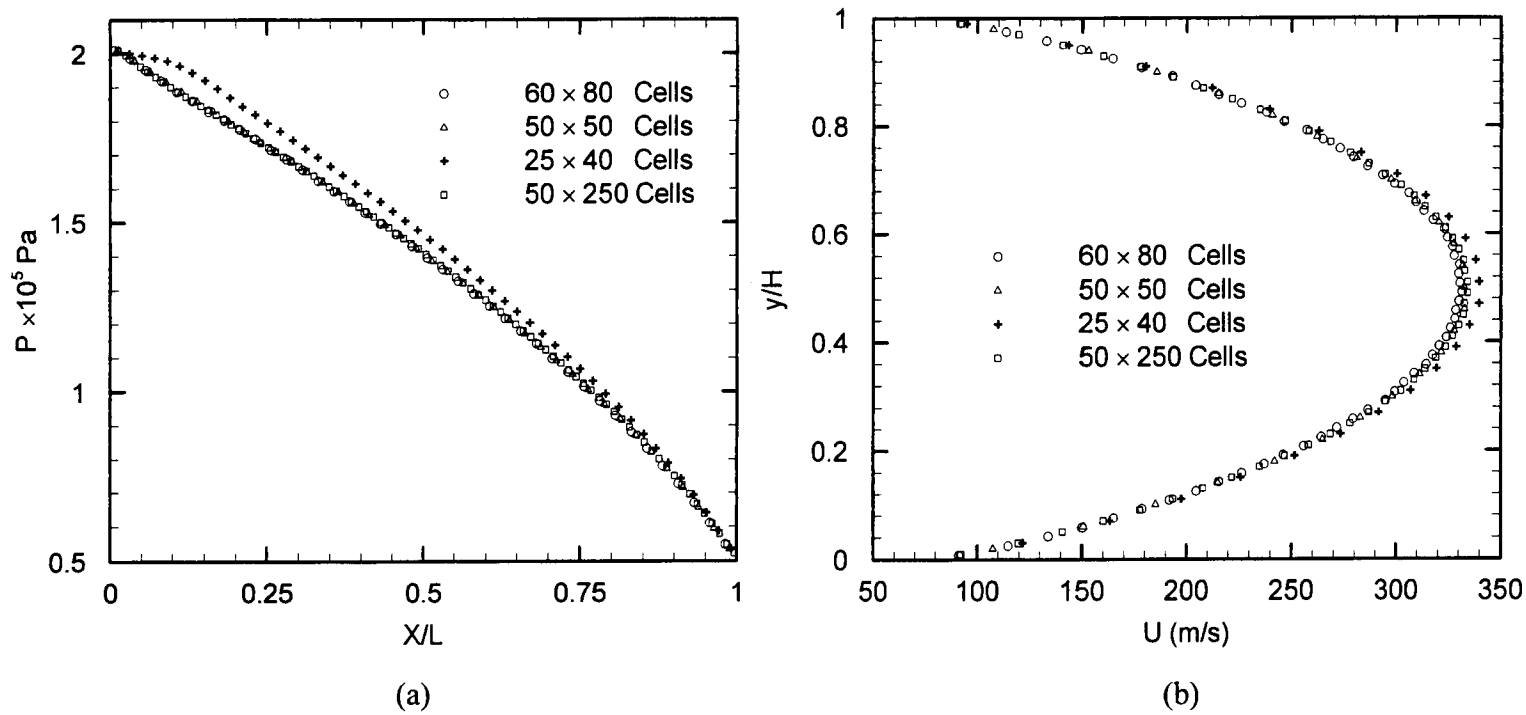

Figure 3.3: Mesh size effect on: (a) the pressure distribution along the uniform channel, (b) the streamwise velocity profiles at the channel mid-span.

and the velocity profiles at different cross sections respectively. It can be noted that the centerline temperature is more sensitive to the number of particles, especially near the channel exit. Similarly, deviation can be observed from the velocity profiles near the channel outlet in Figure 3.4 (b). This can be explained by the fact that as the pressure decreases along the channel, the flow becomes more rarefied. As a result, few molecules are contained in the cell near the channel exit. Therefore, when the scaling factor is fixed the number of simulated particles contained in one cell decreases along the channel, causing significant differences in the velocity profiles near the channel exit. Similar tests were also conducted in the parallel and series microchannels, although the results are not presented here. It can be concluded that using 20 simulated particles per cell, with a corresponding scaling factor on the order of 10^9, yields good accuracy in the numerical results without using too many computational resources.

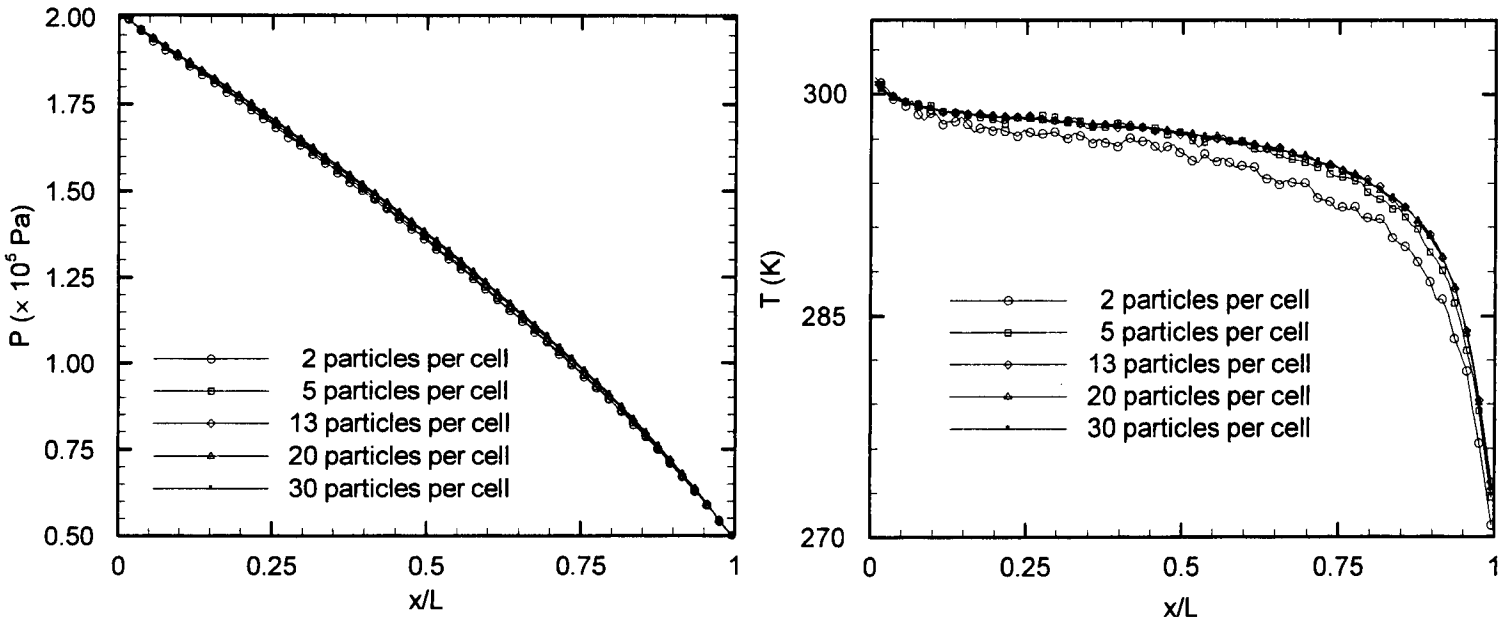

(a)

Figure 3.4 (a): Effect of the average number of simulated particles per cell on the pressure and centerline temperature distributions;

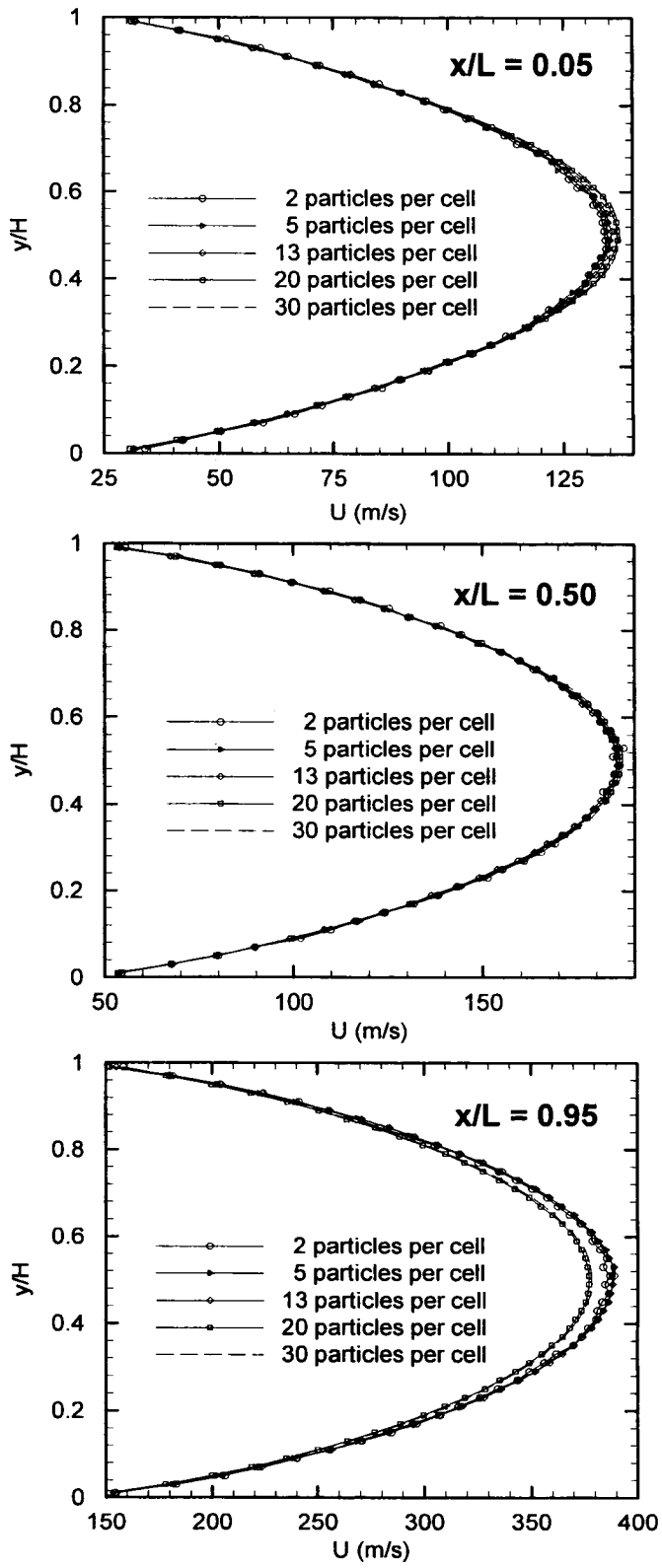

Figure 3.4 (b): Effect of the average number of simulated particles per cell on velocity profiles at channel inlet, mid-span, and outlet.

Chapter 4

Supersonic Flow in Uniform Microchannels

4.1 Code Verification

In order to verify the current DSMC code used for supersonic microchannel flows, the present results were compared with those presented by Liou et al. (2001). The flow conditions were fixed at certain values as shown in Table 4.1 and the testing species was nitrogen as was the case in Liou et al. (2001). Figure 4.1 shows the difference of the streamwise velocity profiles at x/L = 0.5 and it can be observed that the two curves agree well with a maximum deviation of less than 2.5% occurring at the channel center. Good agreement can also be obtained in the centerline temperature distribution as shown in Figure 4.2, with a deviation of approximately 7% after x/H = 1.5.

In the present study, 114300 simulated particles were assigned to the computational domain meshed by 100×60 cells, while in Liou et al.'s work (2001) only 11854 simulated were involved in simulation. The difference of number of the simulated particles may cause the difference in the results. Since more simulated particles were adopted in the current simulation, it is reasonable to believe that the present results are more realistic.

4.2 Supersonic Microchannel Flows with Vacuum Boundary

4.2.1 Effect of the Kn number

Figure 4.3 shows the effect of the Kn on the velocity profiles. The incoming flow enters the microchannel and decelerates during its development through the channel. Figure 4.3 (a) shows the presence of velocity slip in all the cases with different Kn; in

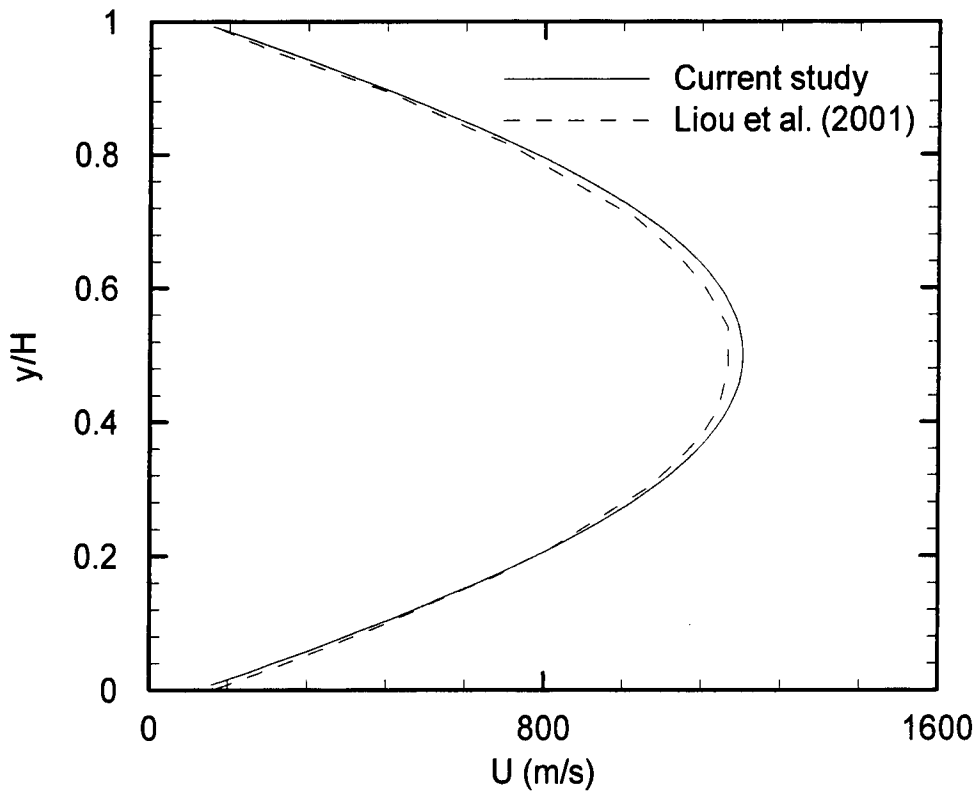

Figure 4.1: Comparison of the streamwise velocity at x/L = 0.5 for vacuum boundary cases.

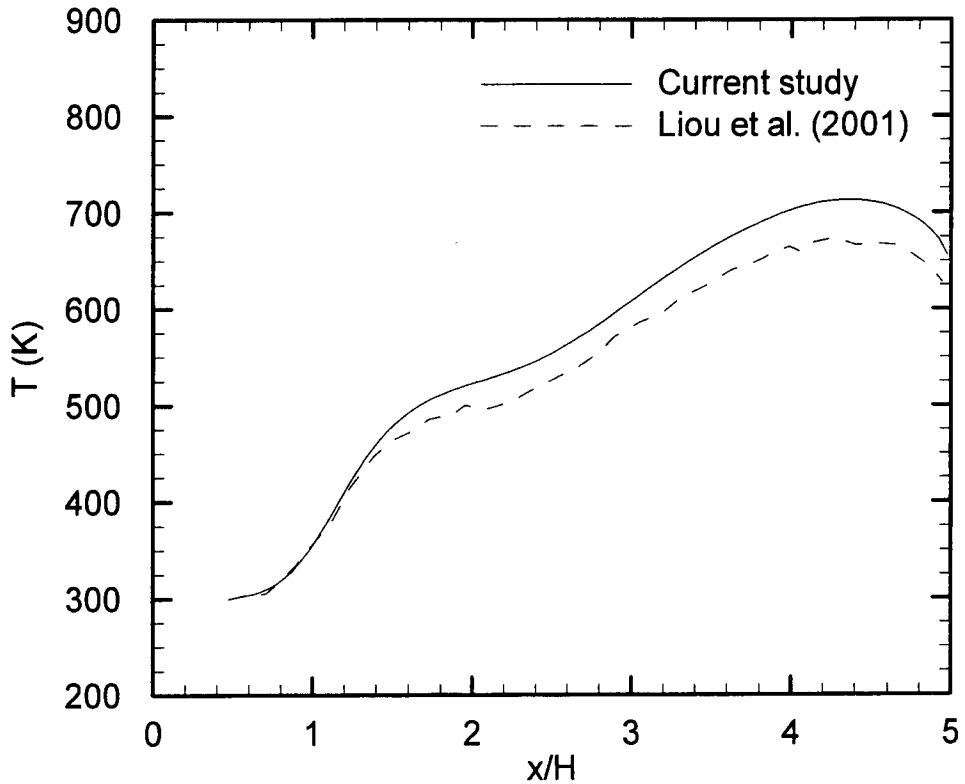

Figure 4.2: Comparison of the centerline temperature distribution for vacuum boundary cases.

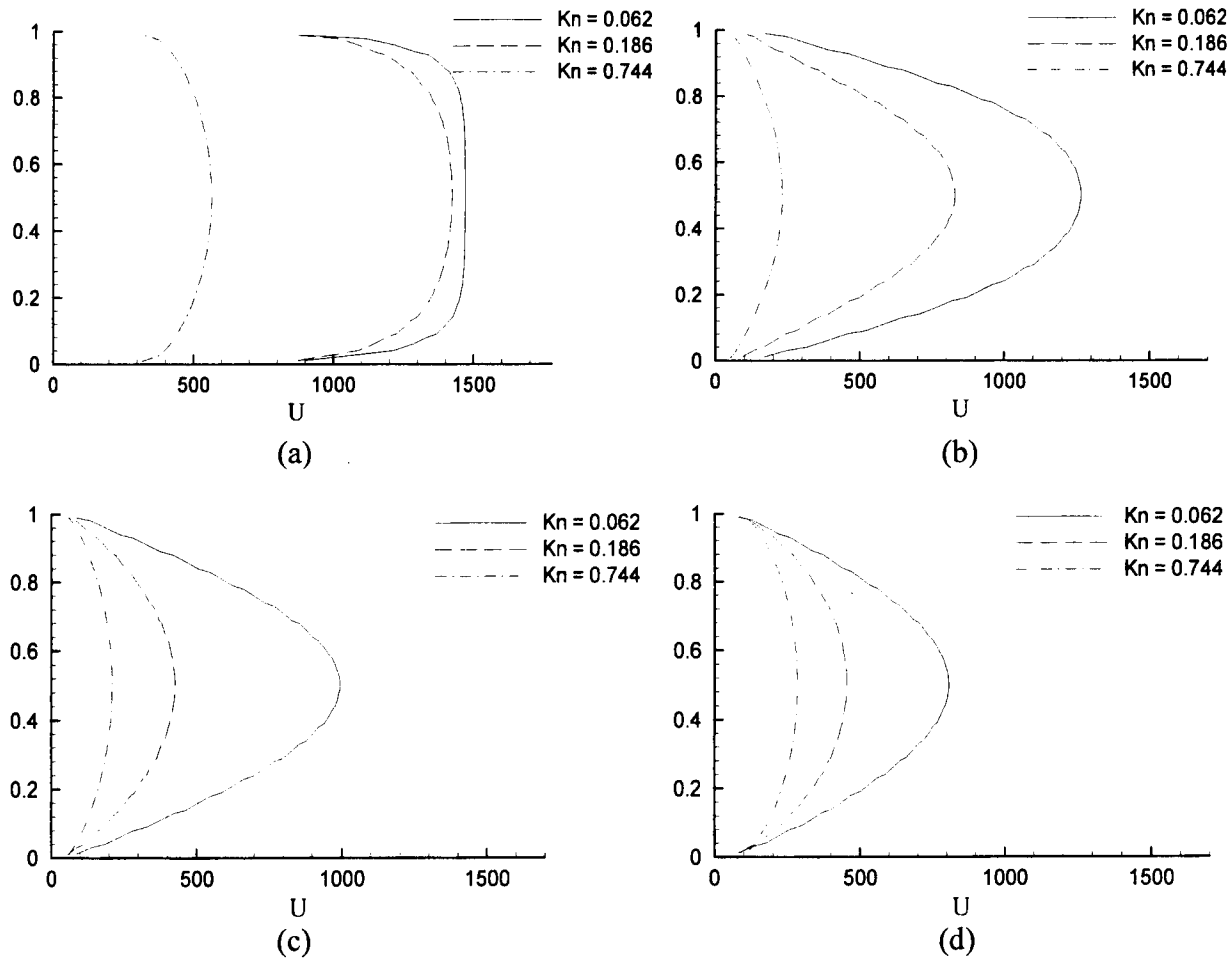

Figure 4.3: Velocity profiles at a) x/L = 0.1, b) x/L = 0.4, c) x/L = 0.7 and d) x/L = 0.9 for different Kn cases.

addition, it can be observed that higher Kn yields smaller velocity slip and vice-versa. As for the velocity profiles, higher Kn yields more uniform distributions. For the curve with Kn = 0.062, the velocity distribution is almost uniform across the channel, except in the wall boundary region where a large velocity gradient occurs. The viscous effects from the channel walls increase its significance along with Kn. Therefore, increasing Kn further retards the flow, generating a more uniformly distributed velocity profile.

Due to the wall friction, the downstream flows (Figure 4.3 (b), (c), (d)) show weakened velocity slips near the wall and an overall velocity downfall through all three cases. As expected, the profiles end up in parabolic shapes. Overall, it can be seen that at any given position along the channel, the mean velocity of a higher Kn case is lower than that of a lower Kn case.

Figure 4.4 shows the development of thermal boundary layers for different Kn numbers. In graph (a), an increase in overall temperature is already observed at the channel entrance. This initial increase in temperature results from the wall friction, which decelerates the gas particles just after the flow channel entrance and converts kinetic energy into internal energy. Figure 4.4 (a) reveals that the flow with the highest Kn (Kn = 0.744) is entirely heated at the entrance by means of a noticeable deceleration in velocity. For the other two cases, the temperatures increase to a high value only near the walls due to friction; especially for the slip flow case (Kn = 0.062), where the main part of the flow remains at the free stream temperature.

In Figures 4.4 (b), (c), and (d) the highest Kn flow undergoes a cooling procedure along the whole channel after being heated initially. Further downstream, the bulk flow temperature decreases and in the mean time, the curve becomes uniform. For the other

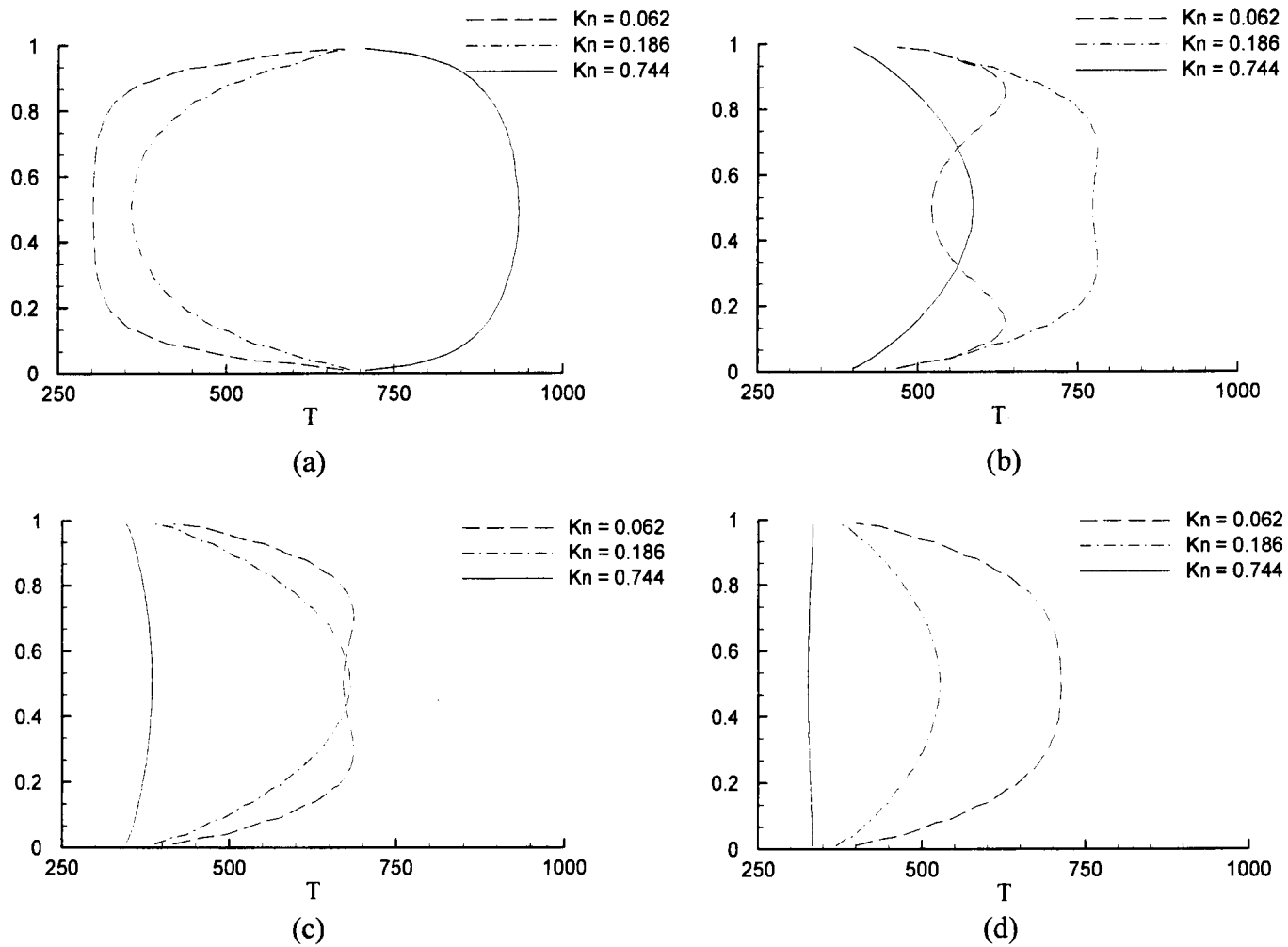

Figure 4.4: Temperature profiles at a) x/L = 0.1, b) x/L = 0.4, c) x/L = 0.7 and d) x/L = 0.9 for different Kn cases.

two cases, the heat generated from the wall friction is gradually transferred to the bulk flow generating two local peaks in the profile. It can be seen that the local peaks merge sooner as Kn increases. Afterwards, there is no longer any heat transfer to the bulk flow and the temperature profiles become uniform near the exit of the channel.

Figure 4.5 shows the temperature distribution along the channel centerline. As mentioned in the previous paragraph, the flow at highest Kn undergoes cooling along the whole channel length, with the heat being transferred from the bulk flow to the walls. Therefore, the centerline temperature for the case with Kn = 0.744 decreases monotonically downstream. For the lower Kn cases, there is a peak, which represents the highest temperature location along the flow stream that moves upstream with increasing Kn.

Figure 4.6 shows the temperature profiles between x/L = 0.4 to x/L = 0.55 of the flow with Kn = 0.186. By taking the location of the maximum centerline temperature on Figure 4.6, the merging phenomenon is observed to occur at the same position at x/L = 0.50 as indicated by Figure 4.4. This position is also where the thermal boundary layers intersect. Further downstream, heat transfer to the bulk flow and cooling subsequently occurs. The peak value of centerline temperature decrease as Kn decreases; therefore, it takes longer for the thermal boundary layers to intersect and to reach the maximum centerline temperature. The heat generated from the wall friction contributes not only to the development of the thermal boundary layers but to the wall heat flux as well. The longer it takes for the thermal layers to intersect, the more heat will be transferred out of the wall. As a result, the value of the maximum centerline temperature decreases.

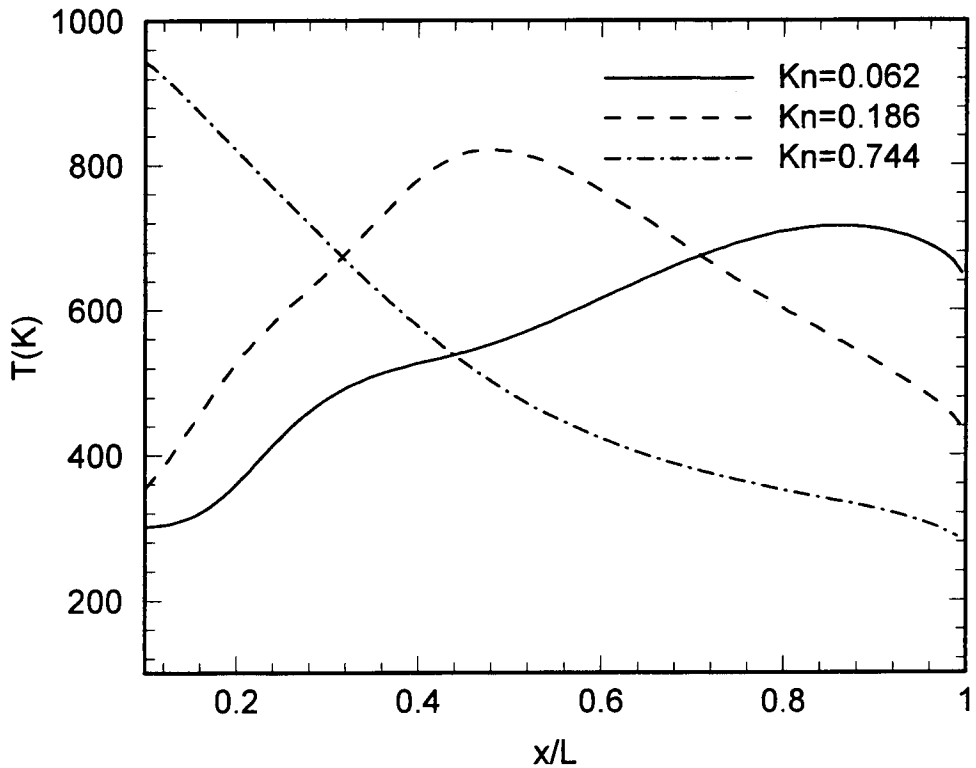

Figure 4.5: Effect of the Kn on the centerline temperature distribution.

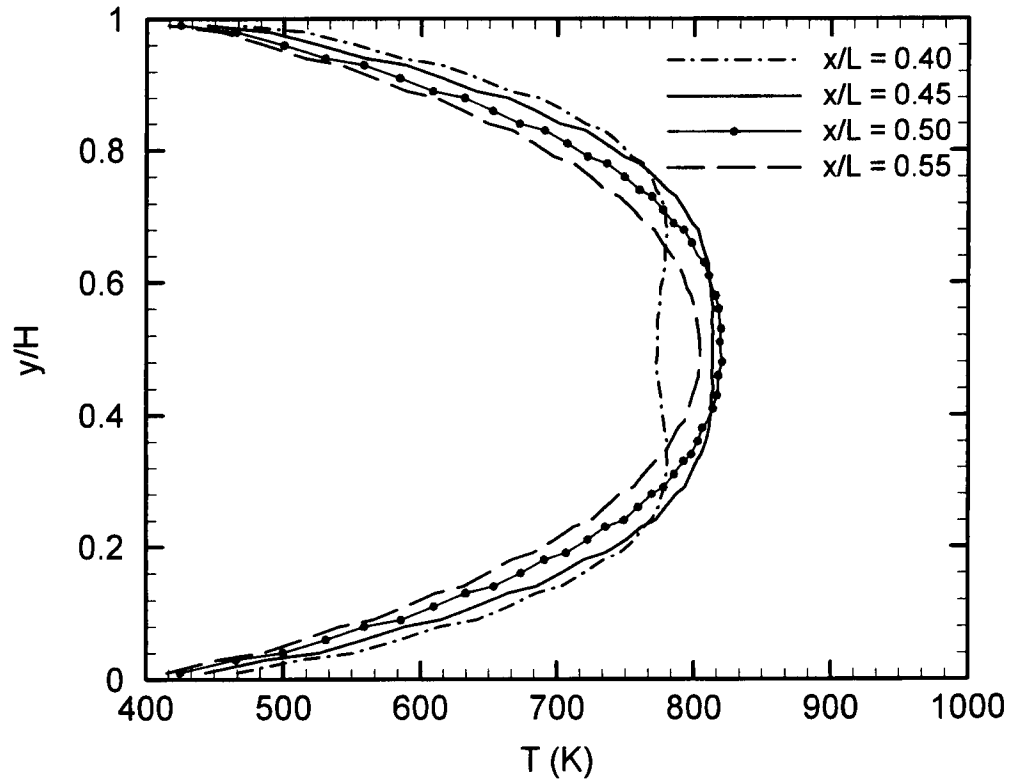

Figure 4.6: Temperature profiles at x/L = 0.40, 0.45, 0.50 and 0.55 for Kn = 0.186.

Figure 4.7 shows the Mach number contours according to the first three cases. For the case with Kn = 0.062, the shock structure is indicated clearly with two detached bow shocks being formed in the wall leading edges. The shocks intersect near x/L = 0.16. The waves obtained from the intersection of the bow shocks, emitted from the upper and lower walls, move downstream, separate, and extend towards the wall as the incident shocks weaken along the channel. As Kn increases to 0.186, the bow shocks broaden with an increase in the angle between the shock and the wall. However, it is hard to identify the intersection of the shocks because of the large shock thickness. The shock structure for Kn = 0.744 behaves dramatically different from the previous cases. Namely, the flow initially decelerates to subsonic due to the enormous viscous effect from the wall, hence so no shock appears in the channel.

Figure 4.8 shows the wall heat flux distribution along the microchannel. The transition flow regime cases have similar trends in the wall heat flux distribution: both reach a maximum peak in their profiles. However, as Kn decreases to 0.062, there is no evident peak occurring in the profile. The drop in the peak value with respect to the Kn maybe due to the fact that the highest Kn flow is entirely heated at the entrance, and so all the heat generated from the wall friction contributes to the wall heat flux. On the other hand, in the other two cases, heat is still required to develop the thermal boundary layers. From the Mach number contours, the positions of the peaks in both cases can be located, with no evident slip change, in the region where Mach number is around 0.4. In addition, for the slip flow case (Kn = 0.062), the heat flux initially decreases and maintains a relatively uniform profile, because more heat has been transferred to the bulk flow in order to develop the thermal layer throughout the whole length of the channel.

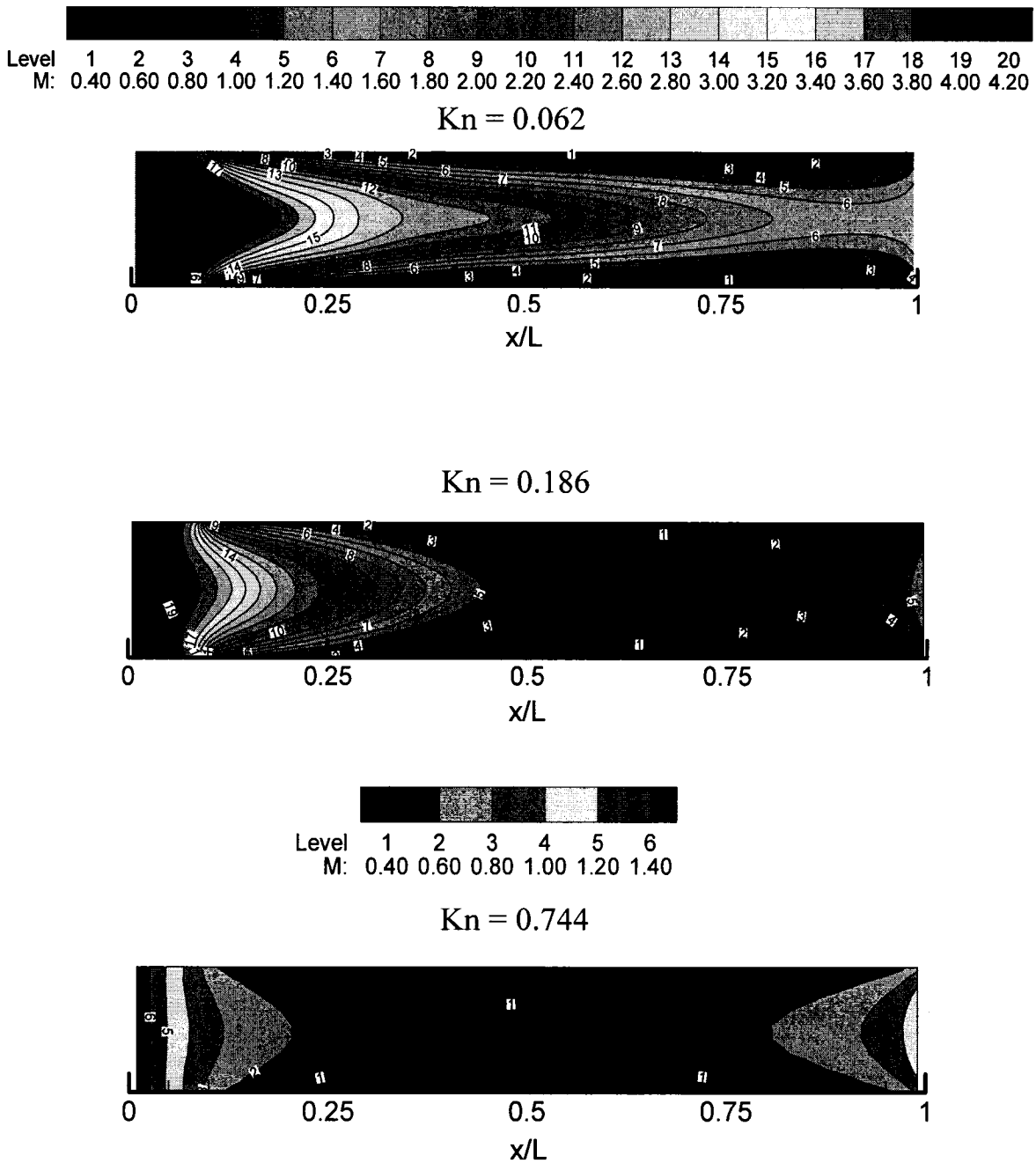

Figure 4.7: Effect of the Kn on the Mach number contours.

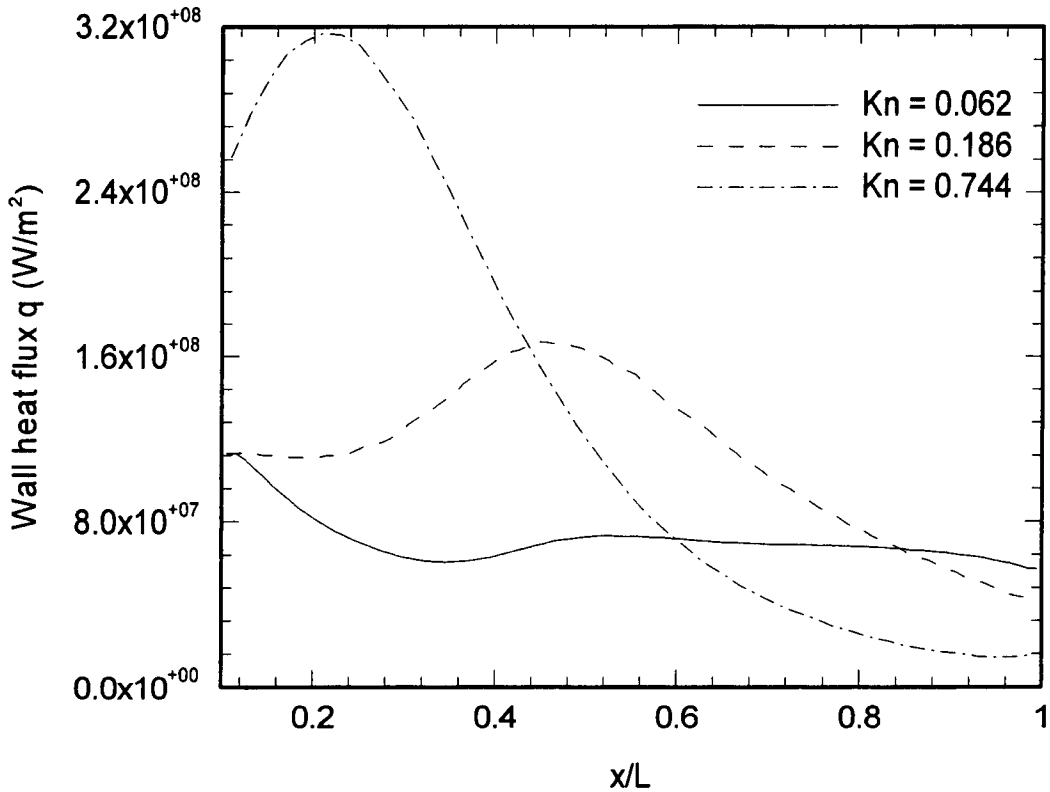

Figure 4.8: The wall heat flux distributions for different Kn.

Thus, it can be concluded that the flow deceleration near the wall and the development of the thermal boundary layers dominate the wall heat flux characteristics.

4.2.2 Effect of wall temperature distribution, flow direction and free stream temperature

In order to examine the wall heat flux characteristics with variable wall temperature distribution, the incoming flow with the temperature of 300 K is allowed to enter from both sides with the first half of the wall maintained at a temperature of 323 K, while the lower half is raised to 353 K. For simplicity, assuming that both flows are from the same inlet but with a reversed temperature distribution, the x-axis is reversed for the flow entering from the higher temperature side. Figures 4.9 (a) and (b) shows that a wall temperature jump is accompanied by a downward step in the wall heat flux, and that a sudden temperature drop causes an upward step in the wall heat flux. The rise in temperature difference due to the decrease in wall temperature causes the wall heat flux to increase, and vice versa. For both cases in Figure 4.9, no significant effect of the flow direction, on the total heat exchange between the bulk flow and the solid walls, can be observed. However, there is a slight distinction in the heat flux profiles. Based on the above analysis, it can be found that a small change in the wall temperature does not influence the total heat exchange behavior of the supersonic microchannel flows.

Figure 4.10 shows the effect of the free stream temperature on the wall heat flux distributions for Kn = 0.062, while the wall temperature is maintained at 323 K. The wall heat flux is higher for Tin = 350 K with a peak slightly shifted upstream. It can be seen that with higher free stream temperature, less energy is required for the thermal layers of the internal flow to be developed. Since the flow at T_{in} = 350K has a higher heat flux

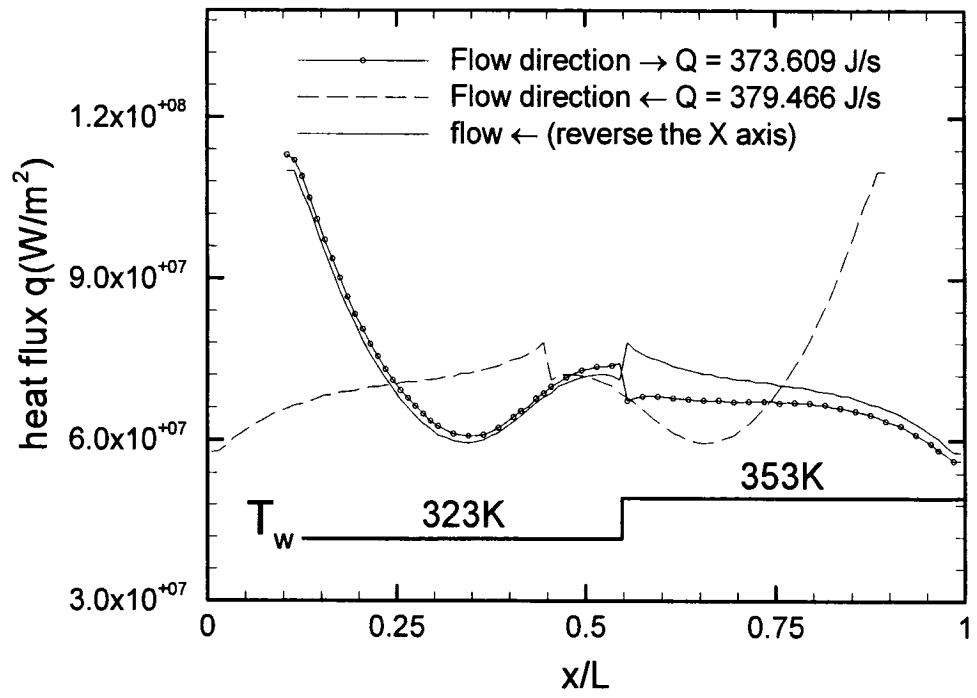

(a)

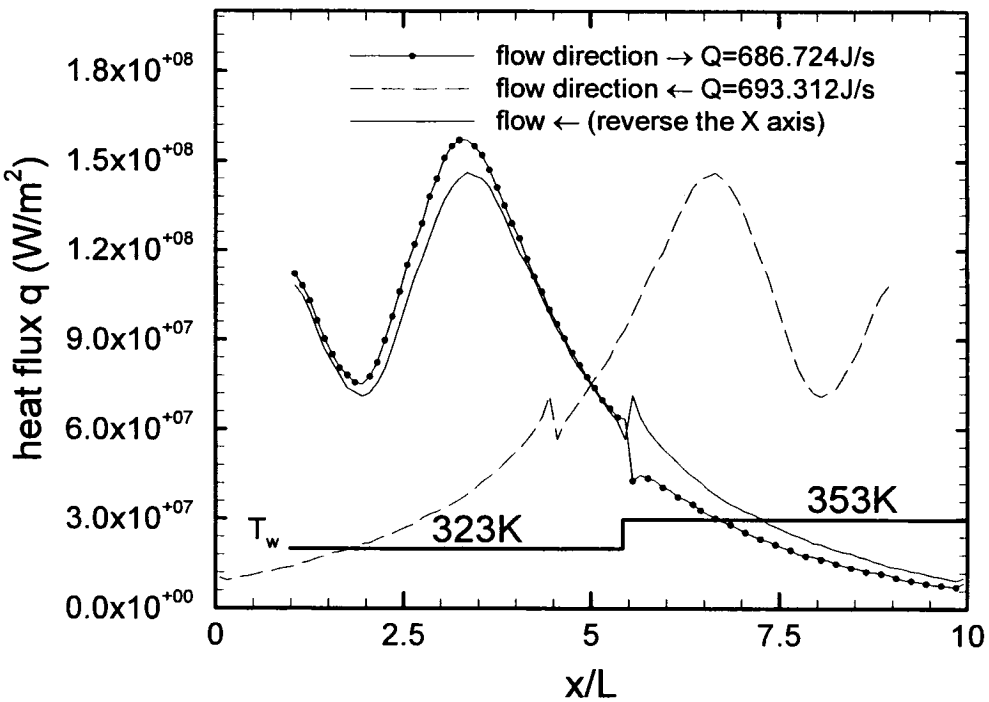

(b)

Figure 4.9: Effect of wall temperature distribution on the wall heat flux for a) L/H = 5 and b) L/H = 10.

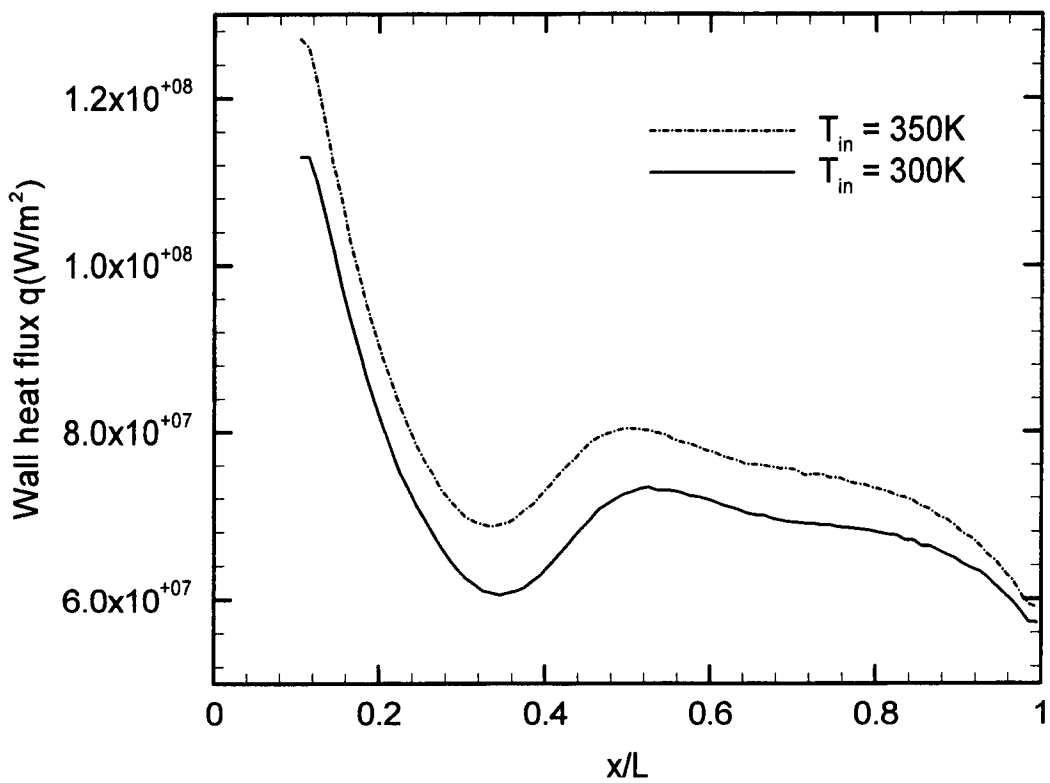

Figure 4.10: Effect of free stream temperature on the wall heat flux.

compared to that at T_{in} = 300 K, the thermal layers develop earlier at T_{in} = 350 K and the profile moves upstream.

4.3 Supersonic Microchannel Flows with Pressure Boundary

4.3.1 Effect of the back pressure

Instead of using the vacuum boundary, the pressure boundary condition was also applied at the channel outlet. The pressure distributions along the channel centerline according to these cases together along with the case using vacuum boundary were plotted in Figure 4.11. At higher back pressures, for instance, P_b = 0.5 or 0.7 MPa, the exit-plane pressure computed from the simulation is equal to the applied back pressure. As the back pressure decreases to 0.1 MPa, however, the exit-plane pressure is found to be higher than the back pressure, which indicates the presence of expansion waves outside the channel. The pressure distribution predicted by the vacuum boundary, which assumes expansion waves outside the channel at the beginning of the simulation, is close with just slight difference to the results for P_b = 0.1 MPa.

Using the pressure boundary, the effect of the back pressure on different flow properties was investigated. In Figure 4.11, it was found that for x/L < 0.6 the back pressure has no effect on the pressure distribution. After this point, the pressure increases monotonically for the two cases with exit-plane pressure equal to the back pressure, while for the case with expansion waves outside the channel, there is a drop in pressure near the channel exit. Figure 4.12 shows the streamwise velocity profiles at x/L = 0.3, 0.5, 0.7 and 0.9 for those four cases. At x/L = 0.3 and 0.5 (below the location of x/L = 0.6), all the velocity profiles are identical and are not affected by the outlet boundary condition, which is consistent to the results observed in the pressure distribution presented above.

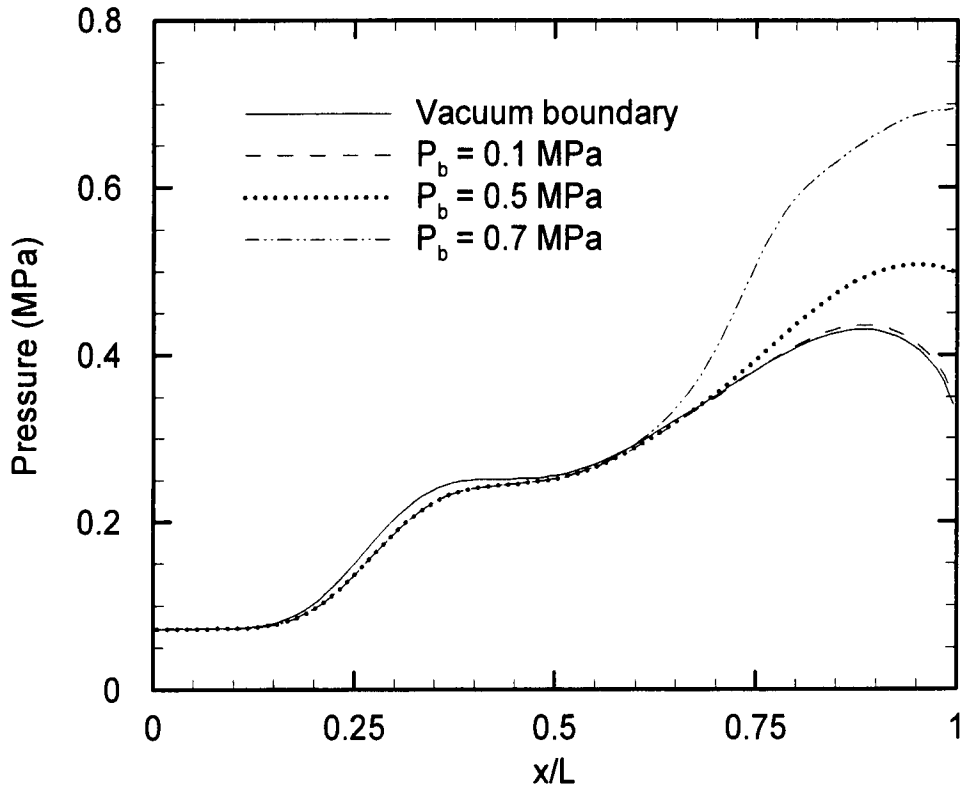

Figure 4.11: Pressure distributions along the channel centerline for different outlet boundaries at $M_{in} = 4.15$.

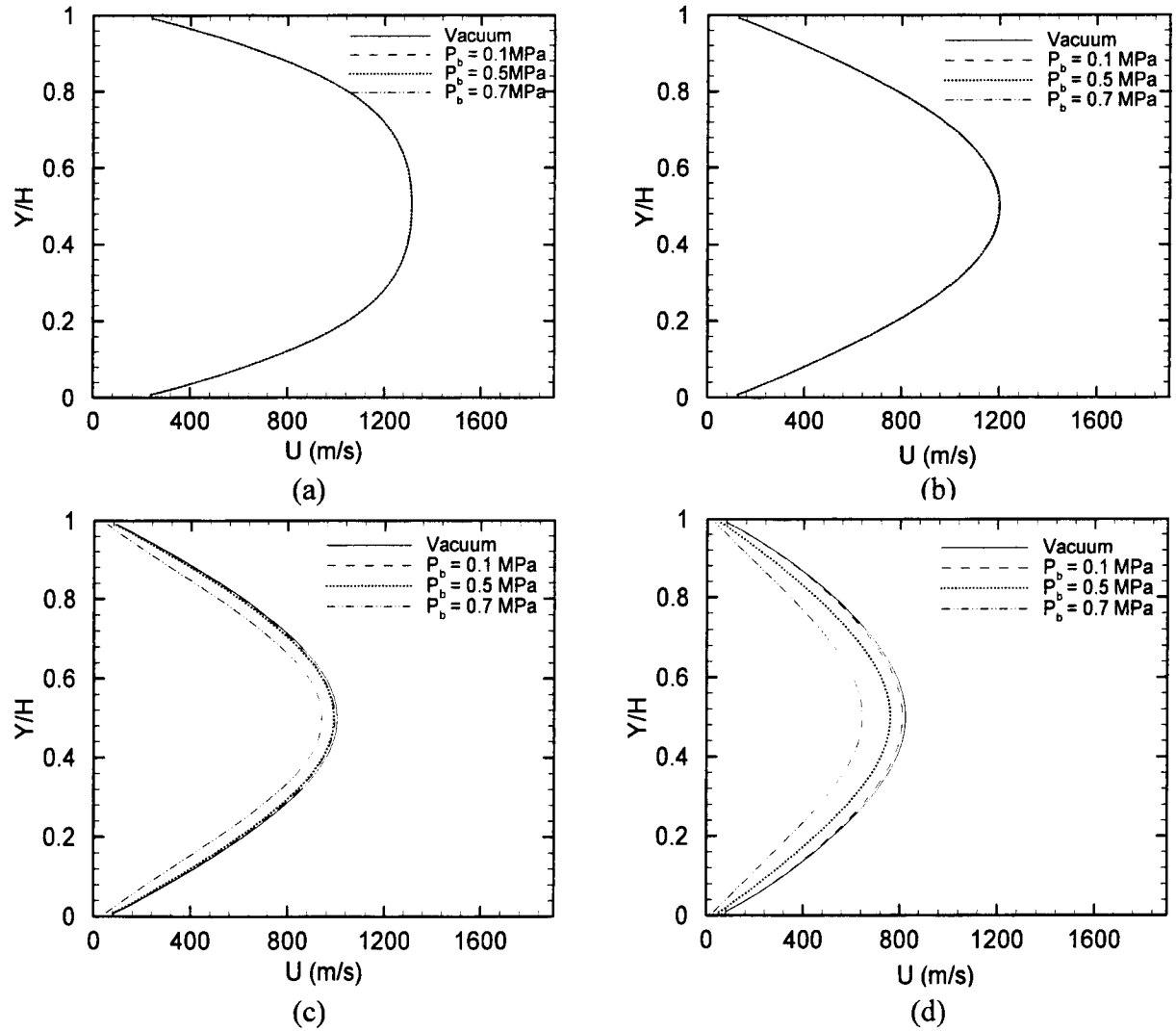

Figure 4.12: Velocity profiles at a) x/L = 0.3, b) x/L = 0.5, c) x/L = 0.7 and d) x/L = 0.9 for different outlet boundaries.

As the flow develops further downstream, the velocity decreases as the back pressure increases and the difference between the velocity profiles becomes more significant. This can be explained by the fact that due to the increase of the back pressure, the flow undergoes more resistance from the outlet boundary, thus generating a lower velocity near the exit.

The heat transfer characteristics with different boundary conditions are shown in Figure 4.13 and Figure 4.14, which give the temperature profiles at various cross sections and the wall heat flux distributions respectively. In Figure 4.13, the development of the thermal layer along the microchannel can be seen where the microchannel flow is heated from the wall to the channel center. Similar to what was observed in the velocity profiles, below the location of x/L = 0.6, there is no effect of the outlet boundary on the flow temperature. Downstream this location, the temperature increases with the increase of back pressure at a given position. This can be explained by the energy conservation theory, where the kinetic energy is converted into the internal energy as the flow decelerates due to the wall friction, thus increasing the flow temperature. Therefore, as x/L > 0.6, the significant decrease of the flow velocity due to increasing back pressure causes the flow temperature to increase. Accordingly, the wall heat flux transferred from the microchannel flow to the upper and the lower boundary walls increases, which is shown in Figure 4.14.

4.3.2 Effect of the inlet Mach number

Effect of the inlet Mach number was investigated by modeling the flow with M_{in} = 3.39 and 4.15 respectively imposing a back pressure of 0.5 MPa, which is higher than the value resulting in expansion waves outside the channel exit. The Mach number contours

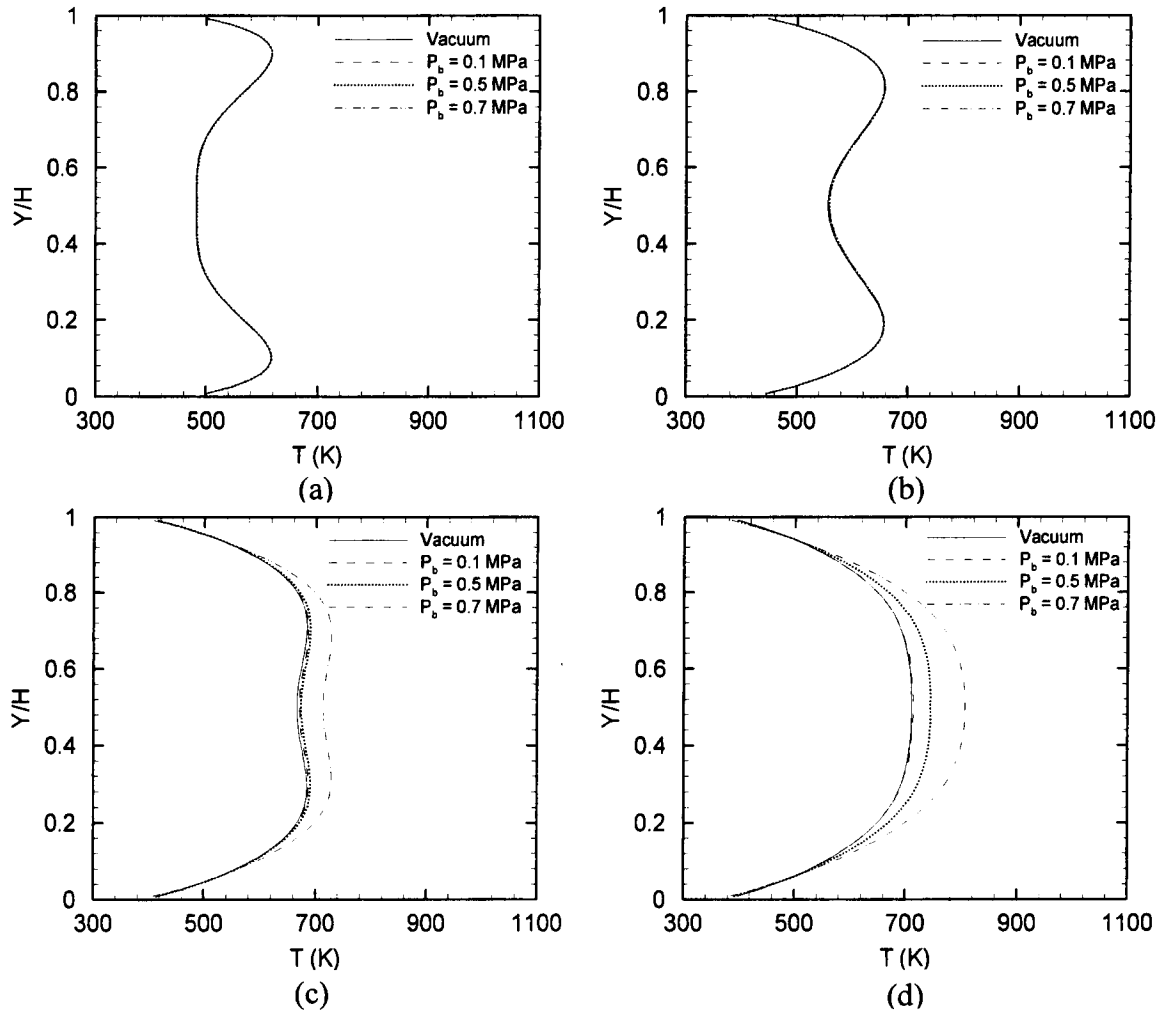

Figure 4.13: Temperature profiles at a) x/L = 0.3, b) x/L = 0.5, c) x/L = 0.7 and d) x/L = 0.9 for different outlet boundaries.

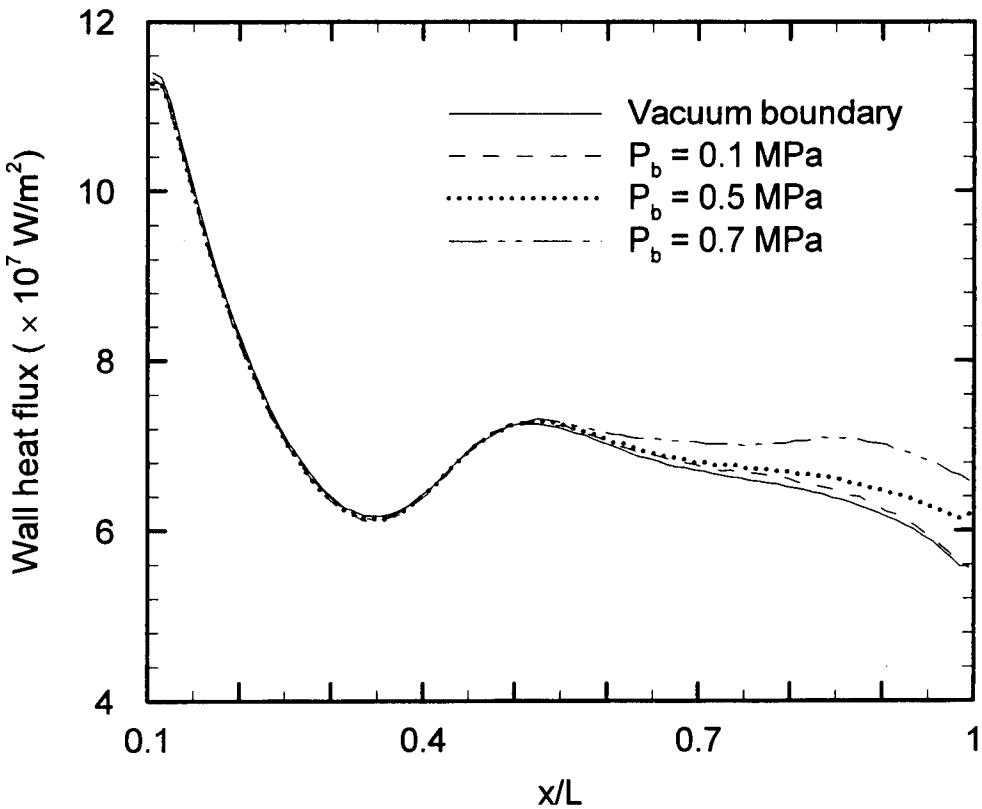

Figure 4.14: Wall heat flux with respect to different outlet boundaries.

were plotted for these two cases in Figure 4.15. Being discharged by the same back pressure, the microchannel flow with $M_{in} = 4.15$ decelerates all the way along the channel until it reaches the exit, whereas the flow with $M_{in} = 3.39$ has a relatively lower speed at certain places and accelerates again throughout the second half of the microchannel.

Significant deviation in the pressure distribution has been revealed in Figure 4.16 between these two cases. Flow with the inlet Mach number of 3.39 has a significant pressure rise starting from the end of the free stream region and ending up with a peak located at around $x/L = 0.7$. This pressure rise is similar to the pressure jump observed in the continuum flow model due to a shock. Near the exit, the pressure eventually decreases gradually along the channel centerline, and at the same time, the flow decelerates to subsonic flow with a Mach number approximately equal to 0.92 just downstream the peak.

In Figure 4.17, the wall heat flux distributions for these two cases are shown. Heat is transferred from the bulk flow to the walls and increasing the inlet Mach number leads to an enhanced wall heat flux. This is due to the fact that the temperature of the high-speed microchannel flow is dominated by the flow speed. As the supersonic flow enters a microchannel, it starts to be retarded by the walls due to the wall friction. As a result, a significant amount of kinetic energy is converted to internal thermal energy thus heating the bulk flow and enhancing the wall heat flux.

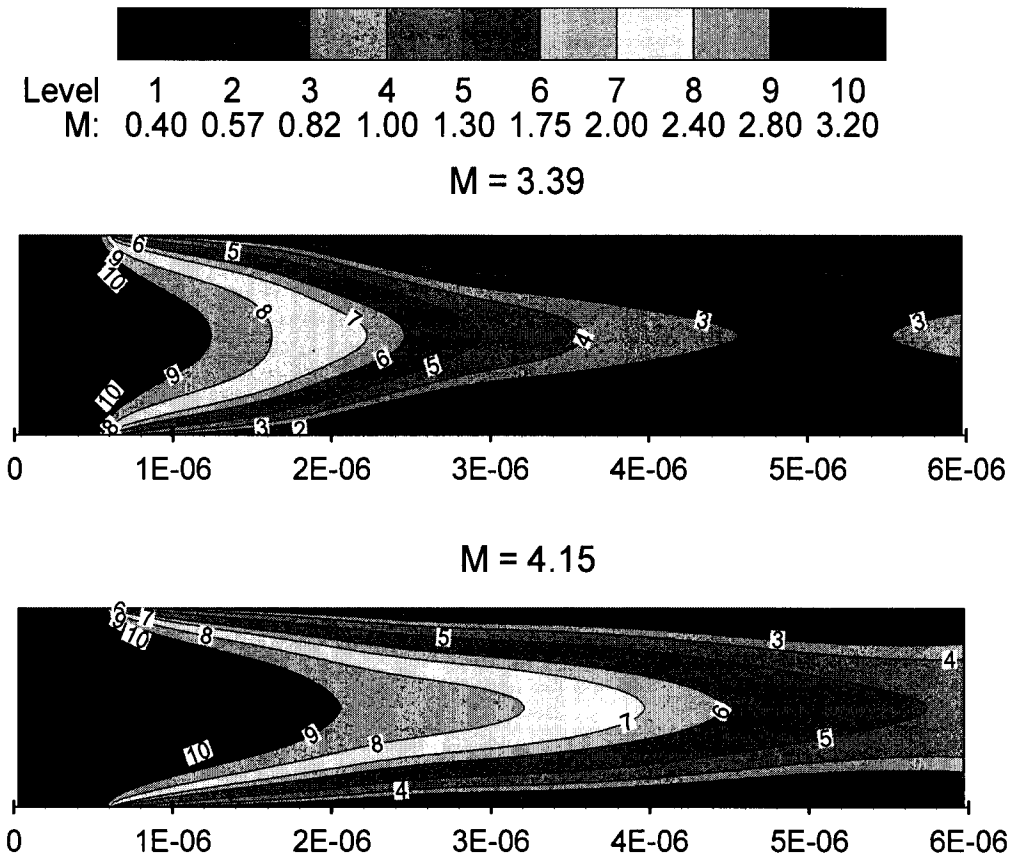

Figure 4.15: Mach number contours for supersonic microchannel flow with $M_{in} = 3.39$ and $M_{in} = 4.15$.

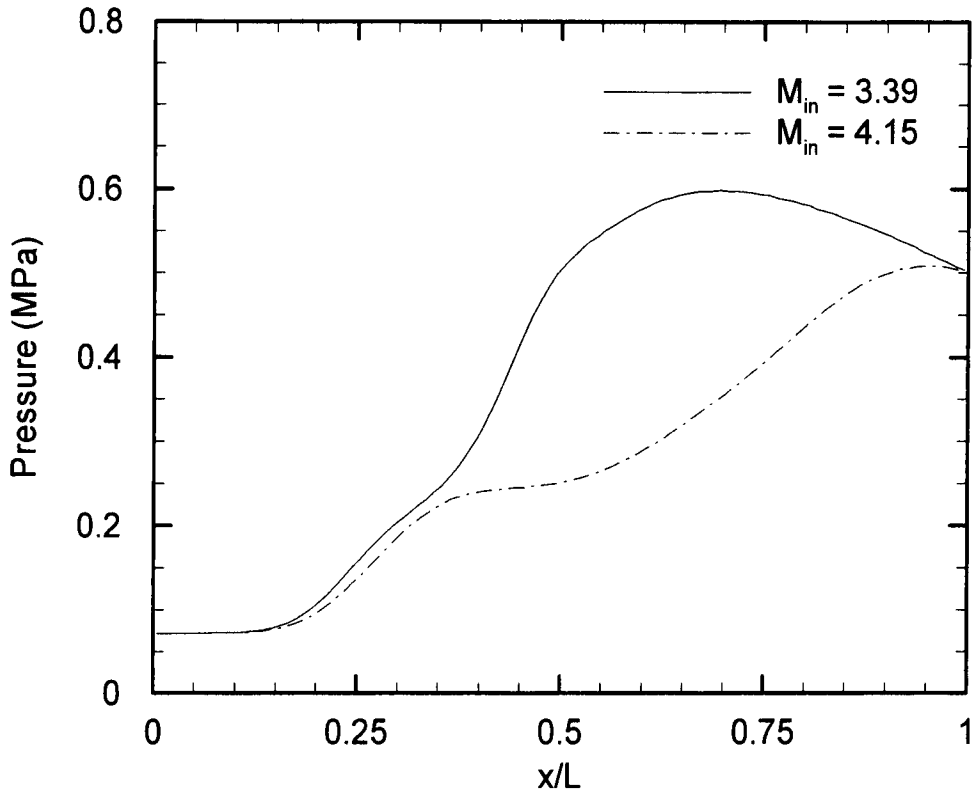

Figure 4.16: Effect of the inlet Mach number on the pressure distribution along the channel centerline at $P_b = 0.5$ MPa.

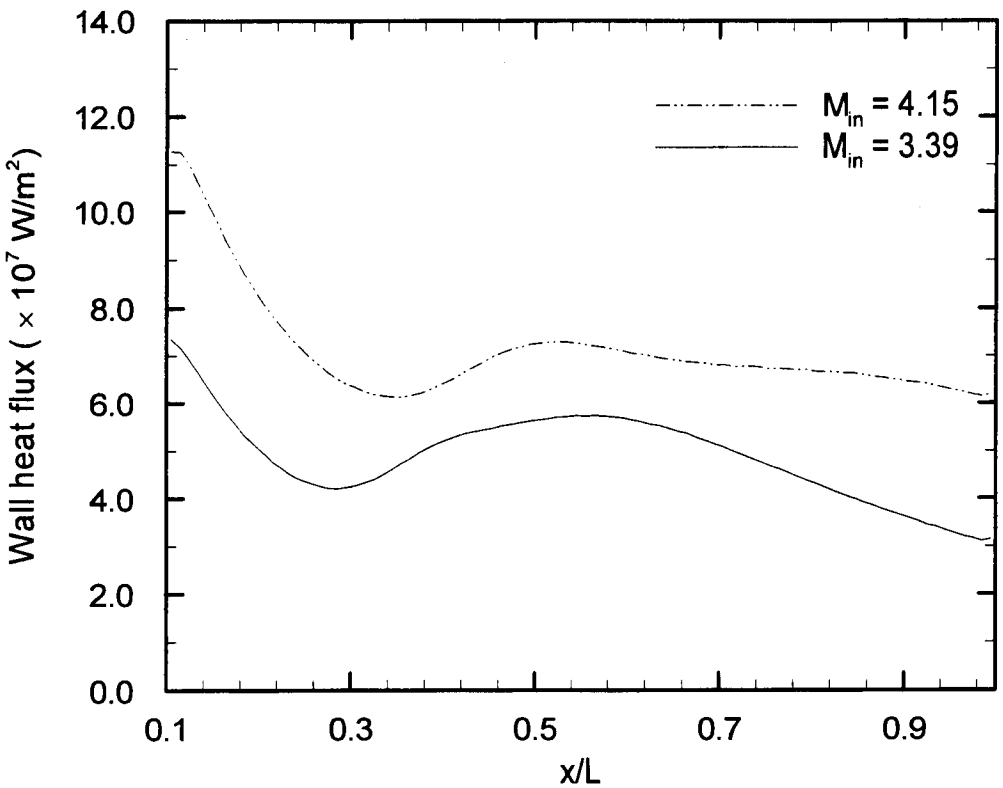

Figure 4.17: Effect of the inlet Mach number on the wall heat flux at P_b = 0.5 MPa.

Table 4.1 Test cases for supersonic flows with vacuum boundary

	Case number							
	1	2	3	4-a	4-b	5-a	5-b	6
Kn (λ/H)	0.062	0.186	0.744	0.062				
L(μm)	6	2	0.5	6		12		6
H(μm)	1.2	0.4	0.1	1.2		1.2		1.2
Mesh	60×100	60×100	10×50	60×100		60×100		60×100
L/H	5			5		10		5
T_{in} (K)	300			300		300		350
T_w (K)	323			323-353	353-323	323-353	353-323	323
Number density(m^{-3})	1.75×10^{25}							
Gas species	nitrogen							
M_{in}	4.15							

Table 4.2 Test cases for supersonic flows with pressure boundary

	Case number				
	1	2	3	4	5
Kn	0.062				
L(μm)	6				
H(μm)	1.2				
L/H	5				
T_{in} (K)	300				
T_w (K)	323				
Number density(m^{-3})	1.75×10^{25}				
Gas species	nitrogen				
M_{in}	4.15				3.39
P_b (MPa)	vacuum	0.1	0.5	0.7	0.5
Expansion waves present at exit	yes	yes	no	no	no

Chapter 5

Subsonic Flow in Uniform, Series and Parallel Microchannels and Gas Mixing in T-shape Microchannel

5.1 Code Verification

The DSMC code used in the current work was first verified by comparing the numerical predictions with analytical solutions. Figure 5.1 shows a good agreement between the DSMC results and the analytic solutions in the pressure distribution. Moreover, Figure 5.2 depicts the comparison of the normalized velocity profiles obtained from the DSMC modeling and the analytical solver by Beskok (1996). When the local Kn is equal to 0.0583, corresponding to the flow in the slip regime, the three curves agreed well with each other with a maximum deviation of less than 8%. As the flow goes into the transition regime for Kn = 0.592, the first-order approximation can no longer predict the flow accurately with an unexpected higher velocity slip occurring near the wall, while the second-order solution can still work properly. One can find that the DSMC is able to predict the flow not only in the slip regime but also in the transition regime successfully.

5.2 Uniform Microchannel Flow

In order to investigate the Kn effect on the heat transfer characteristics for subsonic microchannel flows, the wall temperature was set as 500 K for the base case, case 2, case 4 and case 5 respectively (Table 5.1). The free steam gas temperature was fixed at 300 K. Figure 5.3 shows that for all the three cases, most of the wall heat flux occurs at the channel entrance region within 25% of the entire channel from the inlet. The magnitude

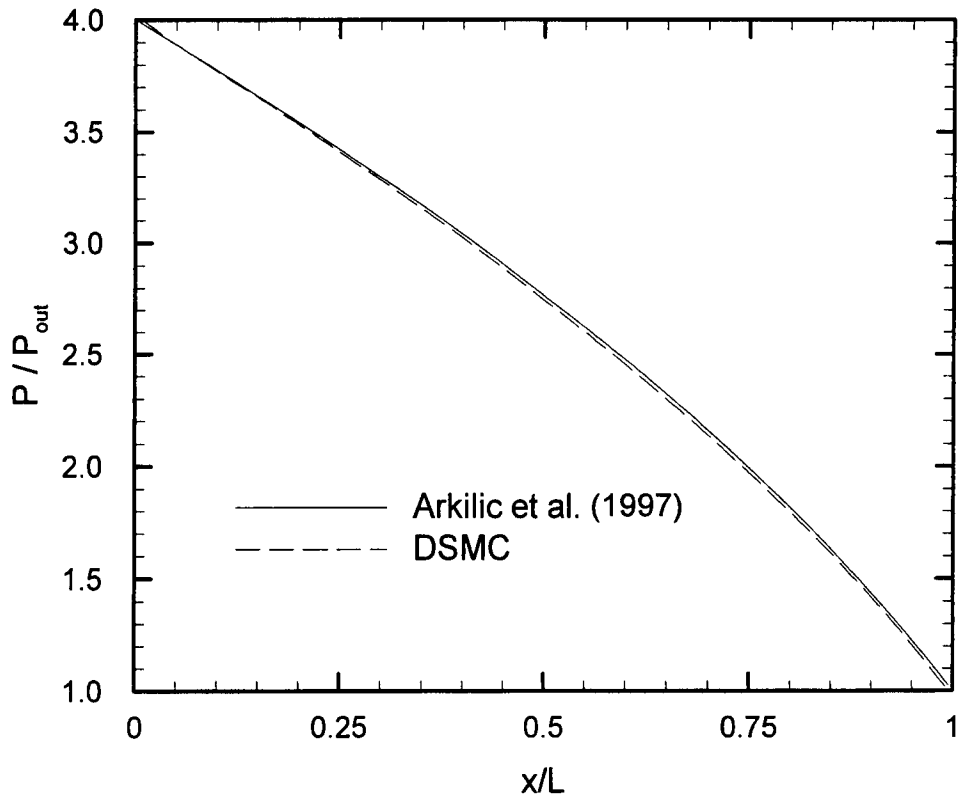

Figure 5.1: Pressure distribution along the uniform microchannel for $Kn_{in} = 0.0547$ and $P_{in}/P_{out} = 4$.

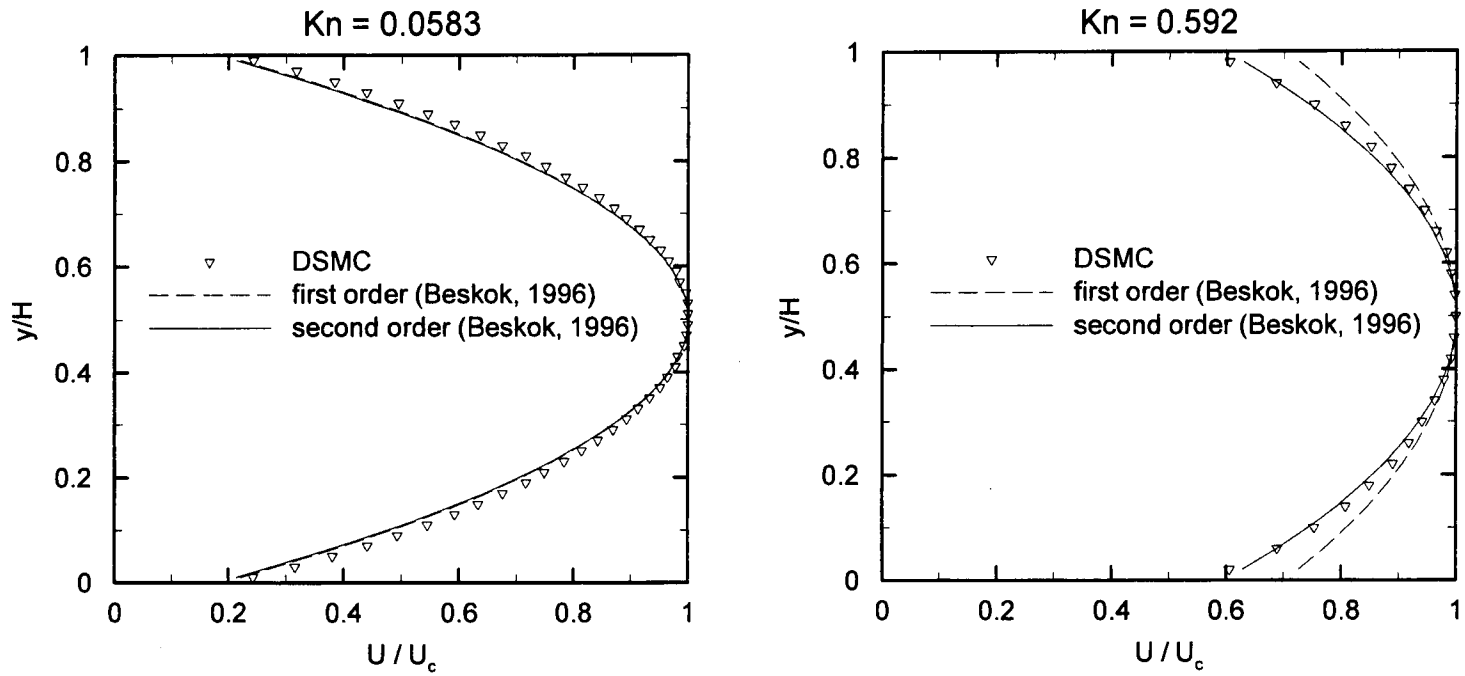

Figure 5.2: Velocity profiles corresponding to different local Knudsen numbers in uniform microchannel.

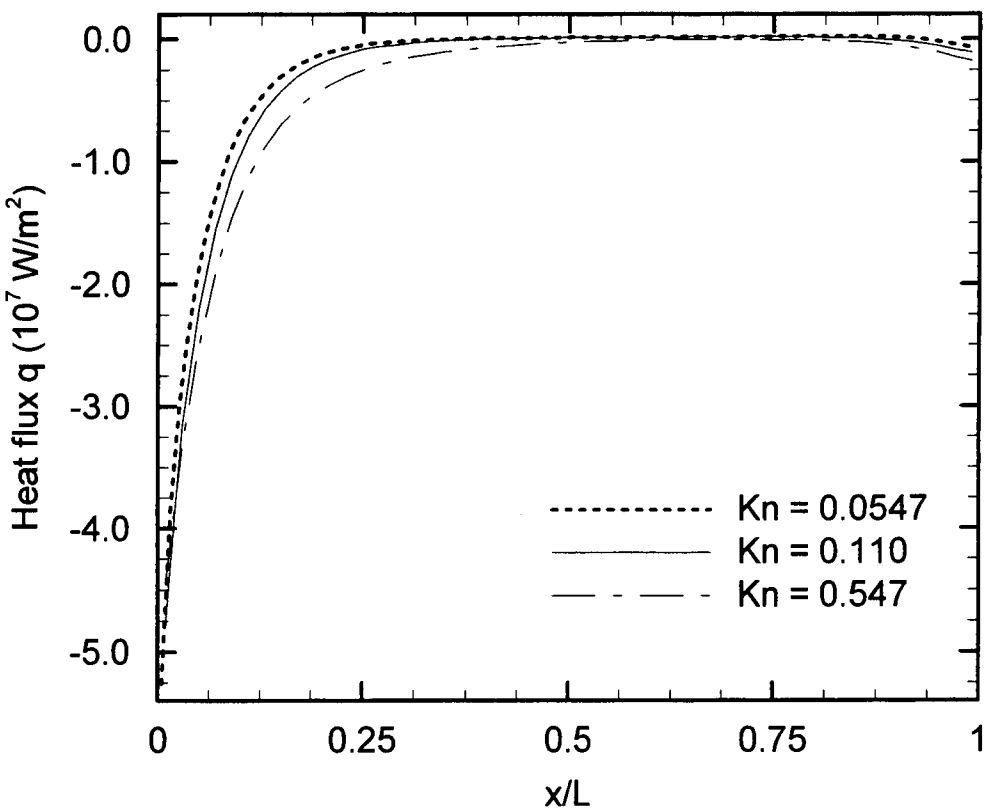

Figure 5.3: The wall heat flux distribution for flow in uniform microchannels with Tw = 500K.

of the wall heat flux in the higher Kn case is slightly greater than that in lower Kn cases. Here, the negative sign indicates that the heat transfer direction is from the hot wall to the bulk flow. This may be caused by the higher wall temperature jump occurring in the more rarefied case as shown in Figure 5.4.

In order to examine the pressure effect on the flow behavior, the pressure ratios 1.33, 2 and 4 were obtained by fixing the inlet pressure at 2.0×10^5 Pa, while the outlet pressure varied from 0.5×10^5 Pa to 1.5×10^5 Pa. Figure 5.5 shows that when $P_{in}/P_{out} = 2$ or 4, the local Kn increases from below 0.1 to above 0.1, which indicates that it is possible to have flow in mixed Kn-regimes. Hence, DSMC is a valid tool to predict this type of flow. The effect of the pressure ratio on the flow velocity is shown in Figure 5.6. The flow velocity increases along the channel, and at a given position, the Mach number is larger with higher pressure ratio. In addition, the Mach number increases more rapidly in a higher pressure ratio case than that in lower pressure ratio cases, especially in the lower half of the channel. By imposing a higher pressure ratio, the compressibility of the gas flow becomes more significant as it develops along the microchannel, which caused a rapid decrease in the flow density. Therefore, in order to satisfy mass conservation, the flow has to accelerate even more. The pressure ratio has almost no effect on the wall heat flux (not shown here), since most of the heat transfer occurs at the first quarter length of the channel, where the pressure ratio has only slight effects on the flow.

Figure 5.7 shows the effect of the wall temperature distribution on the wall heat flux while Figure 5.8 shows the resulting flow temperature distributions close to the walls. In the present work, a linear wall temperature distribution between 400 K and 500 K was applied to the base case 2. Figure 5.7 shows that when the flow enters from the cold side,

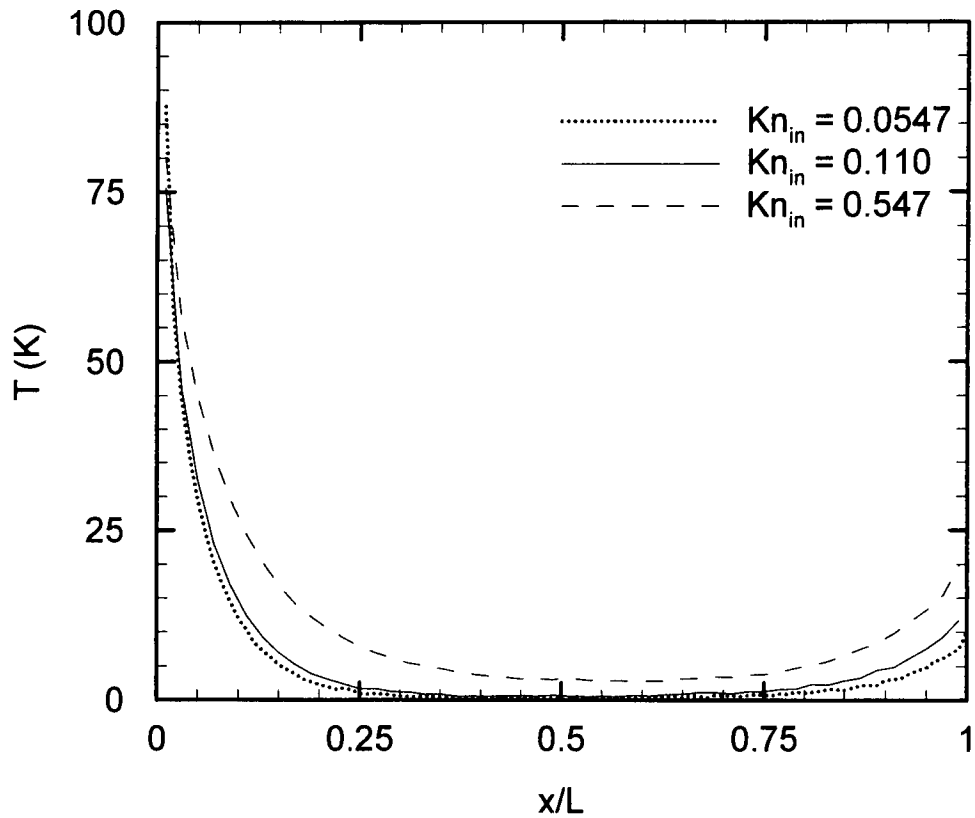

Figure 5.4: The wall temperature jump for flow in uniform microchannels.

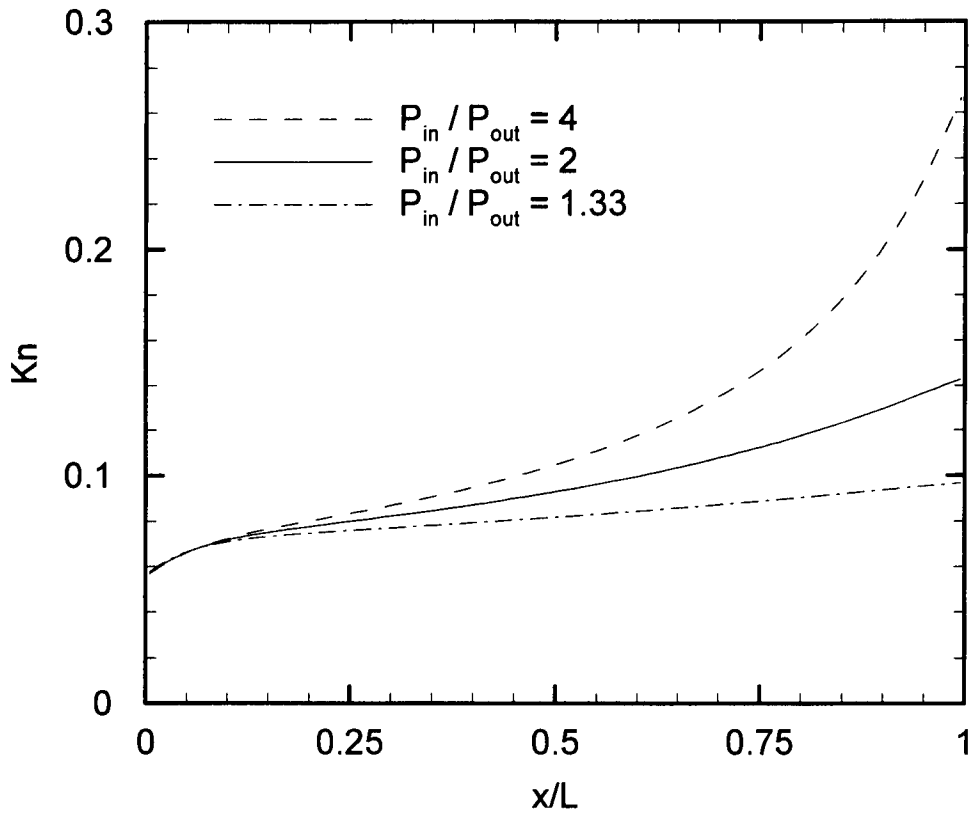

Figure 5.5: Kn number distribution along the uniform channel for $P_{in} / P_{out} = 4$, 2 and 1.33.

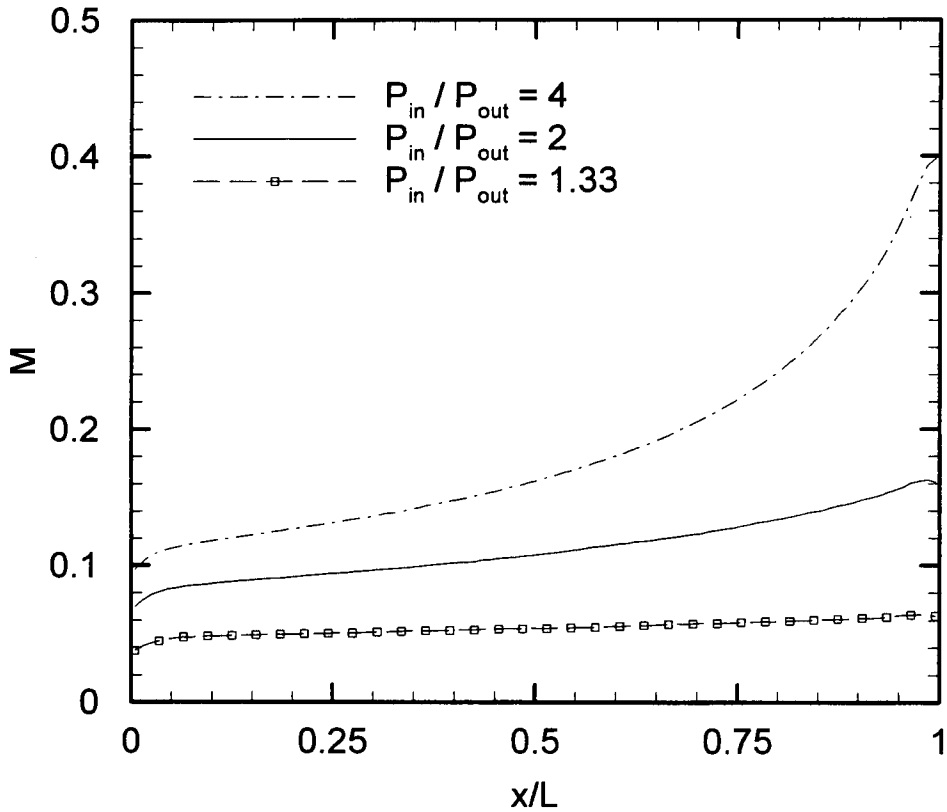

Figure 5.6: Mach number distribution along the centerline of the uniform microchannel.

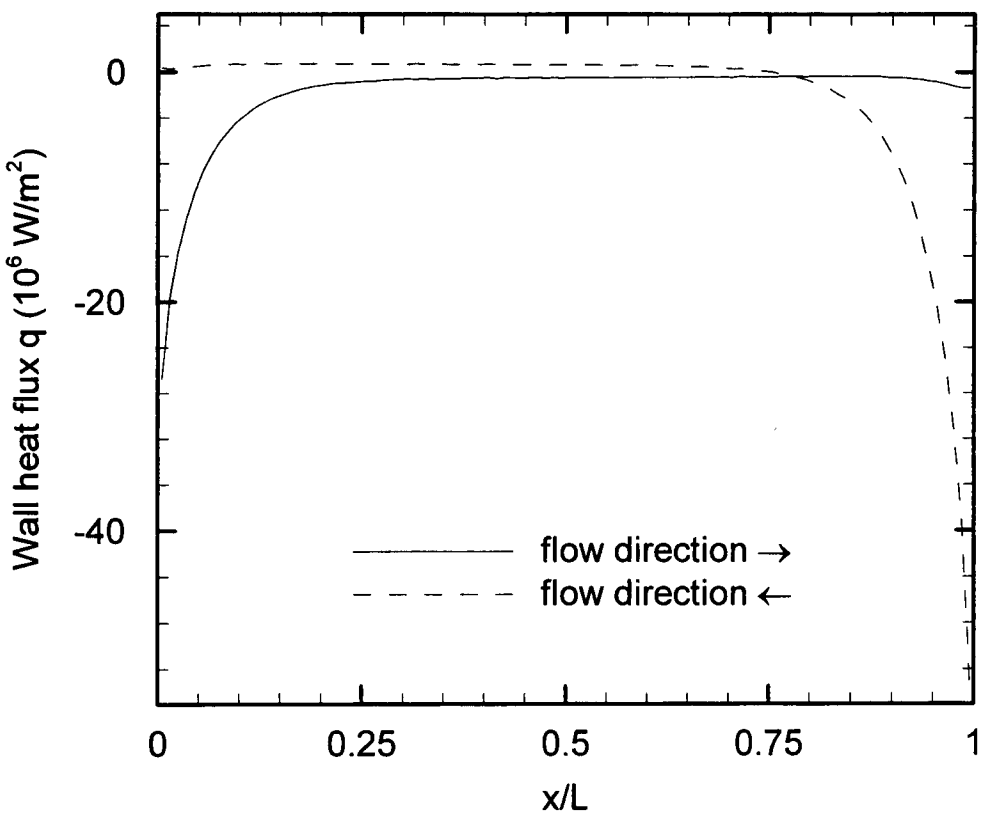

Figure 5.7: Wall heat flux for cases with linear wall temperature distribution.

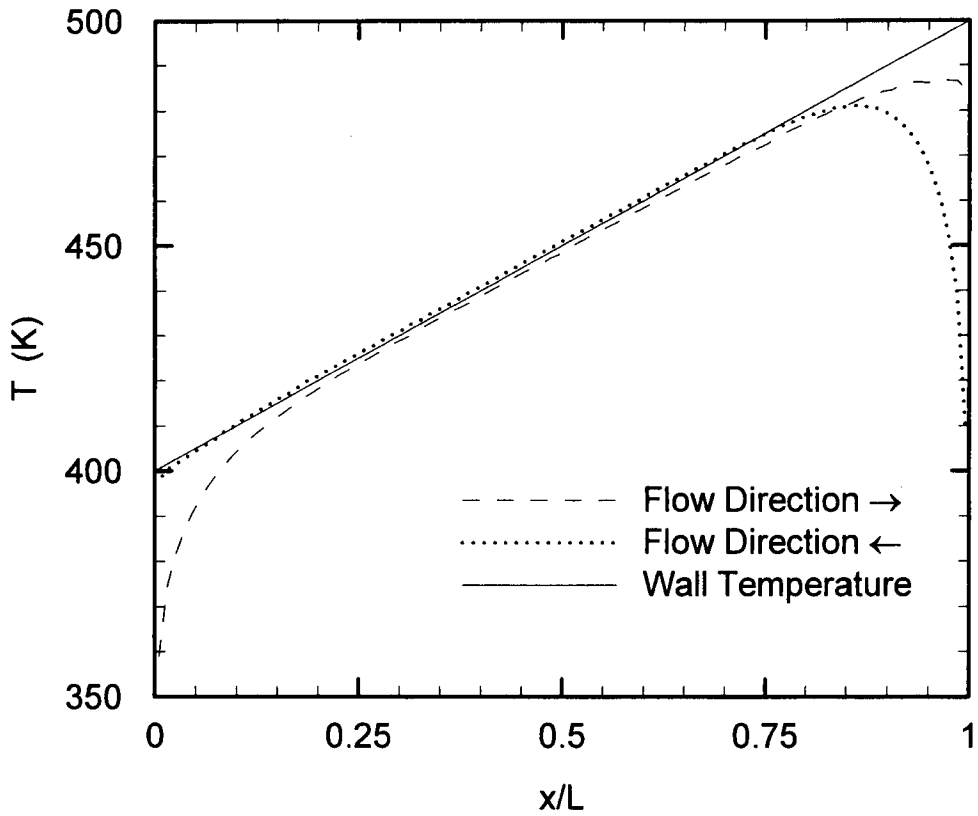

Figure5.8: Temperature distribution of the flow close to the wall.

where T_w = 400 K, most of the wall heat flux occurs at the entrance region and maintains a slightly negative value along the rest of the channel. When the flow enters from the hot side, where T_w = 500 K, most of the wall heat flux also occurs at the entrance region; however, along the rest of the channel it remains a slightly positive value, indicating that the heat is transferred from the bulk flow to the walls. This phenomenon can be explained by the wall temperature distribution depicted in Figure 5.8. For the first case, once the flow becomes mostly heated within the entrance region, the flow temperature is then always slightly lower than the wall temperature since the wall temperature keeps increasing. However, for the other case, as the flow becomes entirely heated within the entrance region, the wall temperature decreases along the channel, and as a result, the flow temperature is always slightly higher than the wall.

5.3 Series Microchannel Flows

Figure 5.9 shows the velocity vectors for case 10 with a pressure ratio of 4. As expected, the streamwise velocity profiles at each cross section are parabolic, except for those close to the interface between the two channel segments. The Kn for this case varies from 0.0957 to 0.230. Hence, apparent velocity slip can be observed near the wall with a magnitude of about 20 m/s at the inlet and 60 m/s at the outlet. In Figure 5.10, the dashed line represents the pressure distribution of the flow entering from the narrow edge while the solid line refers to the flow entering from the wide edge. As the gas stream develops through the narrow segment, the collision rate between the molecules and the wall increases and enhances the wall friction. As a result, larger pressure drop can be always found within the narrow segment.

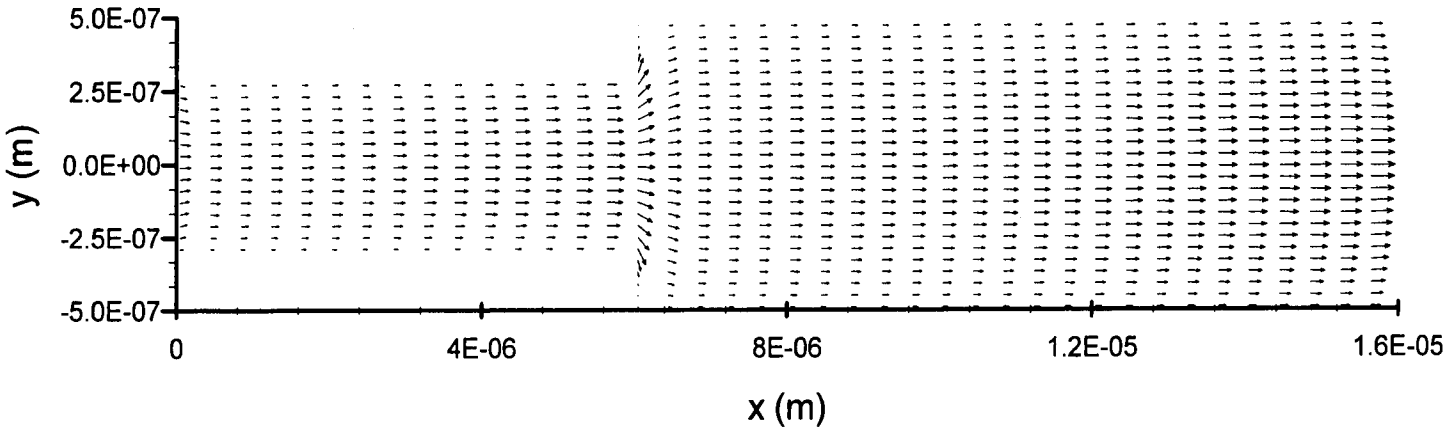

Figure 5.9: Velocity vectors for series microchannel flow at $P_{in}/P_{out} = 4$ and $Kn_{in} = 0.0912$.

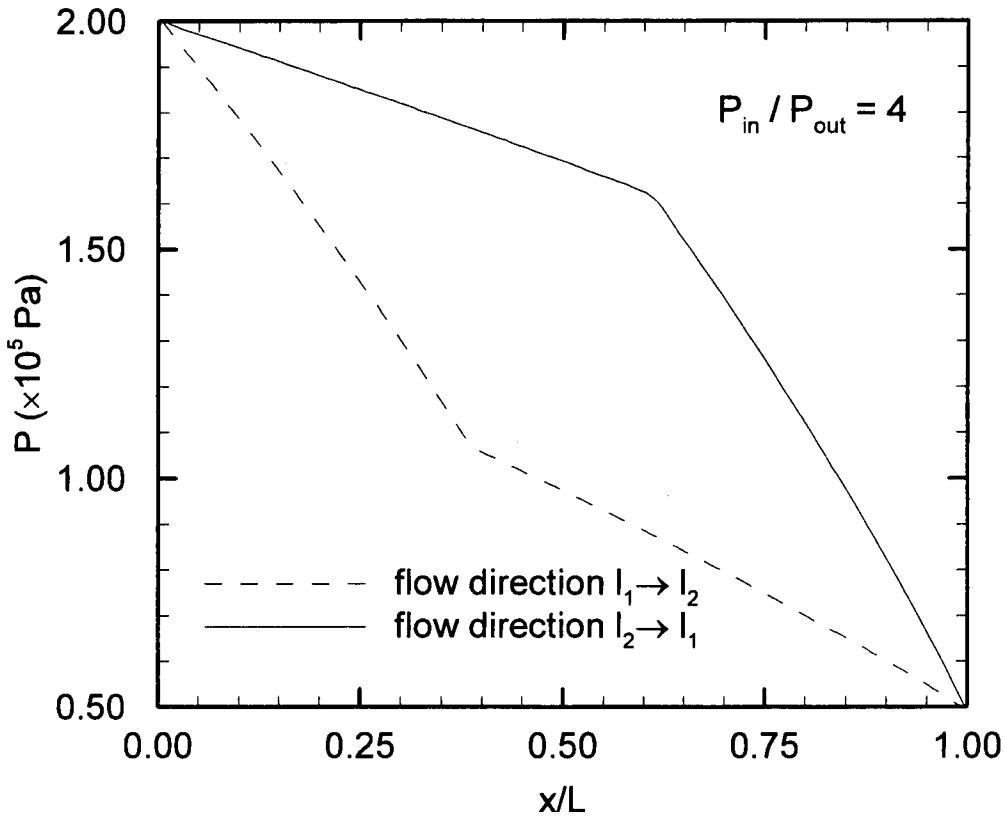

Figure 5.10: Pressure distribution of the series microchannel flow coming from difference edges at $P_{in}/P_{out} = 4$.

The heat transfer characteristic is investigated by setting the wall temperatures higher than the incoming free stream flow temperature. For the first case, T_{w1} (the narrow section wall temperature) and T_{w2} (the wide section wall temperature) are kept at 400 K and 600 K respectively. For the second case, the wall temperature settings are reversed. Figure 5.11 shows that most of the wall heat flux occurs at the beginning of each section, thus warming or cooling the flow almost immediately upon entering the channel segments depending on the temperature difference. These results are consistent to those observed from the uniform channel cases. Unlike the uniform channel cases, a wall heat flux jump can be observed right before the interface for the first case, while a wall heat flux drop occurs in the same position for the second case.

The interface of the two channel segments is located at x/L = 0.375, and so Figure 5.12 (a) and (b) refer to the temperature profiles before the interface while Figure 5.12 (c) and (d) identify the temperature profiles after. For both cases, the flow temperature increases to the wall temperature at x/L = 0.25 as shown in Figure 5.12 (a). However, in Figure 5.12 (b), it is interesting to find that at x/L = 0.36 the flow temperature increases and becomes even higher than the local wall temperature for the first case. For the second case, the flow temperature starts decreasing. This may be due to the diffusion effect of the rarefied flow, which allows the upstream flow to be warmed up or cooled down by the downstream flow near the interface. In the first case, the upstream flow from the interface is heated by the warmer downstream flow, which increases the flow temperature higher than the wall temperature. As a result, heat is transferred from the flow to the wall, which causes the wall heat flux jump as mentioned. In the second case, the flow in a

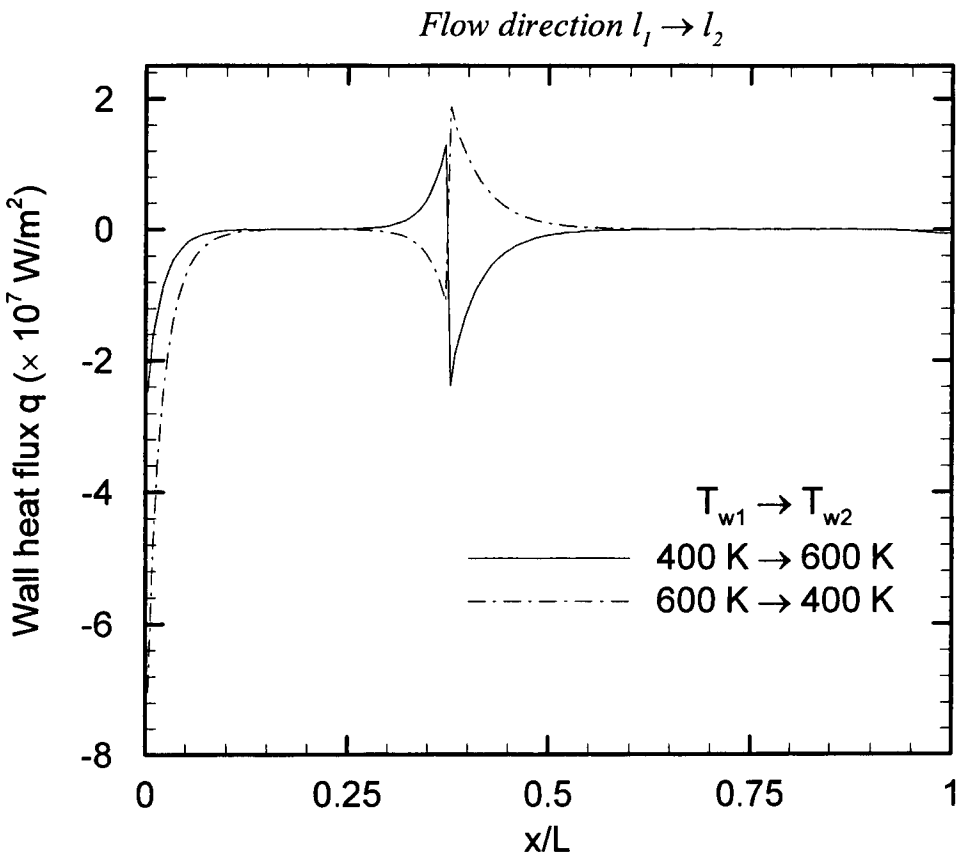

Figure 5.11: Wall heat flux for the series microchannel flows with different wall temperature distributions.

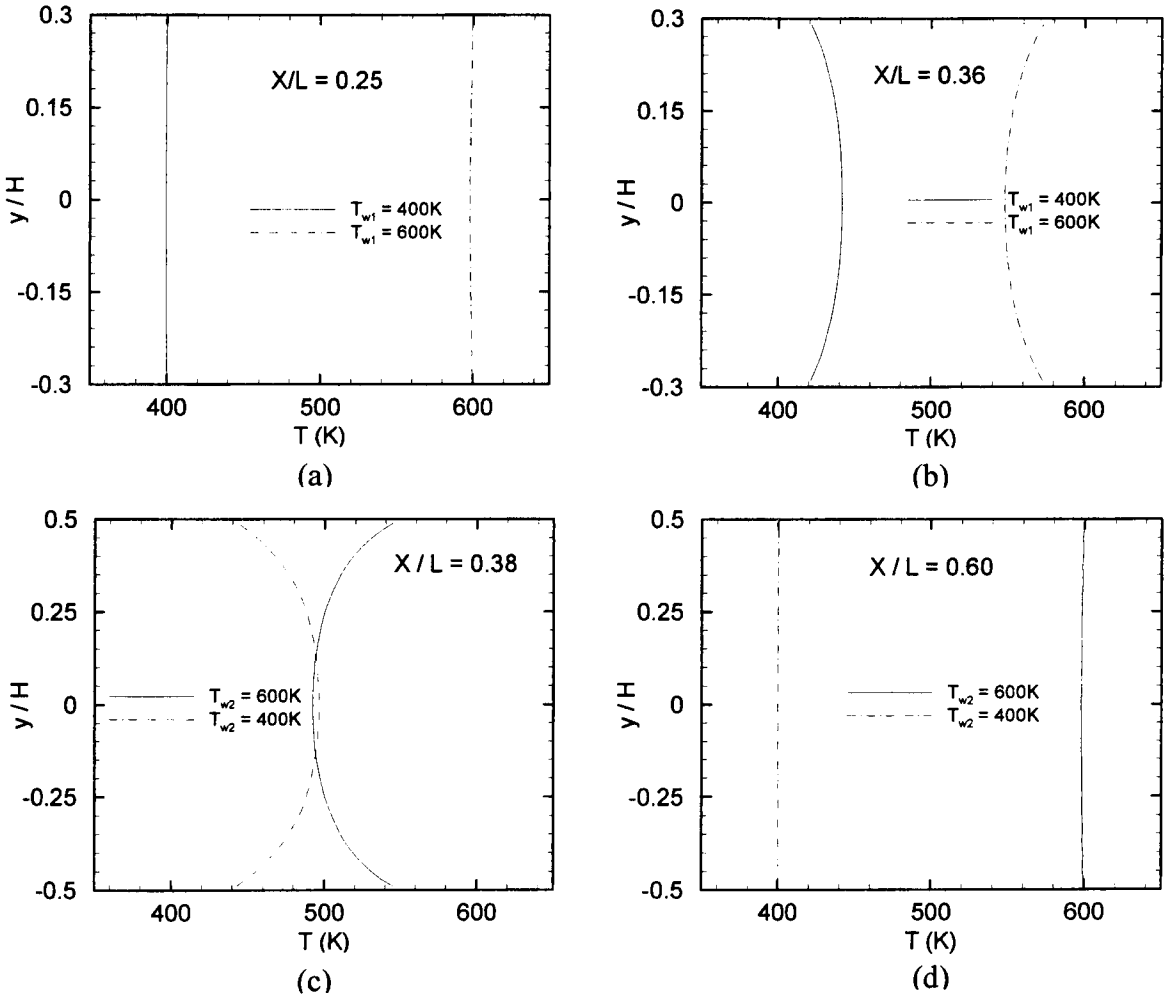

Figure 5.12: Temperature profiles at (a) x/L = 0.25, (b) x/L = 0.36, (c) x/L = 0.38 and (d) x/L = 0.60.

small region upstream from the interface, which is already cooled by the downstream flow, needs to gain more heat from the wall and hence a heat drop occurs.

Case 11 (Table 5.2) was conducted to investigate the effect of the gas species. Here, the flow of argon gas was simulated. The velocity profiles in Figure 5.13 (a)-(d) show that at x/L = 0.431, the speed of the helium gas flow is greater than that of the argon flow, with the velocity difference increasing as the pressure ratio increases. The molecular mass of argon is 6.63×10^{-26} kg, almost ten times of the molecular mass of helium (6.65×10^{-27} kg). The lighter gas is more sensitive to pressure drop throughout the channel and gains more acceleration as the pressure drop increases, yielding the higher difference in velocity.

5.4 Parallel Microchannel Flows

The velocity vectors are presented in Figure 5.14, which schematically shows the development of the flow. The flow recirculation phenomenon can be found downstream from the gap which separates the two incoming flows. This is caused by a reversed pressure drop in the region where the parallel channel flows start to merge. After the flow was fully development, the velocity profiles are parabolic as expected. In the present work, the parameter, L_D/H, is introduced as a developing coefficient to evaluate the recirculation behavior in a quantitative manner, where L_D defines the developing length and H is the main channel height. The developing length is determined by introducing a relative density difference,

$$\xi = \frac{\Delta\rho}{\rho} = \frac{\rho_w - \rho_c}{\rho_w} \tag{5.1}$$

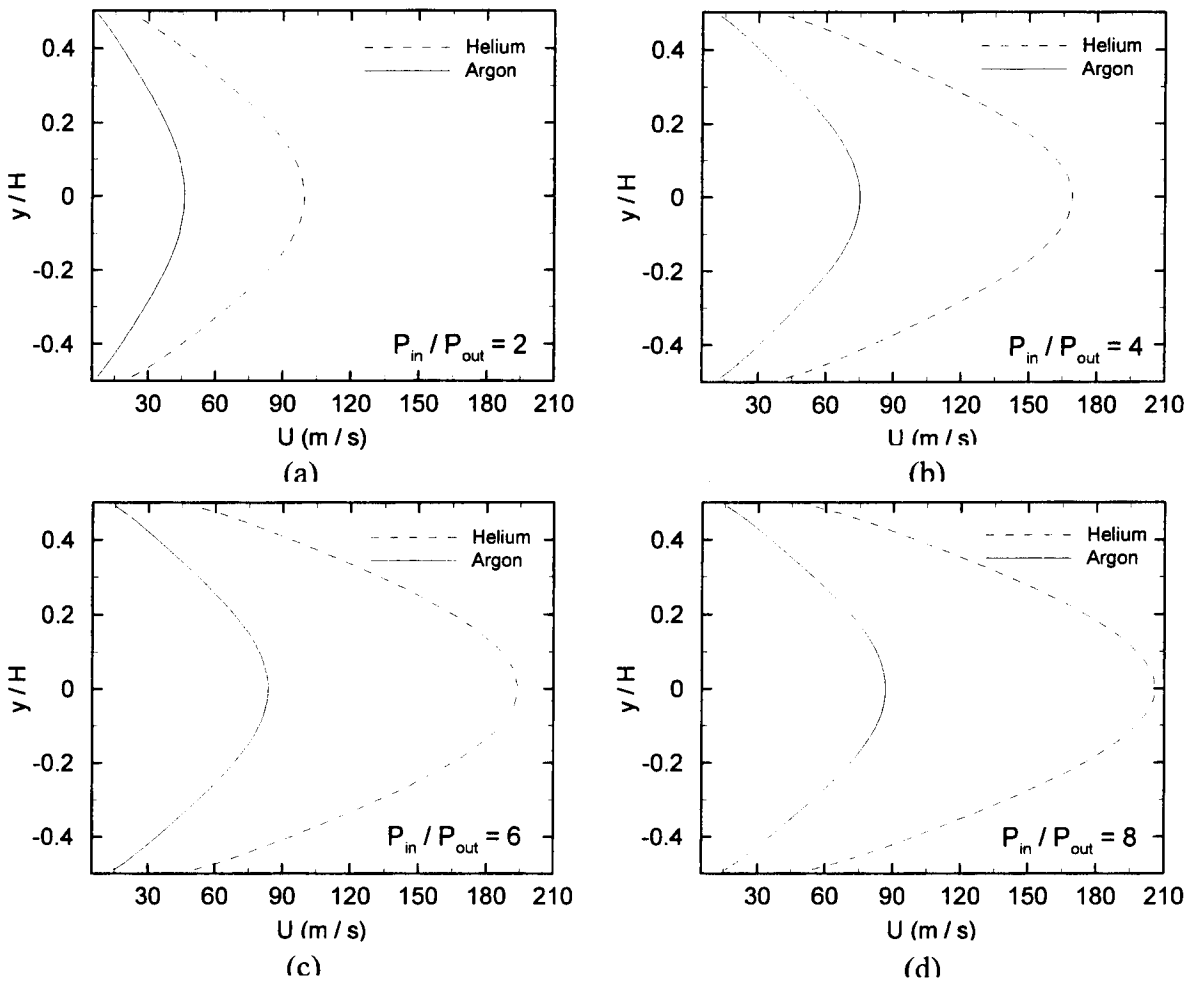

Figure 5.13: The velocity profiles at x/L = 0.431 for (a) $P_{in}/P_{out} = 2$, (b) $P_{in}/P_{out} = 4$, (c) $P_{in}/P_{out} = 6$ and (d) $P_{in}/P_{out} = 8$.

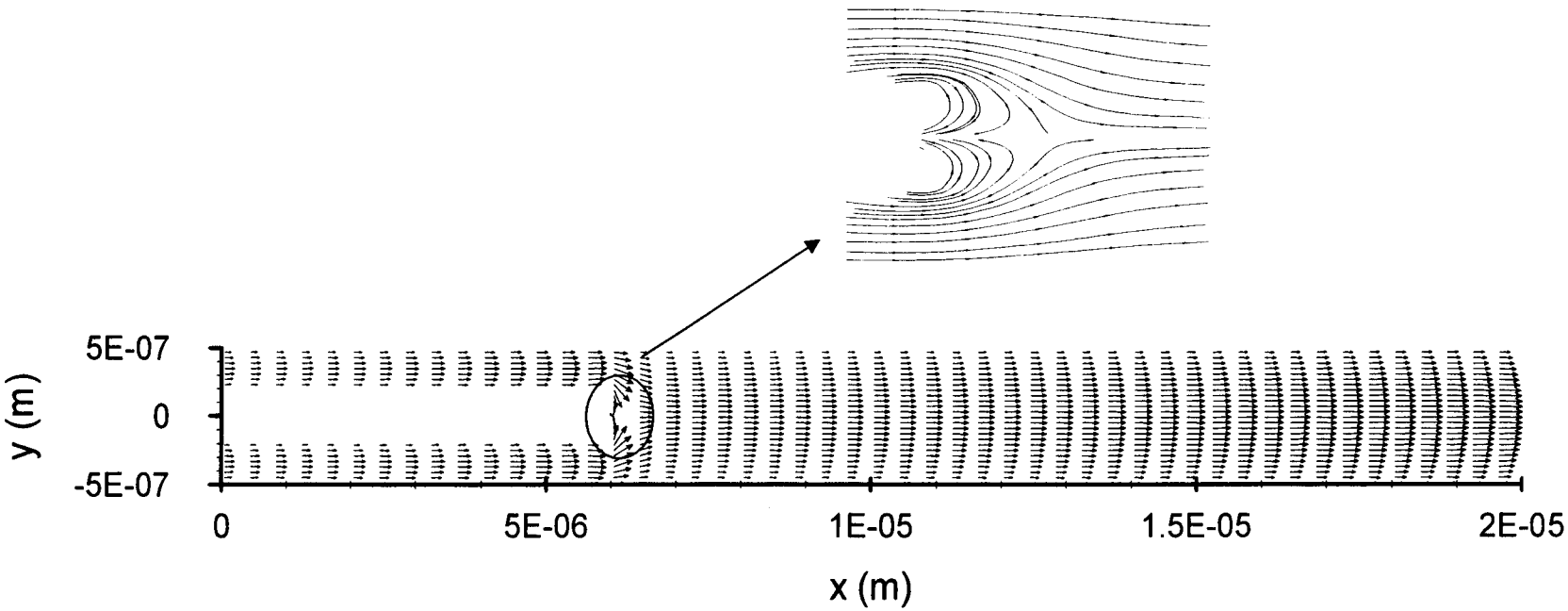

Figure 5.14: Velocity vectors of the parallel microchannel flow at Pin/Pout = 4 and Knin = 0.182.

where ρ_w refers to the flow density in the first lay of cells adjacent to the wall, and ρ_c refers the density at the channel centerline. The evolution of the relative density difference, ξ along the channel is shown in Figure 5.15. A critical value 0.3% was as a means of determining whether the recirculation is complete. As the flow goes further downstream, the fluctuation of ξ is within $\pm 0.3\%$ after a certain length. Afterwards, the flow is considered to be well developed with a relative flat density distribution along the cross section. Thus the developing length L_D can be determined as shown in Figure 5.15.

Case 7 – case 9 were carried out by varying the gap size between the two parallel channels while keeping the domain size unchanged. The value of s/H = 0 represents the situation where there is no gap to separate the parallel flows, while s/H = 1 represents the situation where the gap blocks the channel completely. As the gap height increases, the height of each of the parallel parts decreases. Figure 5.16 shows the effect of the gap size on the developing coefficient. As the gap size increases, the flow in the main channel becomes fully developed sooner. Figure 5.17 shows the effect of the gap size on the pressure distribution near the channel wall. It is apparent that as the gap size increases, more pressure drop occurs within the parallel parts due to the enhanced wall resistance, which is explained in the uniform channel section. The mass flow rate with respect to the non-dimensional gap size is shown in Figure 5.18.

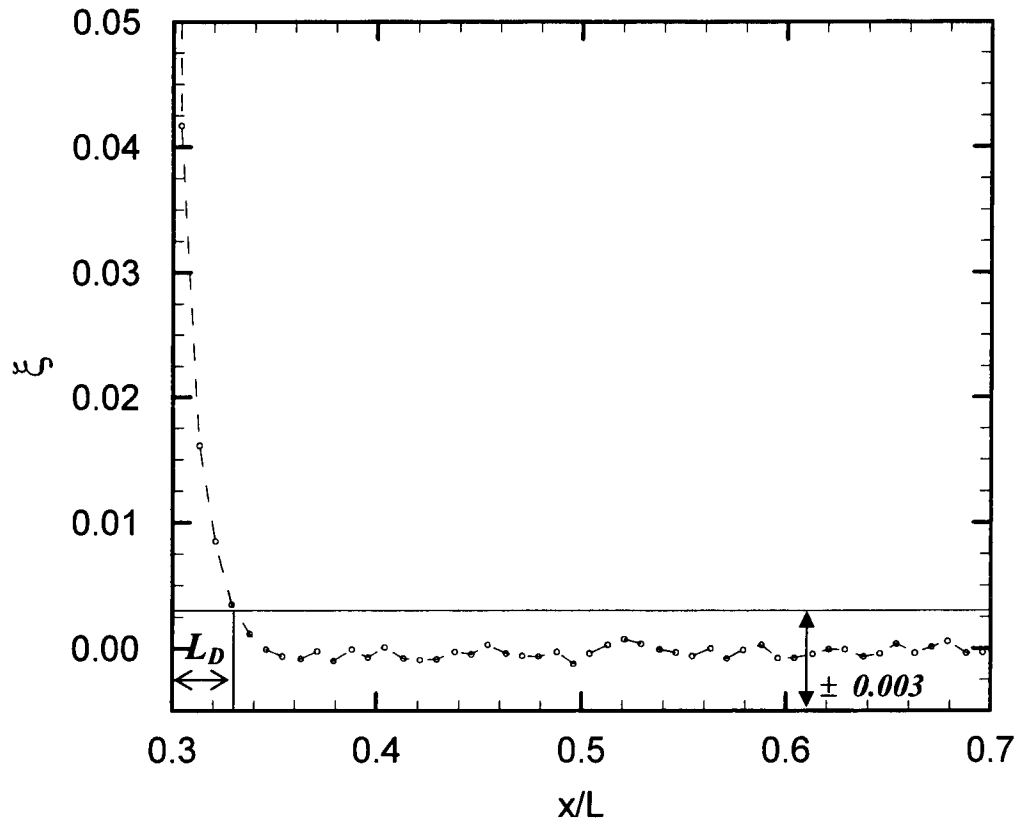

Figure 5.15: Evolution of the relative density difference.

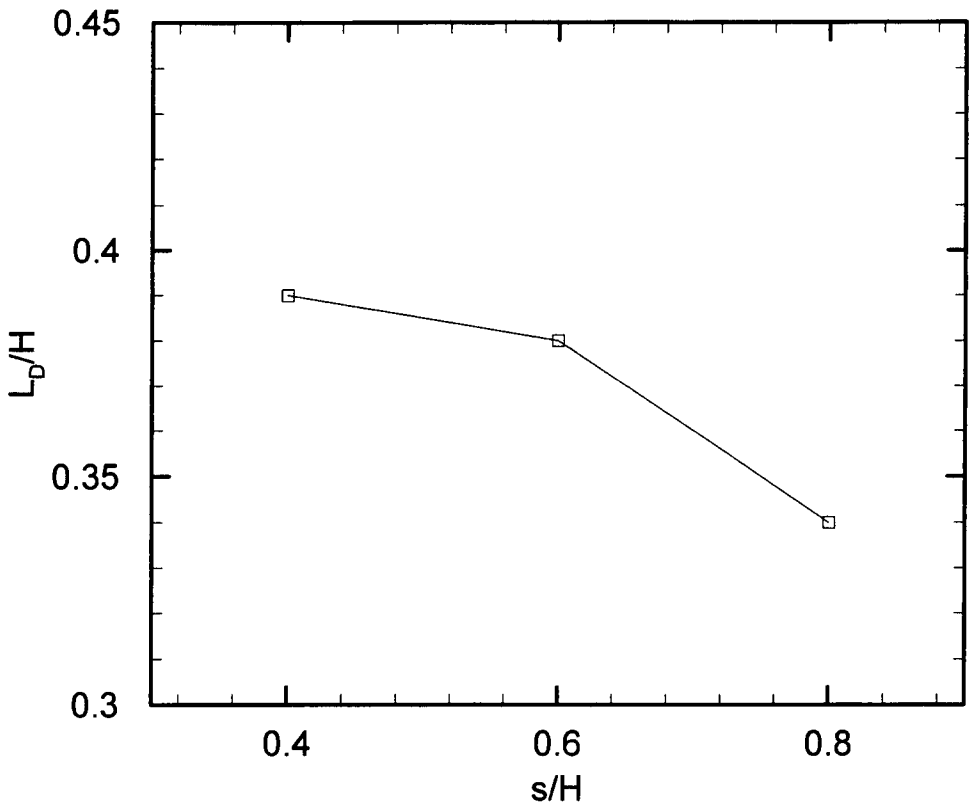

Figure 5.16: The effect of the gap size on the developing coefficient.

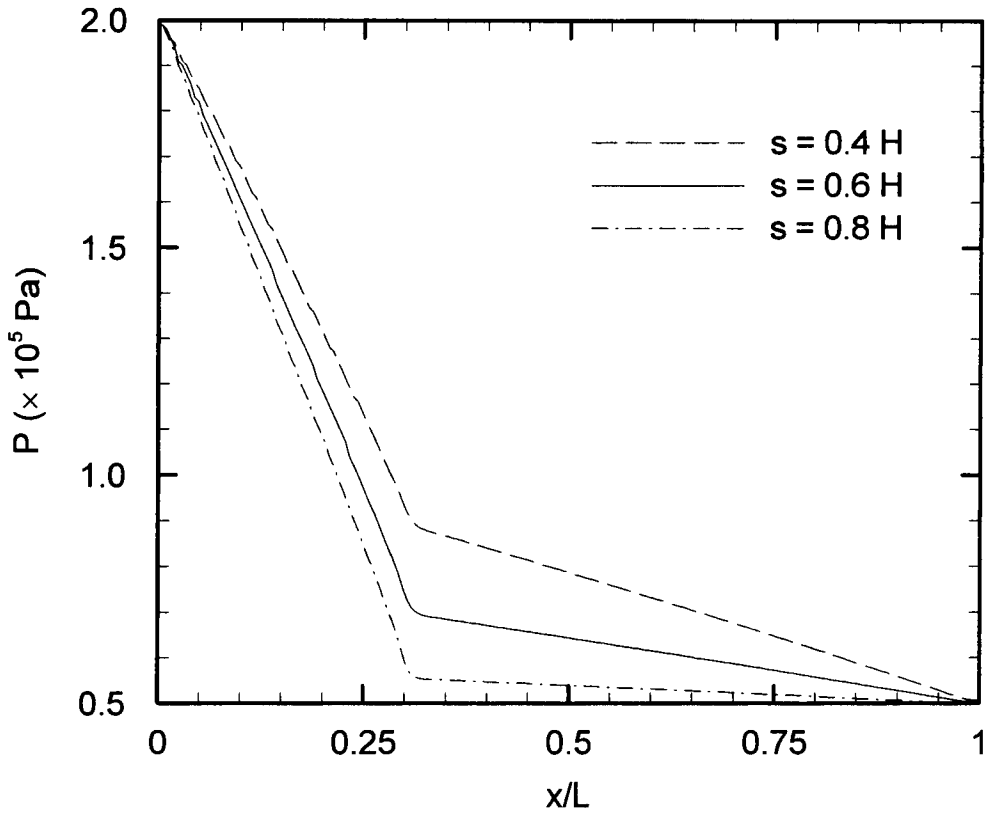

Figure 5.17: Wall pressure distribution along the parallel microchannel with different gap sizes.

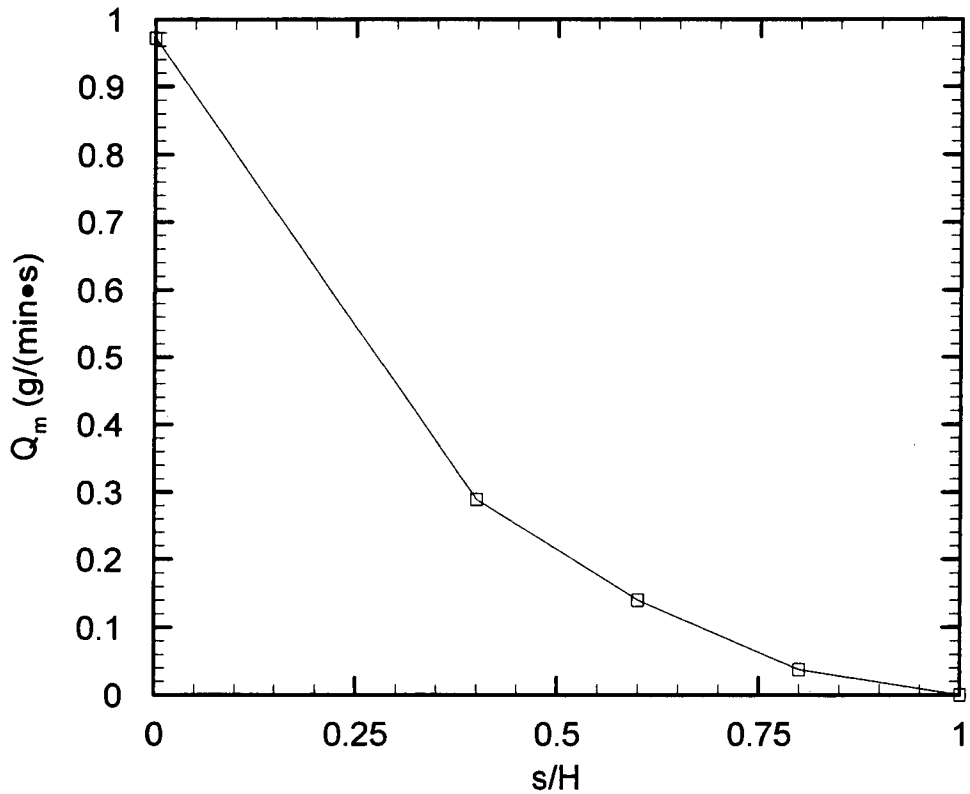

Figure 5.18: The effect of the gas size on the mass flow rate at $P_{in}/P_{out} = 4$.

5.5 T- Shape Micromixer

The mixing process of two gas species entering from two the inlets was simulated using the DSMC. CO and N_2 were selected as the working species in order to avoid the density effect on the mixing since those two gases have the same molecular mass, $m_{co} = m_{N_2} = 4.65 \times 10^{-26} kg$. The two gas streams enter the T junction from the upper and lower inlets respectively and leave the main channel exit as a gas mixture. The pressure at the two inlets is set at the same value, which is near the atmospheric pressure for most of the cases. The outlet pressure at the outlet for all cases is maintained to be low enough to prevent the backflow so as to enhance the mixing performance. All the channel walls are considered to be fully diffuse reflectors with the accommodation coefficient $\alpha = 1$. The effects of the Kn, the inlet pressure, the free stream temperature, and the wall temperature on the mixing behavior will be discussed in the following.

5.5.1 Characterization of the mixing process

Consider a T shape microchannel with the inlet channel width $l_1 = 1\mu m$, the main channel length $l_2 = 5\mu m$ and the height $h = 1.2\mu m$. The free stream temperature is equal to the wall temperature, $T_{in} = T_w = 300K$. The inlet pressure is 0.1 MPa and the outlet pressure is low enough to allow only the departure of the gas mixture from the main channel. Figure 5.19 shows the velocity vectors for the T-shape microchannel flow. The two gaseous flows coming from the inlets start to merge within the T junction. In the main channel the flow is accelerated due to the I/O pressure difference, and the velocity increases a lot along the main channel with a parabolic profile. Also, the velocity slip near the wall caused by the rarefaction effect can be observed.

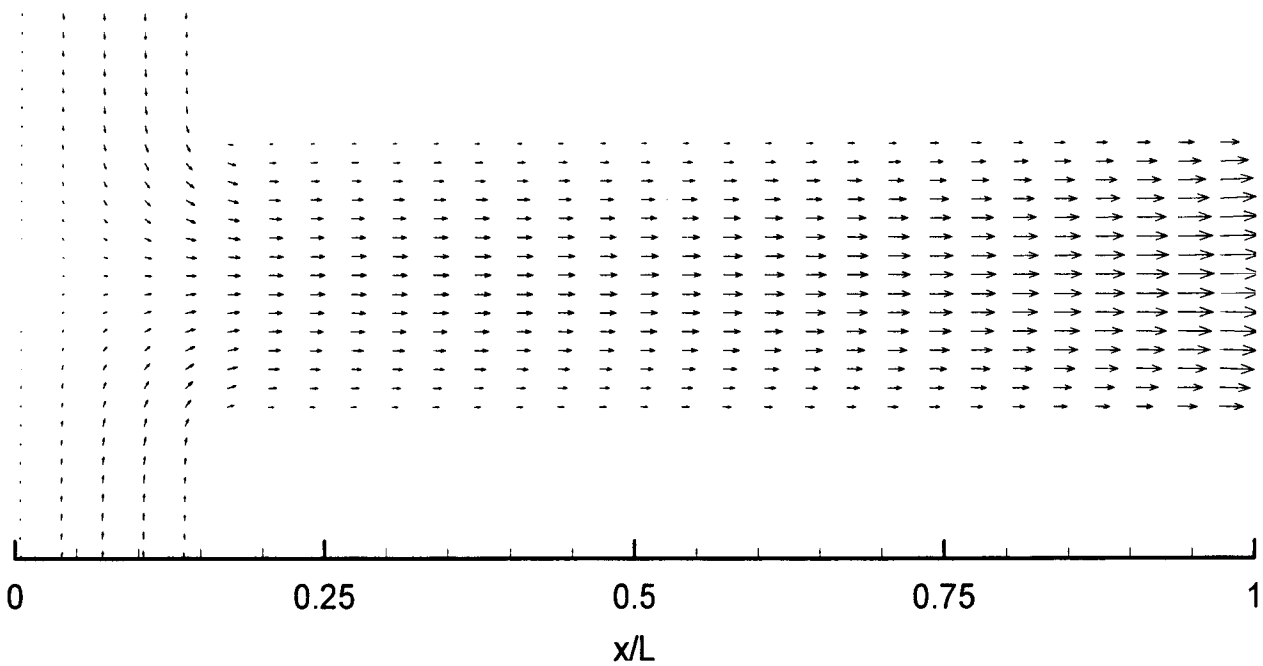

Figure 5.19: Velocity vectors for the gas mixture of CO and N_2 in T-shape microchannel.

To characterize the mixing process, a mixing length, which is used to judge the fully mixing of the two gases, needs to be defined. In Yan et al.'s work (2002), the mixing of two gases was considered to be complete as the density contours appeared symmetric about the channel centerline, and therefore the mixing length was determined. In fact, the mixing length determined by this way may cause large errors because it somehow relies on one's sense and vision. In order to evaluate the mixing process quantitatively, Wang et al. (2005) defined the relative density difference, which was calculated by

$$\xi = \frac{\rho_1 - \rho_0}{\rho_1}, \tag{5.2}$$

where ρ_1 denotes the maximum value of the density at the cross section, and ρ_0 denotes the minimum value there. If the relative density difference, which was an asymptote from 1 to 0 along the channel, decreases to 0.5 %, the two gases were considered fully mixed. In other words, the density distribution was almost uniform at the cross section. Hence, the mixing length can be determined. However, this method deals with the two gas species as a whole without giving any information about each species individually; thus, it is not adequate to evaluate the mixing process.

In the present work, the idea indicated by Gobby et al. (2001) will be used to judge the mixing process. That is, two gases are considered completely mixed when the equilibrium composition is reached. In order to quantitatively evaluate the mixing process, it is defined that complete mixing can be achieved when the composition of each species deviates by no more than ±1 % from its equilibrium composition for all locations in a cross section. In other words, gas mixing is considered complete when

$$\omega_\infty(i) - \frac{\omega_\infty(i)}{100} \le \omega(i,y) \le \omega_\infty(i) + \frac{\omega_\infty(i)}{100}, \tag{5.3}$$

where $\omega_\infty(i)$ represents the equilibrium mass fraction for species i, $i = 1,2$ and $\omega(i,y)$ represents the mass fraction for species i at location y in a cross section. Similarly, the development of the gases mixing can be also judge by defining the composition deviation coefficient as

$$\zeta = \frac{\max\left|\omega(i,y) - \omega_\infty(i)\right|}{\omega_\infty(i)}. \tag{5.4}$$

The composition deviation coefficient should decrease asymptotically to 0 along the main channel and the critical value set to judge whether the two gases are fully mixed is equal to ±1 % as mentioned before.

In our work, only the gas, CO, is taken into account to investigate the mixing process because the gas, N_2, must act the same manner as CO due to the conservation of mass. Figure 5.20 shows the mass fraction contours for CO in the T micromixer. The CO gas enters from the upper inlet while the N_2 gas enters from the lower inlet. As a result, it is reasonable to get the mass fraction of CO in the upper half of the channel higher than that in the lower half of the channel. However, it is obvious to conclude that the mass fraction contours can not quantitatively show the development of the gases combination. Instead, the evolution of the composition deviation coefficient along the main channel for CO is judged. Figure 5.21 indicates the way how the mixing length L_{mix} is defined from the simulation results. The composition deviation coefficient decreases asymptotically to 0 along the main channel as was expected before. The mixing point is picked out where the composition deviation coefficient is equal to 0.01. Then, the mixing length, L_{mix}, is defined as the distance between the starting point of the main channel and the mixing point.

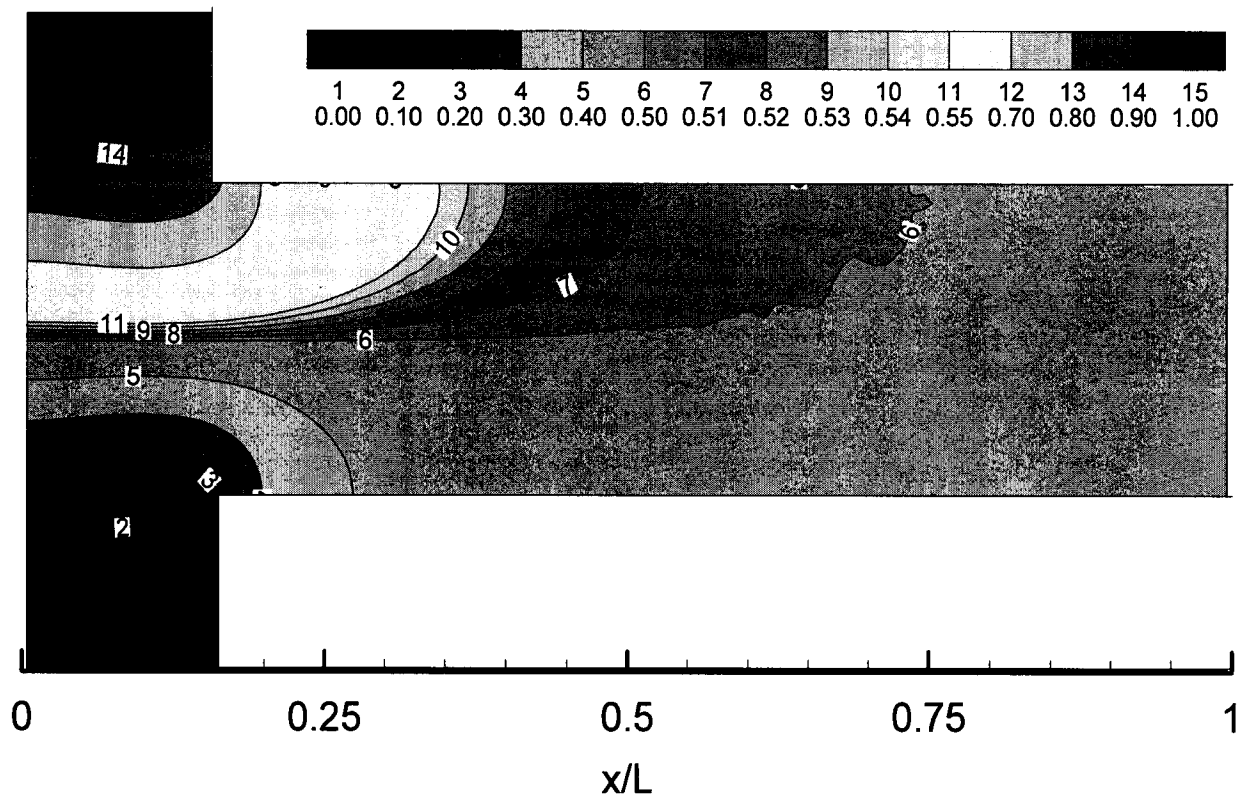

Figure 5.20: Mass fraction contours for the gas mixture of CO and N_2 in T-shape microchannel.

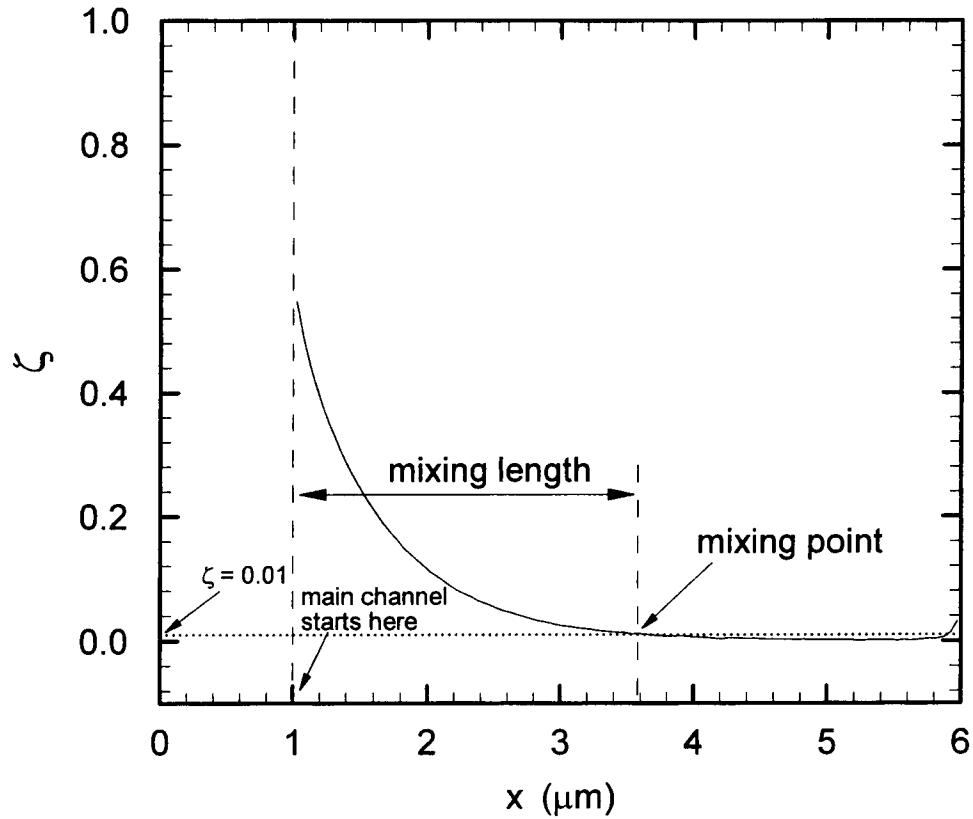

Figure 5.21: Evolution of the composition deviation coefficient along the main channel.

5.5.2 Effect of channel geometry and Kn

At a certain inlet Kn value, the effects of the channel geometry on the mixing process was investigated by changing the inlet channel width, either keeping the channel scale or maintaining the main channel height. Figure 5.22 shows the evolution of the composition deviation coefficient along the main channel for different channel size with the same scale. For the cases with the inlet channel width equal to 0.8 μm, 1.0 μm and 1.25 μm at a same inlet Kn value, the combination of CO and N_2 develops similarly along the main channel and the complete gas mixing happens at the same portion of the main channel length. Figure 5.23 refers to the cases having a certain main channel height with the inlet channel width of 0.8 μm and 1.0 μm respectively. It can be observed that the full mixing is achieved sooner for the T mixer with the lager inlet channel width.

Inspired by the fact that the channel geometry may have some effects on the mixing process even with the same inlet Kn value, the various Kn effects were investigated for the T-shape mixers at a fixed scale, and also for those with the same main channel height. It should be mentioned that only the Kn corresponding to N_2, which is very close to the value for CO due to their close molecular diameters, are counted in analyzing the results. The dimensionless mixing coefficient defined in Wang et al.'s (2005) work was also adopted here to reveal the mixing performance, which is calculated by

$$\eta_{mix} = \frac{L_{mix}}{h}, \tag{5.5}$$

where L_{mix} was defined as the mixing length before, and h is the main channel height. Figure 5.24 shows the variety of the mixing coefficient as a function of the inlet Kn corresponding to the mentioned two configurations. It can be observed that the mixing coefficient decreases as the inlet Kn increases in both conditions. Also, the Kn effect on

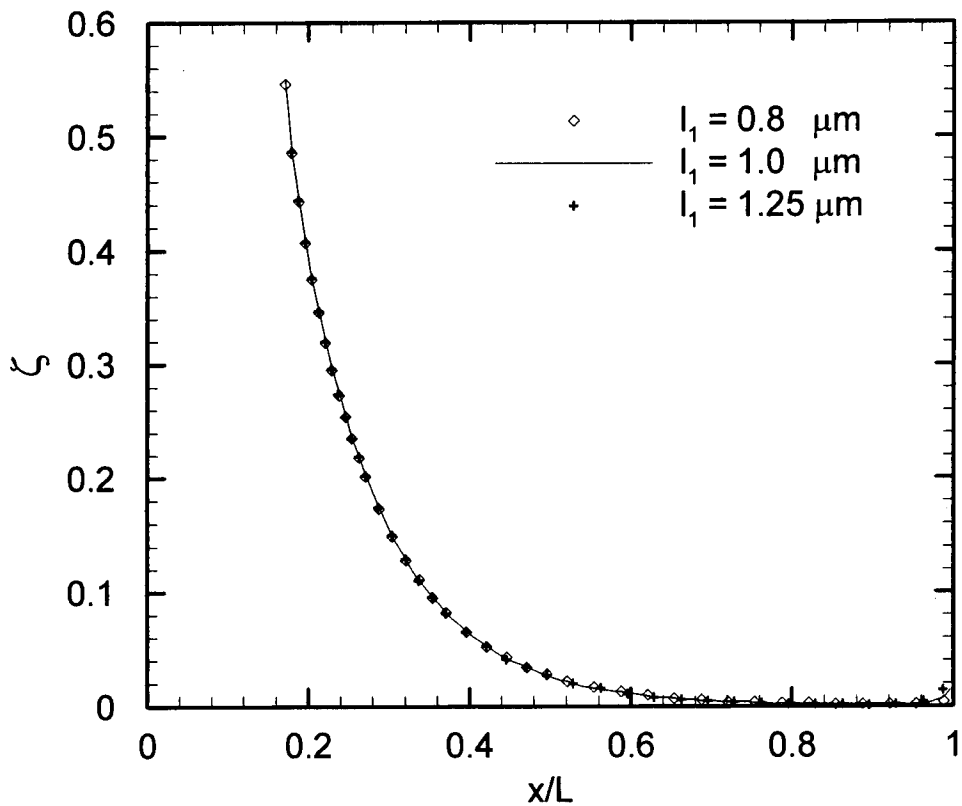

Figure 5.22: Effect of the channel dimension on the mixing process at a certain Kn.

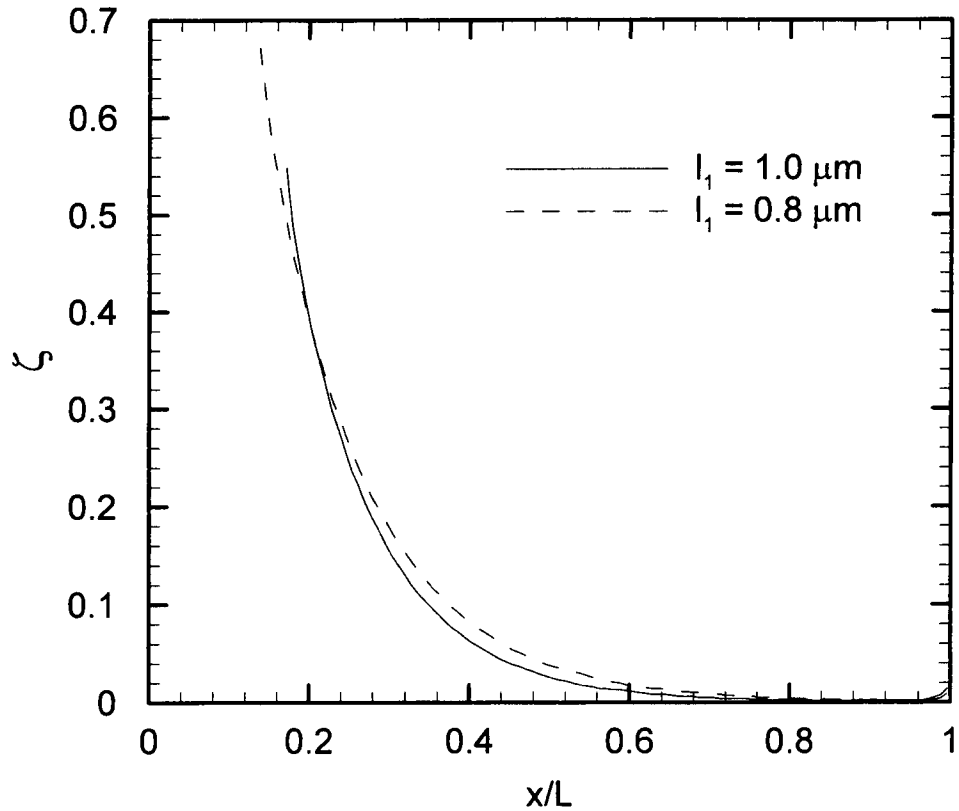

Figure 5.23: Effect of the Kn on the mixing process by changing the inlet channel width.

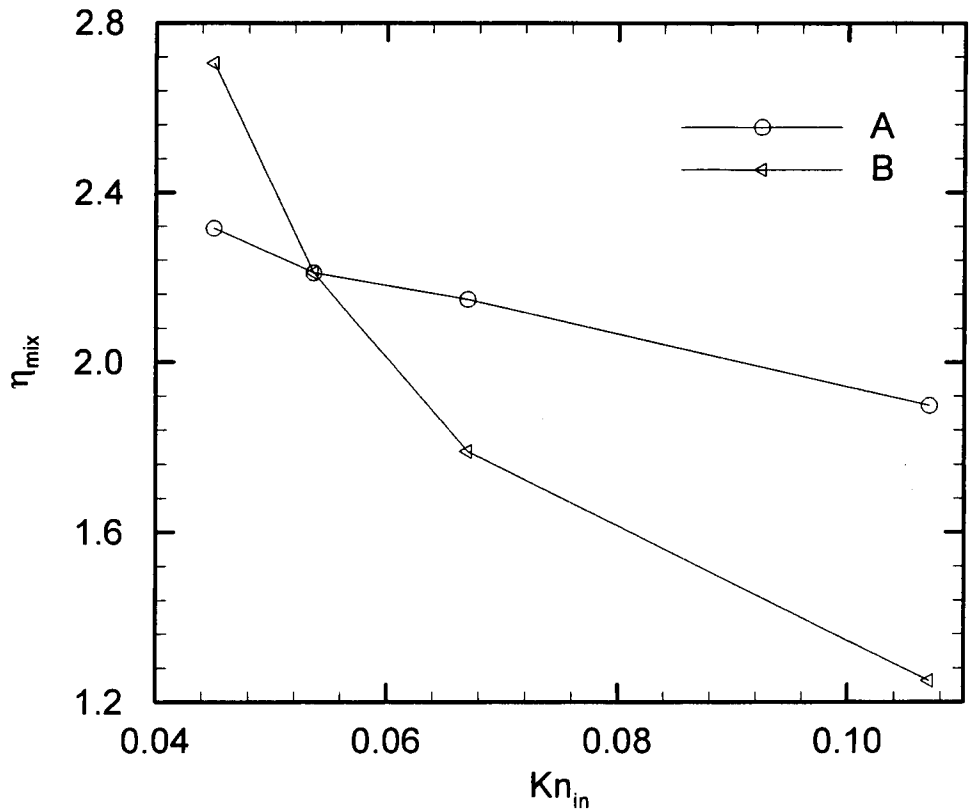

Figure 5.24: Effect of the Kn on the mixing coefficient.

the mixing coefficient is more significant while the main channel height decreases with the decreasing of the inlet channel width. This can be explained by the fact that as the geometry goes into the micro scale, which causes the flow to fall into slip or even transition flow regime, the mixing of two gases can perform more efficiently due to the diffusion effect. That is, in the T configuration the two gas streams, which are CO and N_2 in the present study, are able to diffuse more effectively at the inlet of a T junction as the Kn increases before the mixing is processed subsequently in the main channel. This kind of mixing behavior under rarefied conditions differs considerably from that under continuum conditions, which can be of most importance in the design of the later gas mixers.

5.5.3 Effects of inlet pressure, free stream temperature, and wall temperature

Calculations were repeated by changing the inlet pressure for both inlets while the outlet pressure was maintained lower enough to prevent the backflow. Four cases were carried out with the inlet pressure values of 80, 100, 120, and 150 kPa. The variation of L_{mix}/L, which is the mixing length nondimensionlized by the whole length, versus the inlet pressure is shown in Figure 5.25. It is noted that the mixing length increases monotonically with the increasing of the inlet pressure. As the inlet pressure is increased, the Kn value decreases at the channel inlet and throughout the rest of the T shape microchannel as well. Thus, the diffusion effect in the micro T junction becomes less efficient. In addition, the increment of the inlet pressure also speeds up the flow velocity, which makes the convection effect of the gas stream more pronounced compared with the diffusion effect of the molecules. Therefore, the non-dimensional mixing length is longer for the higher inlet pressure cases to achieve the complete gas mixing.

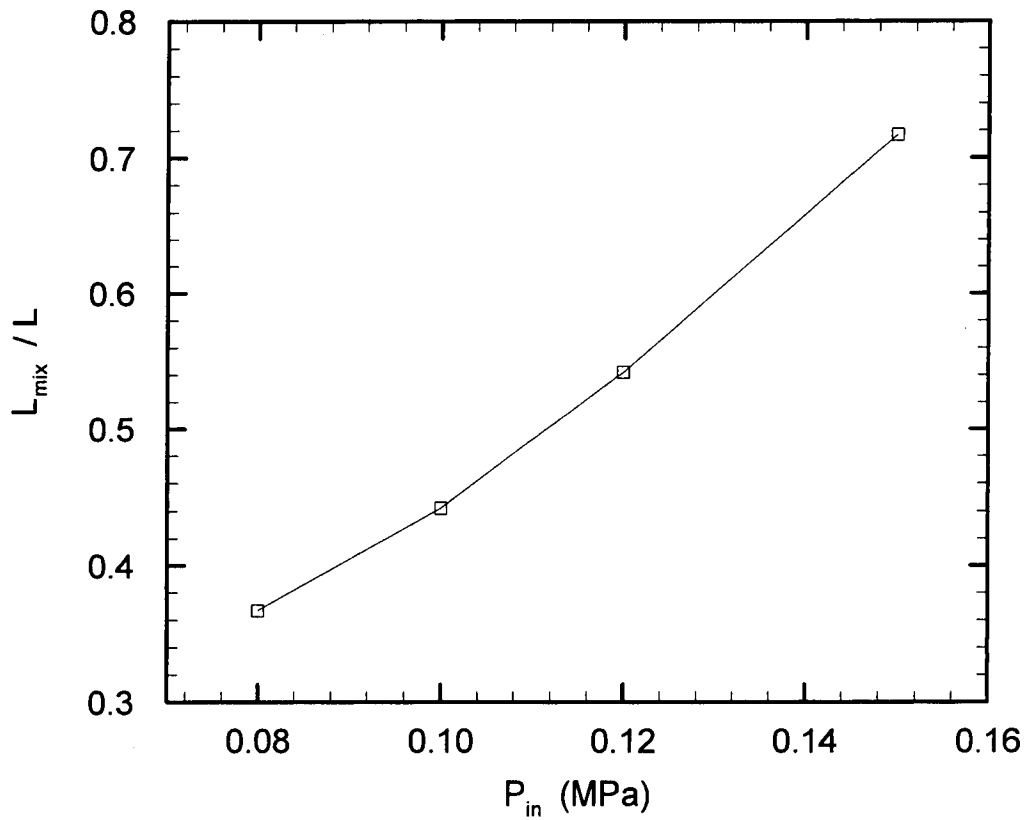

Figure 5.25: Effect of the inlet pressure on the mixing process.

The effect of the free stream temperature on the mixing process was investigated by setting the inlet gas temperature at 300, 350, 400, and 450 K respectively while the wall temperature was maintained at 300 K. It can be observed from Figure 5.26 that as the temperature of the incoming gas increases, the mixing length decreases. This is due to the fact that the higher temperature makes the thermal molecular motion become more active since as is known that the thermal velocity of a molecule is proportional to the gas temperature. As a result, the diffusion effect turns to be more significant thus enhancing the mixing process. On the other hand, when the incoming gas stream temperature was kept at 300 K while the wall temperature was set at 300, 350, 400, and 450 K respectively, similar trend can be obtained as shown in Figure 5.27; that is, the higher wall temperature leads to a shorter mixing length.

Comparing those two figures, it can be found that 150 K in free stream temperature difference just leads to less than 5 % difference in the non-dimensional mixing length. However, with the same amount in the wall temperature difference, the deviation occurring in the non-dimensional mixing length is about 13 %. It can be concluded that the mixing process is more sensitive to the wall temperature rather than the free stream temperature. It is because that when the temperature of the incoming flow is different from that of the wall, the flow temperature can adjust to be equal to the wall temperature very fast at the entrance region of the microchannel. Therefore, increasing the wall temperature can effectively increasing the gas flow temperature along the whole channel thus accelerates the mixing process.

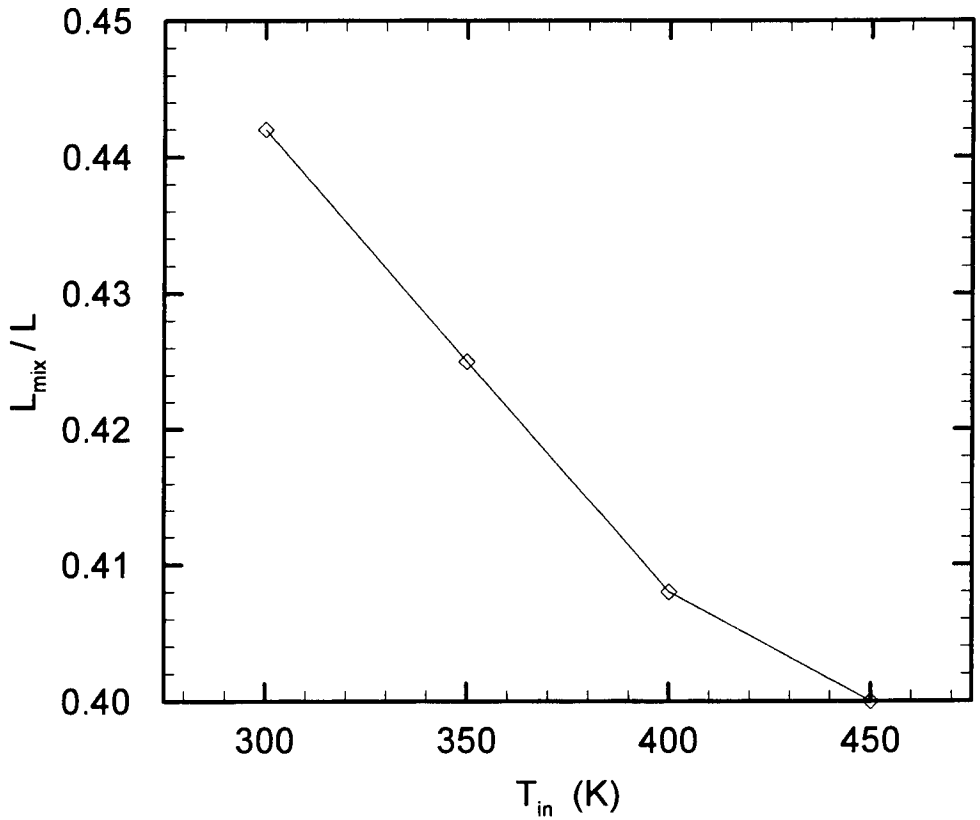

Figure 5.26: Effect of the free stream temperature on the mixing process.

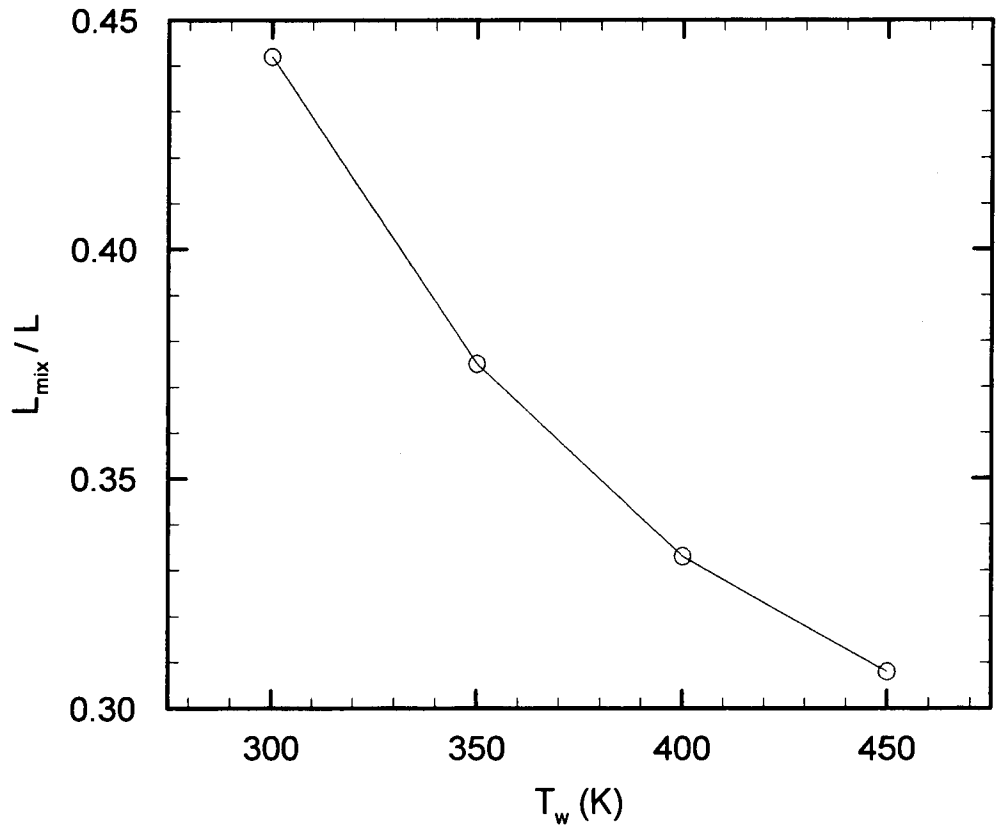

Figure 5.27: Effect of the wall temperature on the mixing process.

Table 5.1 Test cases for subsonic flow in uniform microchannel

	Straight uniform channels				
Quantity	case 1	case 2	case 3	case 4	case 5
Kn_{in} (λ/H)	0.0547			0.110	0.547
H (μm)	1			0.5	0.1
L (μm)	5	10	20	5	1
λ (μm)	5.47×10^{-2}				
mesh size	50×50	50×100	50×200	50×50	25×50
T_∞(K)	300				
P_{in}(Pa)	2.0×10^{5}				

Table 5.2 Test cases for parallel and series microchnannel flows

	Parallel channel				Series channel		
Quantity	case 6	case 7	case 8	case 9	Quantity	case 10	Case 11
Kn_{in}	0.137	0.182	0.273	0.547	species	helium	argon /helium
H(μm)	1				$h_1/2$(μm)	0.3	0.3
L(μm)	20				$h_2/2$(μm)	0.5	0.5
s(μm)	0.2	0.4	0.6	0.8	l_1(μm)	6.0	3.0
l(μm)	6				l_2(μm)	10.0	5.0
λ (um)	5.47×10^{-2}						
mesh size	50×200				-	50×160	
T_∞	300						
P_{in}(Pa)	2.0×10^{5}						

Chapter 6

Conclusion and Future Directions

6.1 Conclusion

In the present work, both supersonic and subsonic flows in uniform microchannels were simulated using the DSMC. The Kn shows a significant effect on the heat transfer characteristics and flow properties. The supersonic microchannel flow decelerates as it enters the microchannel and becomes fully developed sooner with higher Kn due to the strong viscous effect. Large kinetic energy is converted into internal energy because of the wall friction thus the heat is transferred to the bulk flow from the boundary layers. In addition, the intersection of the thermal boundary layers, where the bulk flow has been entirely heated, moves upstream as the Kn increases. For the very rarefied flow with highest Kn in the present work, there is no development of thermal layers at all. Both the wall friction and the development of the thermal boundary layers contribute to the wall heat flux. For flow in the transition regime, there is a peak in the profile moving downstream and decreasing in magnitude as the Kn decreases. Furthermore, the wall heat flux profile for the slip flow is relatively uniform along the channel in comparison to that for the transition flow case. By studying the effects of wall temperature distribution and the flow direction, it was found that change in the wall temperature and the flow direction has negligible effects on the total heat transfer.

Applying the pressure boundaries, supersonic microchannel flow without expansion waves outside the channel as well as the subsonic microchannel flow can be simulated. This boundary condition is more realistic since it is easy to be implemented practically.

For the supersonic flow, as the back pressure increases with the same inlet settings, the flow velocity at the exit region decreases indicating that more kinetic energy will be converted to internal energy. Hence, the flow temperature increases at the exit region, which also results in an enhanced wall heat flux. For supersonic flow with different inlet Mach number, significant pressure jump occurred at the lower inlet Mach number and the wall heat flux decreases considerably. However, similar trends in the wall heat flux were observed for both Mach number cases. In addition, it was also found that the temperature distribution has no obvious effect on the amount of the heat exchange between the bulk flow and the walls. For the subsonic flow, the non-linear pressure distribution and the velocity slip near the wall were obtained as expected. Different inlet Kn corresponding to the slip regime and the transition regime were employed in uniform channel cases. As a higher pressure ratio is imposed, it is possible to have the flow in mixing Kn-regimes, which makes DSMC a powerful tool for predict these types of flows. Moreover, by applying a linear wall temperature distribution, a constant heat flux can be obtained downstream from the entrance region.

Series and parallel microchannel cases were conducted by modifying the original Bird's code and a successful modeling has been achieved. Instead of using the whole rectangular domain, parts of the domains were excluded. The new computational domains for series or parallel microchannel were established by adding three surfaces and applying one symmetric boundary along the channel centerline. For series microchannel flow, larger pressure drop occurs in the narrow segment as the flow enters from either of the channel edges. By imposing different wall temperatures on the two channel segments, the diffusion effect can be observed from the temperature profiles near the interface. As a

result, a heat flux jump or heat flux drop within the interface region is obtained. Simulations were also performed for different gas species: helium and argon. Helium accelerates more than argon due to its light molecular mass. For the parallel channel cases, a parameter named as developing coefficient is defined to evaluate the recirculation flow behavior quantitatively. It was found that the gap size has a slight effect on the recirculation phenomenon.

The mixing process of two gas species, CO and N_2, within the T-shape microchannel was simulated. The outlet pressure was chosen to be lower enough to prevent the backflow in order to speed up the mixing process thus enhances the mixing performance. At a certain inlet Kn, no difference can be found in the mixing process of the two gas species as long as the scale of the geometry is fixed. When the Kn increases, the mixing coefficient decreases, indicating an enhanced mixing process. This type of mixing behavior can only be observed in micro scale, which is quite different from what can be predicted in the macro scale. Actually, those two gas streams started to mix within the T junction before entering the main channel due to the diffusion effect of the rarefied flows. In addition, the mixing length increases by increasing the inlet pressure, which speeds up the flow velocity thus making the convection effect of the gas stream more pronounced compared with the diffusion effect. Increasing the gas flow temperature or the wall temperature can both lead to an enhanced mixing process, while the effect of the wall temperature is more significant.

6.2 Future directions

The field of DSMC simulation of microflows is still in the early stage and has not been used in commercial application. In the current work, the investigated geometries are

all in 2-D, which is not applicable in analyzing the flow phenomena of the real microdevices and therefore, only some qualitative comparison between our simulation and the real flow phenomena can be achieved. Currently, some practical microdevices, such as the integrated microchannel system, which is composed of non-uniform and uniform microchannels, the integrated series and parallel microchannel system, the micro constriction devices, the micro orifice plate and the micro Venturi tube, have already been fabricated. Hence, extending the current work to a 3-D simulation model is strongly recommended in the future research work in order to predict the flow in those real devices. Also, due to the limitation of the computational capability the dimension of the involved geometries especially the length of the current used channel is not as long as that in the experimental work. In the later work, longer channels are suggested to be modeled to obtain the consistence with experimental work given that it is approved by the hardware resources.

Regarding the physical modeling, the unstructured cells are recommended to be established to discretize the computational domain so that the computational domain can not be necessarily rectangular or composed by rectangular sections, which may make the geometries to be more general. In addition, the non-ideal gas effect, the electric force, and the wall roughness may be taken into consideration and make the simulation model more close to the physical situations.

References

1. Arkilic, E.B., Schmidt, M.A., Breuer, K.S., "Gaseous Slip Flow in Long Microchannels", Journal of Microelectromechanical Systems, vol. 6, n 2, pp. 167-178, 1997.

2. Beskok A., "Simulations and Models for Gas Flows in Microgeometries", Ph.D. Dissertation, Princeton University, Princeton, 1996.

3. Bird G. A., "Molecular Gas Dynamics", Clarendon Press, Oxford, 1976.

4. Bird G. A., "Molecular Gas Dynamics and the Direct Simulation of Gas Flows", Oxford Engineering Science, Oxford University Press, New York, 1994.

5. Cheng Kan Bun, Man Wong and Yitshak Zohar, "Parallel and Series Multiple Microchannel Systems", Proceedings of the IEEE Micro Electro Mechanical Systems (MEMS), pp. 291-294, 2003.

6. Fan Qin, Xue Hong and Shu Chang, "DSMC Simulation of Gaseous Flows in Microchannels", Proceedings of the 5th ASME/JSME Joint Thermal Engineering Conference March 15-19, San Diego, California, 1999.

7. Fang Yichuan and Liou William W., "Computations of the Flow and Heat Transfer in Microdevices Using DSMC with Implicit Boundary Conditions", Journal of Heat Transfer, vol.124, pp.338-345, 2002.

8. Gabriel K., J. Jarvis, W. Trimmer, "Small Machines, Large Opportunities", NSF Tech. Rep., 1988.

9. Hadjiconstantinou Nicolas G., "Convective Heat Transfer in Micro and Nano Channels: Nusselt Number beyond Slip Flow", Proceedings of the ASME Heat Transfer Division, vol.2, pp.13-22, 2000.

10. Hadjiconstantinou Nicolas G., Simek Olga, "Constant-wall-temperature Nusselt Number in Micro and Nano-Channels", Journal of Heat transfer, vol. 124, pp.356-364, 2000.

11. Hadjiconstantinou Nicolas G., "The Effect of Viscous Heat Dissipation on Convective Heat Transfer in Small-Scale Sleeping Gaseous Flows", First International Conference on Microchannels and Minichannels, April 24-25, Rochester, New York, USA, pp. 269-273, 2003.

12. Ilgaz M. and Junichi Kobayashi, "Development of a Rarefied Gas Flow Simulator Using the Direct-Simulation Monte Carlo Method", JSME International Journal, no. 3, vol. 33, pp. 463-467, 1990.

13. Ilgaz M. and Çelenligil M. C., "DSMC Simulation of Low Density Choked Flow in Parallel-Plate Channel", 23rd International Symposium, AIP Conference Proceedings, vol. 663, pp. 831-840, 2003.

14. Karniadakis George, Ali Beskok, "Micro Flows: Fundamentals and Simulation", Springer-Verlag, New York, 2002.

15. Li Xinxin, Wing Yin Lee, Man Wong, and Yitshak Zohar, "Gas Flow in Constriction Microdevices", Sensor and Actuators, vol. 83, pp. 277-283, 2000.

16. Liou, W. W., Y.C. Fang, "Implicit Boundary Conditions for Direct Simulation Monte Carlo Method in MEMS Flow Predictions", CMES, vol.1, no.4, pp. 119-128, 2000.

17. Liou, William W., Y. Fang, "Heat Transfer in Microchannel Devices Using DSMC", Journal of Microelectromechanical system, vol.10, no.2. pp. 274-279, 2001.

18. Liu, Jianqiang, Tai Yu-Chong, Ho Chih-Ming, "MEMS for Pressure Distribution Studies of Gaseous Flows in Microchannels", Proceedings of the IEEE Micro Electro Mechanical Systems (MEMS), pp. 209-215, 1995.

19. Liu Frank HsinChih, "Artificial-Moving-Wall Condition in Simulation of Micro Couette Flow", Second International Conference on Microchannels and Minichannels (ICMM 2004-2335), June 17-19, 2004.

20. Mavriplis C., J.C. Ahn, R. Goulard, "Heat Transfer and Flowfields in Short Microchannels Using Direct Simulation Monte Carlo", Journal of Thermophysics and Heat Transfer, vol. 11, n 4, pp. 489-96, 1997.

21. Nance Robert P., David B. Hash, and H. A. Hassan, "Role of Boundary Conditions in Monte Carlo Simulation of Microelectromechanical Systems", Journal of Thermophysics and Heat Transfer, no. 3, vol. 12, pp. 447-449, 1998.

22. Oh, C. K., E. S. Oran, R. S. Sinkovits, "Computations of High-Speed, High Knudsen Number Microchannel Flows", Journal of Thermophysics and Heat Transfer, vol.11, no.4, pp. 497-505, 1997.

23. Oran E. S., C. K. Oh, and B. Z. Cybyk, "Direct Simulation Monte Carlo: Recent Advances and Application", Annual Review of Fluid Mechanics, vol. 30, pp. 403-441, 1998.

24. Pan L. S., G. R. Liu, B. C. Khoo, and B. Song, " A Modified Direct Simulation Monte Carlo Method for Low-speed Microflows", Journal of Micromechanics and Microengineering, vol. 10, pp. 21-27, 2000.

25. Park J. H., S. W. Baek, S. J. Kang, and M. J. Yu, "Analysis of Thermal Slip in Oscillating Rarefied Flow Using DSMC", Numerical Heat Transfer, Part A, vol. 42, pp. 647-659, 2002.

26. Park J. H., P. Bahukudumbi, and Ali Beskok, "Rarefaction Effects on Shear Driven Oscillatory Gas Flows: A Direct Simulation Monte Carlo Study in the Entire Knudsen Regime", Physics of Fluids, vol. 16, no. 2, pp. 317-330, 2004.

27. Piekos E. S. and K. S. Breuer, "DSMC Modeling of Micromechanical Device", FDRL-TR-95-5, Fluid Dynamics Research Laboratory, 1995.

28. Piekos E. S. and K. S. Breuer, "Numerical Modeling of Micromechanical Devices Using the Direct Simulation Monte Carlo Method", Journal of Fluids Engineering, vol. 118, pp. 464-469, 1996.

29. Pong, Kin-Choek, Ho Chih-Ming, Liu Jianqiang, Tai Yu-Chong, "Non-linear Pressure Distribution in Uniform Microchannels", Application of Microfabrication to Fluid Mechanics, ASME, pp. 51-56, 1994.

30. Qunwu, H., Qiuwang, W., Xian, W., Ozoe, H., "Computational Investigation of Low-speed Gas Flow and Heat Transfer in Micro-channel Using DSMC with Pressure Boundary Condition", Computational Studies, Advanced Computational Methods in Heat Transfer VIII, vol. 5, pp. 463-469, 2004.

31. Shih Jack C., Chih-Ming Ho, Jiangqiang Liu, and Yu-Chong Tai, "Monatomic and Polyatomic Gas Flow through Uniform Microchannels", Microelectromechanical Systems, ASME, vol. 59, pp. 197-202, 1996.

32. Shu C., Mao X. H. and Chew Y.T., "Particle Number Per Cell and Scaling Factor Effect on Accuracy of DSMC Simulation of Microflows", International Journal of Numerical Methods for Heat and Fluid Flow, vol. 15, pp. 827-841, 2005.

33. Wang Moran, Zhixin Li., "Non-ideal Gas Flow and Heat Transfer in Micro- and Nano Channels Using the Direct Simulation Monte Carlo Method", Physical Review E. 68: 046704(1-6), 2003.

34. Wang Moran, Li Zhixin, "Simulations for Gas Flows in Microgeometries Using the Direct Simulation Monte Carlo method", International Journal of Heat and Fluid Flow, vol. 25, n 6, December, pp. 975-985, 2004.

35. Wang Moran, Li Zhixin, "Gases Mixing in Microchannels using the direct simulation Monte Carlo method", ASME International Conference of Micro and Mini Channel, Toronto, CA, June 13-15, 2005.

36. Wu J.-S., Fred Lee and S.-C. Wong, "Pressure Boundary Treatment in Internal Gas Flows at Subsonic Speed Using the DSMC Method", Rarefied Gas Dynamics: 22nd International Symposium, pp. 408-417, 2000.

37. Wu J.-S., Tseng K.-C., "Analysis of Micro-scale Gas Flows with Pressure Boundaries Using Direct Simulation Monte Carlo Method", Computers and Fluids, vol. 30, pp. 711-735, 2001.

38. Xue H., Fan Q., Shu C., "Prediction of Micro-channel Flows Using Direct Simulation Monte Carlo", Probabilistic Engineering Mechanics, vol. 15, pp. 213-219, 2000.

39. Xue Hong, Ji Hongmiao and Shu Chang, 2003, "Prediction of Flow and Heat Transfer Characteristics in Micro-Coutte Flow, Microscale Thermophysical Engineering", vol.7, pp.51-68, 2003.

40. Yan Fang, Farouk Bakhtier, Johnson Jeremy, "Direct Simulation Monte Carlo Calculations of Three Dimensional Non-continuum Gas Flows", American Society of Mechanical Engineers, Heat Transfer Division, (Publication) HTD, vol. 372, n 6, pp. 33-40, 2002.